TÉCNICO LISBOA

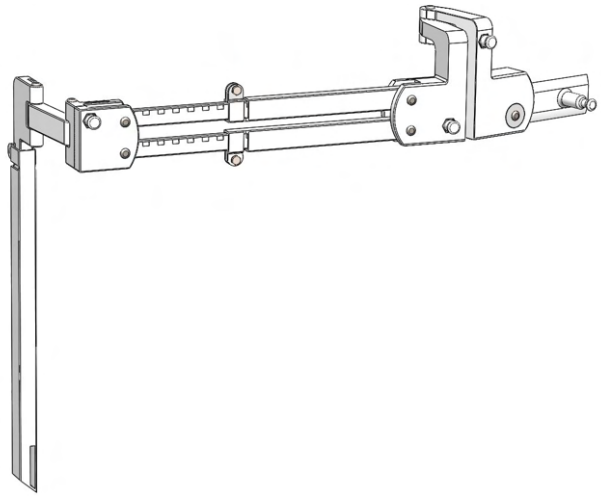

Analysis and design of an assistive and adjustable 3D-printed exoskeleton for disabled children

Joana Filipa Oliveira dos Santos

Thesis to obtain the Master of Science Degree in

Mechanical Engineering

Supervisors: Prof. Luís Filipe Galrão dos Reis
Prof. Miguel António Lopes de Matos Neves

Examination Committee

Chairperson: Prof. Paulo Rui Alves Fernandes
Supervisor: Prof. Miguel António Lopes de Matos Neves
Member of the Committee: Prof. Miguel Pedro Tavares da Silva

December 2021

I wholeheartedly dedicate this thesis to the unprivileged disabled children around the world. I hope this work contributes to improve the quality of life of anyone who suffers from musculoskeletal disorders, regardless of socioeconomic status.

Acknowledgments

Firstly, I would like to thank my supervisors, professors Miguel Neves and Luís Reis, for their constant support and encouragement throughout this thesis. Their productive criticism, suggestions, and expertise were essential for its completion.

I extend my gratitude to the Instituto Superior Técnico professors that throughout the course of my bachelor's and master's contributed to my growth as a student and future mechanical engineer, and as a person.

I am also extremely grateful to the friends I made along the way, without whom my college experience would not have been nearly as enjoyable and fun. To my best friends, Débora, Miguel, and Tatiana, thank you for being part of my best memories and being present in the worst moments. You made this journey worthwhile.

I would also like to acknowledge the support and strength that my family gave me throughout my education. I am eternally grateful to have amazing parents, Dora and Leonel, that provided me with all the opportunities they could afford, allowing me to pursue a master's degree in mechanical engineering.

Additionally, I would like to thank my boyfriend, Gabriel, who offered comfort and advice and without whom this work would not have been possible. Finally, I would like to like to acknowledge my cats for being my source of happiness, laughter, and tranquility in times of stress.

Resumo

Com a prevalência de perturbações músculo-esqueléticas a aumentar no mundo, a indústria de exosqueletos aplicada na área de assistência e reabilitação de condições médicas tem sido um setor em rápido crescimento. Distúrbios músculo-esqueléticos que afetam os membros superiores são particularmente preocupantes visto que a mobilidade dos braços é crucial para efetuar tarefas básicas do dia-a-dia e pacientes que sofrem deste tipo de deficiência têm um nível de qualidade de vida mais baixo. No que toca a crianças, a mobilidade dos braços é extremamente importante para ganhar independência e viver uma infância, e desenvolvimento, normal. No entanto, o número limitado de exosqueletos para assistência dos membros superiores para crianças atualmente disponíveis no mercado não são adaptáveis ao seu crescimento e são, frequentemente, inacessíveis a crianças desfavorecidas.

Na presente dissertação, é proposto um exosqueleto ergonómico passivo para assistência dos membros superiores impresso em 3D. O projeto do exosqueleto é baseado no Wilmington Robotic Exoskeleton, uma ortose passiva que usa elásticos para compensar a força da gravidade e proporcionar uma sensação de flutuação, que permite ao utilizador efetuar certos movimentos que não seriam possíveis sem o exosqueleto. O novo exosqueleto projetado é ajustável a um paciente dos 2 anos até à idade adulta e possibilita ao utilizador efetuar atividades quotidianas, sem interferir no seu ambiente e conforto. Por fim, um protótipo do projeto final é fabricado em ácido poliláctico numa impressora 3D, e os elementos que ligam o exosqueleto ao corpo do utilizador são impressos em poliuretano termoplástico.

Palavras-chave: Exosqueleto, Ajustável, Impressão 3D, Exosqueleto Passivo, Membros Superiores

Abstract

As the prevalence of musculoskeletal disorders increases throughout the world, the exoskeleton industry in the field of rehabilitative and assistive medical care has been rapidly growing. Upper extremity musculoskeletal disorders are one of the most concerning disabilities as mobility in the upper limbs is pivotal to perform basic tasks, and patients that suffer from these kinds of disorders often have a decreased quality of life. For children, upper limb mobility is crucial to gain independence and live a normal childhood. However, the limited number of commercially available upper limb assistive exoskeletons for children are not adaptable to their growth and are often inaccessible to underprivileged patients.

In this dissertation, a 3D printed ergonomic passive upper limb exoskeleton that mitigates the problems mentioned previously is proposed. The design of the exoskeleton is based on the Wilmington Robotic Exoskeleton, a passive orthosis that uses elastic bands to counterweight gravity and provide a flotation sensation to the user, enabling arm movement. The redesigned exoskeleton is adjustable to a patient from 2 years old to adulthood and allows the user to perform the essential activities of daily living through fluid movements, without interfering with the environment and the comfort of the wearer. A prototype of the final design of the exoskeleton is completely 3D printed in polylactic acid, and the connecting elements to the body of the user are printed using thermoplastic polyurethane.

Keywords: Exoskeleton, Adjustable, 3D Printing, Passive Exoskeleton, Upper Limbs

Contents

List of Tables

List of Figures

Nomenclature

Analytical Calculations Symbols

σ_a, σ_b	Principal stresses
σ_F	Normal stress in uniaxial tension or compression
σ_M	Maximum normal stress due a bending moment
σ_y	Normal stresses applied in the y-axis
σ_z	Normal stresses applied in the z-direction
τ_T	Shear stresses due to a torsional moment
τ_V	Transverse shear stress due to a shear force
$\tau_z y$	Total shear stresses
A	Area of the cross-section
A_M	Area enclosed by a section's median line
D	External diameter
d	Internal diameter
F	Normal force
h	Height
I	Second moment of area
K_t	Geometric stress concentration factor
M_x	Bending moment around the x-axis
M_y	Bending moment around the y-axis
n_s	Safety factor
Q	First moment of area
T	Torsional moment

t	Wall thickness
V	Shear force
w	Width

Dynamic Model Symbols

1	Vector of the degrees of freedom
α_j	Link twist of joint j
τ	Vector of applied torques at the actuated joints
θ_j	Joint angle of joint j
A_j	Homogeneous transformation matrix
a_j	Link offset of joint j
$C(q, \dot{q})$	Coriolis and centrifugal vector
d_j	Link length of joint j
$f(\dot{q})$	Damping vector
F_e	Vector of external forces applied by the human and/or external load
$G(q)$	Gravitational vector
J_e^T	Transposed extended Jacobian matrix
$M(q)$	Inertia matrix
P_{load}	Load applied in the exoskeleton

List of Abbreviations

3DP	Three-Dimensional Printing.
3D	Three-Dimensional.
ABS	Acrylonitrile Butadiene Styrene.
ADLs	Activities of Daily Living.
ADs	Assistive devices.
AMC	Arthrogryposis Multiplex Congenital.
AM	Additive Manufacturing.
CAD	Computer-Aided Design.
CAM	Computer-Aided Manufacturing.
CMD	Congenital Muscular Dystrophies.
CNC	Computerized Numerical Control.
DMD	Duchenne Muscular Dystrophy.
DMLS	Direct Metal Laser Sintering.
DOFs	Degrees of Freedom.
EM	Electrorheologica Material.
FDM	Fused Deposition Modeling.
FEA	Finite Element Aanalysis.
FEM	Finite Element Method.
FFA	Flexible Fluidic Actuators.
HAL	Hybrid Assistive Limb.
MDs	Musculoskeletal Disorders.
MD	Muscular Dystrophies.
MIT	Massachusetts Institute of Technology.
MR	Magnetorheological Material.
NASA	National Aeronautics and Space Administration.
PAMs	Pneumatic Artificial Muscles.
PBF	Powder Bed Fusion.
PLA	Polylactic Acid.
ROM	Range of Motion.
SLA	Stereolitography.

SLM Selective Laser Melting.

SLS Selective Laser Sintering.

SMA Spinal Muscular Atrophy.

STL Digital Light Processing.

TPU Thermoplastic Polyurethane.

UEDs Upper Extremity Musculoskeletal Disorders.

US United States.

WHO World Health Organization.

WREX Wilmington Robotic Exoskeleton.

Chapter 1

Introduction

The first chapter introduces the theme of the present dissertation, the relevance of the subject selected, and the overall purpose of this thesis. Additionally, an introduction to the topic of upper limb exoskeletons, in particular the Wilmington Robotic Exoskeleton (WREX), and the disorders to which it is applicable is presented in the second section. The specific objectives of the present thesis are outlined in section 1.3 and, in the section 1.4, the structure of this dissertation is delineated.

1.1 Motivation

According to the World Health Organization (WHO), it is estimated that 15% of the world's population suffers from some form of disability. This percentage has been increasing throughout the years as the world's population ages and chronic health conditions become more common. The prevalence of disability is higher in lower-income households and countries [1]. Musculoskeletal disorders (MDs) are conditions that affect the spinal cord, limbs, and joints and cause limited mobility and consequent decrease in the quality of life of the individual. These kinds of disorders are the leading cause of disability worldwide [2].

Although the data on the prevalence of these types of disorders is inconsistent, upper extremity musculoskeletal disorders (UEDs) are one of the most concerning MDs [3]. The upper extremity is the part of the upper body that encompasses the upper arm, the forearm, and the hand. Mobility in the upper limbs is crucial to perform basic day-to-day activities and the lack of functionality in this area can have a large impact on various aspects of the disabled person's life. While for people that are visually or hearing impaired, wheelchair users, and people with limited walking abilities there are various measures implemented to assure their accessibility and involvement in society, it is rare to find inclusion strategies targeted towards people suffering from UEDs. In fact, the target group for measures concerning accessibility for the disabled, that was prepared in collaboration with the United Nations Economic and Social Commission, does not include people with functional disabilities of the arm or hand [4]. For people suffering from UEDs it is also increasingly more difficult to adapt to work tasks and, consequently, achieve financial comfort and independence [5].

From these conditions came the necessity to create exoskeletons. Exoskeletons are mechanical structures that are externally attached to the joints of the user and can serve multiple purposes, such as enhancing physical ability or for medical purposes, assisting and rehabilitating the user. Accordingly, the devices used to assist patients suffering from muscular paralysis or weakness are categorized as assistive exoskeletons while others used to help patients recover from certain injuries or conditions are categorized as rehabilitative exoskeletons [6]. Assistive exoskeletons are, therefore, intended to be used for extended periods of time to aid the daily activities of the user, while providing a comfortable experience. Additionally, exoskeletons can be classified as upper extremity exoskeletons, in case they are joined to the arms, shoulders, and torso, lower extremity exoskeletons, in case they offer support to the legs and hips, or as full-body exoskeletons. Lastly, passive exoskeletons do not use external power to aid in movement but resort to other elements to store energy and assist the user, such as springs and elastic bands, while active exoskeletons rely on an external source of energy [7].

Although the advances in the technology of exoskeletons have been significant in the recent past and will continue to be in the future, with projections pointing to a compound annual growth rate of the global exoskeleton market of 41.3%, from 2018 to 2025 [8], it is expected that the development of this technology will focus on military and corporate applications, as well as in assistive exoskeletons for the elderly. Contrarily, the development of devices meant for children is still somewhat scarce.

In children, musculoskeletal disorders can occur due to systemic conditions, such as Juvenile Idiopathic Arthritis and Hypermobility syndrome, orthopedic conditions, such as Scoliosis, or trauma [9]. Furthermore, upper extremity disorders are recorded in 2 out of 1000 live births [10]. Although these disorders are rare, especially in young children, the quality of life of the patient is usually severely compromised. Specifically, upper limbs disorders that affect the development of motor skills influence the mobility of the child, which causes an inability to perform basic tasks, such as getting dressed or eating, and ultimately hinders the chance to live a normal childhood. Consequently, for these kinds of conditions, the treatment is usually aimed towards maximizing the limb's function [11] through, for example, the employment of exoskeletons.

Regarding exoskeletons designed for children, the options are still very limited, as the existing exoskeletons are often too heavy, large, or expensive. One of the largest developments in recent years is the incorporation of three-dimensional (3D) printing in the construction of exoskeletons. Since 3D printing allows for the economical and rapid manufacturing of customized products, it is particularly useful in the exoskeleton industry. Additionally, 3D printing is practical in providing a replacement for parts of the exoskeleton in case they deform or fracture, or when the child outgrows them. However, the development in exoskeletons that are adjustable to the growth of the children is still insufficient, as existing 3D printed structures are still highly customized and inflexible.

Therefore, the purpose of this thesis is to analyze and design an assistive 3D-printed exoskeleton of the upper limbs that is adjustable to the child's growth.

1.2 Topic Overview

The project designed throughout the present thesis is an assistive and passive exoskeleton for the upper limbs based on the Wilmington Robotic Exoskeleton (WREX), represented in figure 1.1.

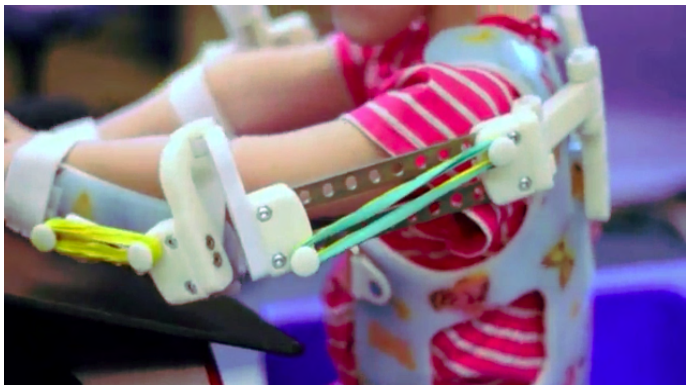

Figure 1.1: Wilmington robotic exoskeleton (WREX) exoskeleton [12]

The WREX exoskeleton was developed for children that suffer from multiple disorders, particularly muscular dystrophies (MD), spinal muscular atrophy (SMA), partial spinal cord injury, and arthrogryposis. These diseases are neuromuscular disorders that affect the strength of the muscles and, consequently, the ability of the patient to move.

Arthrogryposis multiplex congenital (AMC), also known as arthrogryposis, is a non-progressive condition that is estimated to occur once in every 3000 live births [13]. This condition is characterized by multiple joint contractures and muscle weakness throughout the body. As there is still no cure for AMC, the treatment of this condition is focused on providing the patient with the best quality of life possible and fostering independence through mobility training [14].

SMA is a rare neuromuscular disorder characterized by the degeneration of motor neurons of the spinal cord, causing muscle weakness, and affects one in every 10,000 live births [15]. As SMA is still incurable, the treatment of this disorder is focused on delaying the decline of the motor skills of the patient. In this disorder, muscular weakness in the lower limbs is more prominent than in the upper limbs. Therefore, patients who utilize an upper-limbs exoskeleton generally require that this device is attached to a wheelchair. The most common and serious form of SMA is type 1, accounting for 50% of all SMA cases, and prevents the patient from being able to perform spontaneous antigravity movements of limbs.

Muscular dystrophies are a group of incurable rare muscular disorders that cause muscle weakness and inability to properly coordinate muscle movement, generally diagnosed in childhood, with a prevalence of 25.1 per 100,000 person-years [16]. Most individuals with muscular dystrophy eventually require a wheelchair and other devices to assist movement. For MD, physical therapy is one of the most effective treatments, to maintain the strength of the muscles and delay the progress of the disorder.

Partial spinal cord injuries also affect the upper limbs function for people with tetraplegia, a paralysis that affects both arms and both legs. As lower limb rehabilitation is limited for tetraplegic patients, the main priority for treatment is to rehabilitate the upper limbs [17]. Usually, this process encompasses both surgical interventions as well as physical therapy.

The main objective of the WREX is to counter the force of gravity in order to decrease the effort the user has to make to move the arm. For this purpose, elastics, counterweights, or springs are used. Although this device, and similar exoskeletons, are not only assistive but also rehabilitative there is, currently, insufficient evidence to accurately predict the benefits of such devices in improving the condition of patients suffering from muscular weakness [18]. Therefore, it is expected that, in some cases, an upper-extremity exoskeleton will be used throughout the life of the patient.

1.3 Objectives

Considering that the exoskeleton might be used throughout the life of the patient, the objective of the present thesis is to design an exoskeleton that can be adjusted to the size of the user throughout their growth. Since the minimum age at which the WREX has been used is 2 years old [19], it is considered that the exoskeleton developed should fit the user from 2 years-old up to when the growth of the arm ceases. To fit a larger range of people, the upper limit of the anthropometric dimensions considered is for an average male adult. The anthropometric data necessary to estimate the range of dimensions of the exoskeleton is represented in table 1.1, according to [20–22], and illustrated in figure 1.2.

Table 1.1: Average anthropometric dimensions in centimeters (cm), [20–22]

Measurement	2-year-old child	Adult
1 - Shoulder-Elbow Length	17.3	36.6
2 - Mid-arm circumference	16.1	33.8
3 - Elbow-Hand Length	22.9	41.7
4 - Sagittal abdominal diameter	15.0	22.8
5 - Waist circumference	48.3	94.8
6 - Torso length	24.4	52.0

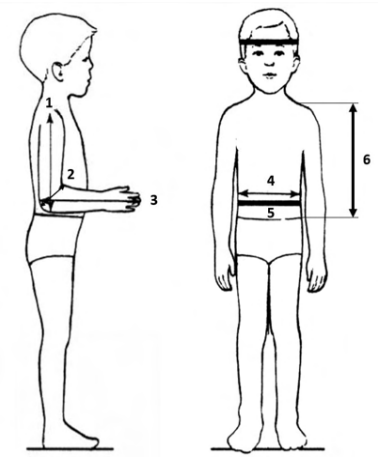

Figure 1.2: Illustration of the considered anthropometric dimensions, adapted from [20]

Contrarily to gait for the lower limbs, there are no defined standard activities of daily living (ADLs) in

regards to the upper limbs [23]. Therefore, it is necessary to define essential ADLs that the exoskeleton should allow the user to perform, according to [24], enumerated in table 1.2.

Table 1.2: Activities of daily living according to [24]

Tasks		
Hygiene-Related	Feeding-Related	Everyday
1. Reach to opposite axilla 2. Reach to opposite side of neck 3. Reach to side and back of head	4. Hand to mouth 5. Eat with a spoon 6. Drink from a mug	7. Answer the phone 8. Brush hair 9. Raise a block (5N) to shoulder height 10. Raise a block (5N) to head height

For the exoskeleton to allow for the movement required, in order to permit the user to perform basic daily tasks, it is necessary to develop an exoskeleton with five degrees of freedom (DOFs), while the WREX offers four.

There are two versions of the WREX: one that is mostly manufactured in aluminum that is attached to a wheelchair, and another that is mainly 3D printed mounted on a custom-fitted vest. In the present thesis, the exoskeleton designed must be completely manufactured through 3D printing, except for certain connecting elements such as bolts. 3D printing, as mentioned in the previous section, allows for the production of a lightweight and adjustable device and offers an inexpensive alternative to the exoskeletons currently commercialized that usually require the user to be present through the manufacturing process on multiple occasions and are highly customized being, therefore, not available to most people with MDs.

Furthermore, it is of utmost importance that the exoskeleton is comfortable and aesthetically pleasing. For ambulatory patients, it is reported the WREX device is incommodious, causing various users to reject the exoskeleton. In addition, studies that measured patients' satisfaction using the WREX reported that multiple subjects classified the device as mechanical in appearance with hard links and joints that do not always move in concert with the joints of the arm, interfering with clothes and the user's environment [19, 25, 26]. Therefore, one of the main objectives of this thesis is to improve the ergonomics of the exoskeleton. A detailed overview of the WREX exoskeleton and its limitations is provided in section 2.4.6.

1.4 Thesis Outline

The present dissertation is subdivided into seven chapters.

Chapter 2 - Background introduces a brief state of the art of the exoskeleton industry. Firstly, a historical overview of the industry is provided in three particular areas: military, industrial, and medical. Afterward, a review of the recent technological developments and available exoskeletons in each area is presented, with a special emphasis given to exoskeletons in the healthcare industry, which is the most relevant for this thesis. The final section of the chapter focuses on the WREX exoskeleton, the basis for the design of the exoskeleton in this dissertation.

Chapter 3 - First Prototype focuses not only on the process of designing and manufacturing the first prototype but also on the improvements to be made on the prototype both in terms of the design and of the 3D printing process. The topic of 3D printing is also addressed, in particular the different processes, filaments, and parameters relevant to the present thesis.

Chapter 4 - Engineering Calculation Notes contains the analytical calculations performed to ensure that the exoskeleton complies with the safety criteria, and the subsequent changes necessary to introduce before the final prototype is manufactured.

Chapter 5 - Finite Element Analysis presents the finite element analysis executed to corroborate the results obtained in Chapter 4 and to ensure the structural integrity of the final design.

Chapter 6 - Final Prototype exhibits the final design and 3D printed prototype of the exoskeleton.

Chapter 7 - Conclusion presents the final conclusions regarding the completion of the objectives of the present thesis and the final prototype. Furthermore, possible next steps in research of the current topic and for the improvement of the exoskeleton are described in the section of future work.

Chapter 2

Background

The present chapter introduces a brief state of the art of the exoskeleton industry in various areas, particularly military, industrial, and medical, and a literature review of relevant topics concerning upper limb exoskeleton devices such as the biomechanics of the upper limbs and the actuation principles of active exoskeletons. The first section of the chapter presents a historical overview of the exoskeleton industry in various fields and the most recent developments of this technology. Afterward, a review of multiple prototypes, concepts, and commercially available exoskeletons in various areas, with a special emphasis on the healthcare industry, is presented. Lastly, a detailed description of the WREX exoskeleton and its limitations is provided in section 2.4.6.

2.1 Historical Overview

The term exoskeleton originated in the field of zoology, to describe external structures that are usually observed in invertebrate species, for example in insects, crustaceans, and mollusks [27]. These hardened and rigid structures protect and support the animal.

It is difficult to pinpoint when exoskeletons designed for humans first appeared, as body armors can be considered exoskeletons and they can date back to 1400 BC [28]. Nevertheless, considering that, for the purpose of this thesis, exoskeletons are defined as mechanical structures that are externally joined to the human body, the first model of a device that resembles a bionic exoskeleton was patented in 1890. This patent described a lower-body passive exoskeleton that intended to enhance the performance of the user when running or jumping [29].

Only in the second half of the 20^{th} century the first active exoskeletons appeared. In the 1960s, the development of exoskeletons was mostly targeted towards the military, such as the Hardiman [30], a full-body exoskeleton developed to enhance soldiers' performance, or towards rehabilitative applications, such as the Kinematic Walker created by the Mihailo Pupin Institute in Belgrade [31], an active lower-body exoskeleton suitable for paralyzed patients. Both these devices can be seen in figure 2.1, and were discontinued as their heavy weight and the inadequate technology available at the time made them unviable.

(a) Hardiman developed by General Electric and the US Armed Forces [30]

(b) Kinematic walker developed by the Mihailo Pupin Institute [31]

Figure 2.1: Examples of early exoskeleton prototypes

Solely in the early 2000s, with the evolution in fields like robotics, exoskeletons became commercially available. The first rehabilitative exoskeleton available in the market was Lokomat, an active, lower-body device targeted towards hospital patients that had suffered from spinal cord injuries, as can be seen in figure 2.2 (a). In 2010, assistive exoskeletons became available for personal use, such as the ReWalk exoskeleton, presented in figure 2.2 (b), and the Indigo [32]. Most of the assistive devices available today are designed for paraplegic patients, allowing the user to move without a wheelchair.

Furthermore, exoskeletons targeted towards military applications also have been developed in the 21^{st} century, mostly by the United States Army. These devices usually focus on augmenting the strength and endurance of the user, with the objective of enhancing soldiers' abilities in combat. Full-body powered exoskeletons, such as the Raytheon XOS, the XO Max, and the Guardian XO can be put on in a short amount of time and significantly enhance human strength. In fact, the XO Max, presented in figure 2.2 (c), allows the user to lift up to 90 kg of weight for eight hours [33]. However, these exoskeletons are still not fully prepared nor developed for a close combat environment and for warm and humid climates, as they impair the agility and comfort of the user. Therefore, these devices are currently being used for applications outside of direct combat, such as to help soldiers transport armaments.

More recently, the number of exoskeletons developed for industrial applications has been exponentially growing. These exoskeletons are usually passive and have the objective of relieving the user of loads or of their own body weight. The automotive industry has been a pioneer in implementing exoskeletons in their factories, as Audi and Hyundai are both testing lower-body exoskeletons to reduce the strain in the knees of workers whose functions involve overhead labor. Furthermore, Ford has been implementing upper-body exoskeletons that support workers' arms when performing overhead tasks.

Lastly, exoskeletons can also be used by civilians to enhance certain movements, specifically for human locomotion assistance and human strength augmentation. An example of this type of exoskeleton is the Hybrid Assistive Limb (HAL), developed by the University of Tsukuba with the objective of assisting healthy people in enhancing their strength, allowing the user to lift objects weighing up to 70 kg [34].

(a) Lokomat, developed by Hocoma [35]

(b) ReWalk exoskeleton [36]

(c) XO Max developed by Sarcos [37]

Figure 2.2: Examples of commercially available exoskeletons

Furthermore, there are also devices targeted towards specific professions. To assist nurses in transferring patients, an exoskeleton was developed by the Kanagawa Institute of Technology in Atsugi [38]. Similarly, the Naval Aeronautical Engineering Institute Exoskeleton Suit was developed for the military to assist the user in carrying heavy loads and to increase speed in hazardous terrains, but can also be used by firefighters and in disaster relief situations [32]. Additionally, the National Aeronautics and Space Administration (NASA) also co-developed the X1 exoskeleton, with the purpose of training astronauts in space to prevent muscle fatigue and bone thinning [39].

Currently, although the exoskeleton industry has been significantly growing, there are still many challenges in the commercial implementation of these structures. It is necessary to decrease the weight of exoskeletons and enhance their design to provide a satisfactory experience for the user and, for active exoskeletons, it is crucial to develop lightweight and efficient power systems. However, as the research concerning this topic continues to grow, as represented in figure 2.3, solutions and technologies that tackle the problems exoskeletons often face are being implemented, resulting in more effective and ergonomic devices. Furthermore, it can be verified that the research concerning soft exoskeletons has been exponentially growing in recent years.

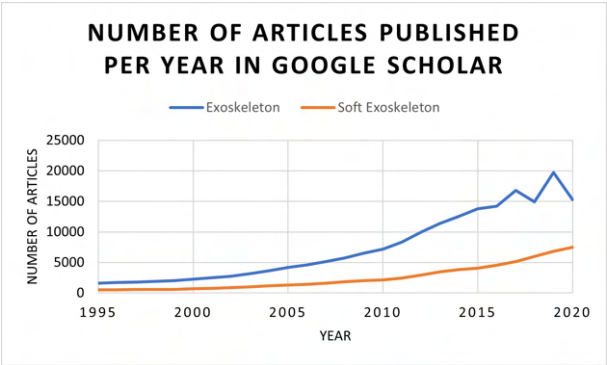

Figure 2.3: Evolution of the number of articles containing the key-words ”exoskeletons” and ”soft exoskeletons” published per year in Google Scholar

Soft-bodied exoskeletons, also commonly referred to as soft exosuits or soft wearable robots, consist of exoskeletons that do not have a rigid structure, but use textiles that better simulate the biomechanics of the human body. In parallel, the field of soft robotics has become increasingly popular in recent years mainly due to the increase of human-robot interaction especially in the field of medicine. It is, therefore, expected that in the future the industry of will shift towards soft-bodied exoskeletons as a means to develop more ergonomic and efficient devices that are widely available. For example, the ”XOS” exoskeletons mentioned previously were discontinued by the US military as their development became stagnated when the designers got caught up in the vicious cycle of developing rigid structures that require powerful and heavy actuators powered by bulky power sources that, in turn, demand heavier structures. To solve this problem, which is similar to the obstacles that the development of many current other exoskeleton projects face, soft robotics might be the solution.

In comparison with traditional rigid exoskeletons, soft-bodied exoskeletons provide fewer constraints and interference with the user and their surroundings, a reduction in the weight of the structure, and an overall better interaction with the wearer. In addition, as soft exoskeletons have less inertia and are less extensive, the energy necessary to power the exoskeleton is also reduced and the running time of the device increased. Furthermore, as wearing a soft structure is easier than fitting a rigid one, the high customization necessary for the commercially available exoskeletons in recent years could be substituted with adaptable and size-flexible structures, or even discretized into standard clothing sizes. Ergonomically, these exoskeletons also have many advantages, such as potentially being concealed underneath regular clothing, and increasing user comfort, as well as reducing the possibility of injury [40]. Cost-wise, soft exoskeletons are potentially cheaper, as fabrics and elastomers often used are cheaper than metals used in rigid-bodied exoskeletons, and as there is no need for individual customization.

However, there are some disadvantages that come with soft-bodied exoskeletons. Whereas rigid exoskeletons have a hard structure, soft systems rely on the user’s skeletal system which hinders the transfer of power, limiting the force that can be applied. For this reason, it is also increasingly difficult to mount sensors, motors, and actuators in the soft structure. Consequently, mostly pneumatic actuation is used, due to its lightweight characteristics.

To overcome the limitations of both rigid-bodied and soft-bodied exoskeletons, systems that combine both approaches are being implemented [41]. These structures consist of the combination of rigid elements placed parallel to the bones and soft elements in the joints of the user. Moreover, magnetorheological (MR) and electrorheological (ER) materials are being researched and integrated into exoskeletons. Magnetorheological materials are a group of materials that consist of micron-sized ferrous particles dispersed in a fluid or an elastomer whose properties vary when a magnetic field is applied, while electrorheological materials have a similar behavior when an electric field is imposed upon them. Similarly, shape-memory materials are also being researched for the same purposes. One example of the fusion of soft and rigid structures is tendon-driven exoskeletons. Tendon-driven mechanisms are driven by tendons that can keep a positive tension [42]. However, in comparison with Flexible Fluidic Actuators (FFA), in tendon-based exoskeletons, it is necessary to incorporate rigid structures not only to distribute the force that is localized at the point of attachment, but also to provide comfort to the user,

preventing the deformation of the otherwise soft structure.

In the future, it is also expected that the integration of nanotechnology in this industry will allow for a tremendous evolution of exoskeletons. This technology would allow for exoskeletons to become an integral part of the user and treat diseases such as obesity [29]. Another recent development in the exoskeleton industry is the introduction of 3D printing, which allows for rapid prototyping and lightweight devices. Therefore, this technology can decrease the cost of exoskeletons and expand their applicability.

The following sections focus on analyzing the current state of the exoskeleton industry in the three main application areas: military, industrial, and medical.

2.2 Military Exoskeletons

Military exoskeletons account for a share of more than one-quarter of the global exoskeleton market [8]. The exoskeletons employed for military purposes usually have the objective of augmenting human strength, endurance, and performance. Therefore, these devices are mostly active and require high torques and actuators to power the system. Actuators significantly increase the weight and the inertia of the system, creating oftentimes exoskeletons that are too inconvenient and cumbersome to use. Furthermore, military exoskeletons often require actuation in complex and multi-dimensional joints such as in the ankles. More information regarding different types of actuators and future prospects is provided in section 2.4. Furthermore, as the actuators require some form of power, difficulties ensue regarding the safety of power sources, particularly in harsh environments, since most are flammable or explosive. Another challenge that arises with military exoskeletons is related to sensing, as available sensors are not precise or quick enough, creating a lag between the intention of the user and the actual exoskeleton movement. Additionally, exoskeletons should be worn by a large number of soldiers, however, any misalignment between actuators and joints or misfit of the suit could have disastrous consequences in warfare. Consequently, it is imperial that the exoskeleton is custom-fitted to its user, which would take a large number of resources.

For the US military, the predecessor for the usage of exoskeletons for military purposes, all attempts of manufacturing exoskeletons were not successful in combat environments, due to the reasons enumerated in the previous paragraph, and subsequently discontinued. However, the Russian military has successfully integrated exoskeletons in the army. The Ratnik 3, in particular, is analyzed in the following section.

Ratnik 3

The Ratnik suit, presented in figure 2.4, is a combat gear for the Russian Army that consists of ten subsystems that include a body armor able to withstand 7.62 mm rounds and a helmet that features thermal night vision. The third-generation Ratnik also includes an active exoskeleton to increase the physical power of the user, and a passive exoskeleton, to reduce the strain on the joints and the risk of injury. The active exoskeleton is powered by a system of electric motors, levers, hydraulics, and pneumatics, substantially increasing its weight. Three hundred thousand of these devices are already in

use by Russian soldiers, most of them equipped with only the passive exoskeleton.

Figure 2.4: Third-generation Ratnik Suit [43]

The earlier version of Ratnik 3, named EO-1, featured only the passive exoskeleton and was tested in the Syria conflict in 2017 to assist soldiers carrying a console on their chest weighing over 18 kg, to control the Uran-6 mine-clearing Robot. The EO-1 test was extremely successful, with the soldiers stating that the exoskeleton was intuitive to use, rapid to put on, and could instantly be taken off if necessary. Each EO-1 exoskeleton costs around 3000 € and allows the user to carry up to 45 kg for long periods of time.

2.3 Industrial Exoskeletons

Although industrial exoskeletons have the smallest share in the global exoskeleton market, accounting for less than 25%, it is anticipated to register the fastest growth rate due to the fact that industries are becoming increasingly aware of the rising prevalence of work-related injuries and subsequent monetary losses [8]. In fact, according to the Health and Safety Executive (HSE), in the UK, musculoskeletal disorders affect 2 in every 100 workers in the construction industry. Therefore, it is crucial for companies to minimize the risk of injury to their employees and increase their productivity through the implementation of exoskeletons.

For the purpose of this thesis, analyzing industrial exoskeletons is extremely relevant as many of their characteristics align with the objectives of the exoskeleton design. Firstly, for the companies that purchase exoskeletons for their workers, minimizing the number of exoskeletons necessary is important to decrease their cost. Additionally, it would be unreasonable for every employee to attend fitting sessions and to have a customized exoskeleton. Consequently, the exoskeletons should be adaptable enough to fit most people and to be interchangeable between workers. Moreover, it is crucial to reduce the time the employees spend in mounting and fitting the device and, therefore, the exoskeleton should be easy and fast to put on. On the other hand, industrial exoskeletons must be comfortable and minimally interfere with the workflow of the user.

In the next section, two commercially available industrial exoskeletons are described, the SuitX and the Skelex 360-XFR.

SuitX

SuitX offers three exoskeletons ShoulderX, BackX and LegX, presented in figure 2.5, that reduce the users' risk of suffering injuries and physical labor when performing repetitive tasks. These exoskeletons can be used independently or in combination with each other. All these devices are passive and can fit 90% of adult humans while taking less than a minute to put on and take off. Various multinational companies such as Fiat and Siemens have implemented these exoskeletons into their workforce.

(a) ShoulderX Exoskeleton

(b) BackX Exoskeleton

(c) LegX Exoskeleton

Figure 2.5: SuitX Exoskeletons [44]

The ShoulderX is suitable for users that perform chest to overhead tasks, reducing their muscle fatigue and, consequently, improving productiveness. This passive exoskeleton weighs 3.17 kg and transfers the load from the worker's arm to their hips, minimizing their effort. In fact, a 2019 article concerning the usage of the ShoulderX concluded that muscle activity was reduced by up to 81% in workers that used the exoskeleton, in comparison with unassisted users [45].

The BackX is a lightweight exoskeleton, weighing only 3.2 kg, whose main objective is to reduce the risk of back work injuries while increasing the endurance of the worker. It is used to passively assist in tasks that involve lifting heavy objects by stooping or bending. It has been shown that the exoskeleton reduces the strain on the user's lower back by 60%, on average, and improves the time that a worker can hold a back-straining posture by 52% [46].

Lastly, the LegX supports the user's knees in squatting positions, reducing the strain in the quadriceps by 57%. This device can support a maximum of 113 kg and be adjusted to different positions and support options [47].

Skelex 360-XFR

The Skelex 360-XFR is a passive exoskeleton that acts as an anti-gravity device that supports the arms. Its main purpose is to relieve the fatigue of workers when performing overhead repetitive tasks that do not involve carrying heavy weights. Therefore, contrary to the previous exoskeletons, only loads up to 5 kg can be lifted using this device. The total weight of the device is 2.5 kg and it offers support forces from 1 to 4.9 kg per arm. Notably, companies such as Airbus, Nissan, and Honda have adopted the Skelex exoskeletons for their workforce. As presented in figure 2.6 (a), the exoskeleton is divided into a harness and the arm structures that are attachable to it.

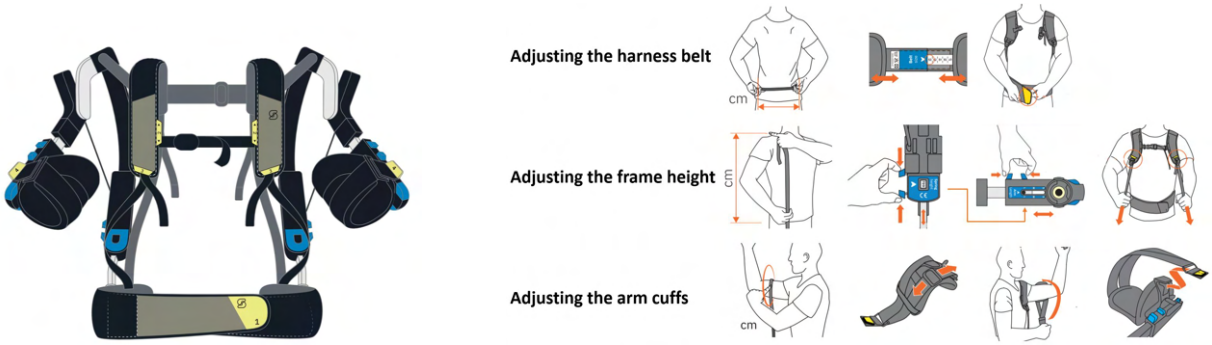

(a) Schematic of the Skelex industrial exoskeleton

(b) Skelex 360-XFR sizing and donning instructions

Figure 2.6: Skelex 360-XFR industrial exoskeleton [48]

The main advantage of the Skelex exoskeleton is the fact that it can be worn by multiple users, as it is adjustable to different sizes, and can be mounted by the wearer himself in less than 30 seconds. The process of fitting and putting on the exoskeleton is described in the following paragraph and schematized in figure 2.6 (b).

In the harness, the belt size is adaptable to the waist circumference of the user and the height of the frames is adjustable to the vertical distance from the hip bone to the top of the shoulder from 44 to 55 cm. When the height of the frames is adjusted a letter appears (S, M, or L) that facilitates setting the arm length in future situations. Additionally, the arm cups are adjustable to the user's arm circumference but are subdivided into sizes that the client can order. The small size is suitable for arm circumferences of 20 to 28 cm, the medium size covers the range from 27 to 35 cm, and the large size is adaptable to circumferences from 34 to 42 cm.

2.4 Medical Exoskeletons

The market of exoskeletons targeted towards treating medical conditions has been significantly growing, with forecasts predicting a growth rate of 35.15% between 2020 and 2027, and the market accounting for 1600 million euros by 2027 [8]. This growth is not only a consequence of the constant developments in technology but also of both the increase in chronic conditions and the aging of the world's population. Healthcare is also the industry with the largest share in the global exoskeleton market, accounting for more than half of the market size [8].

According to the United Nations, it is expected that the number of people above 60 will account for approximately 2.1 billion in 2050, nearly doubling in comparison with the same figure in 2015 [49]. As a consequence of the aging of the population and the rise of the prevalence of chronic illnesses, MDs are affecting an increasing number of people. These types of disorders impair the patient's mobility and, consequently, their independence and qualify of life. Furthermore, these patients are forced to rely on the assistance provided by caregivers, especially when suffering from upper limbs disorders that prevent the patient to perform simple actions necessary for survival such as eating.

Exoskeletons play an important role in assisting and rehabilitating patients affected by MDs that cause

loss of limb mobility, especially chronic disabilities caused by neuromuscular diseases such as stroke, spinal cord injuries, and muscular dystrophy, or neurodegenerative diseases such as multiple sclerosis. These disorders lead to muscle weakness and, often, paralysis causing patients to be unable to perform essential daily tasks. Rehabilitative exoskeletons have the function of performing physiotherapy. Namely, active exoskeletons are becoming widely used in a recently introduced form of physiotherapy named robotic therapy. Robotic therapy can not only fasten the recovery process for patients but also decrease the medical staff necessary to perform these treatments, reducing the overall cost of rehabilitation [18].

To assist the lower limb mobility of the people that suffer from these disorders, devices such as wheelchairs or walkers are often used. These Assistive Devices (ADs) are meant to assist the user in their daily living, maintaining or improving their mobility. However, current ADs have multiple limitations, such as not allowing enough limb movement and having a negative effect on the user both physically and physiologically, and are not effective in rehabilitating the user. Additionally, there are far fewer commercially available products to assist with upper limb mobility than with lower limb mobility even though non-ambulatory patients that suffer from neuromuscular disorders prioritize upper limb function over lower limb. These patients identified tasks such as re-positioning at night and while seated, bringing their hands to the mouth, using the wheelchair joystick and the computer, and tasks related to personal hygiene as their priorities [50].

Additionally, studies show that patients are receptive to exoskeletons both as assistive and rehabilitative devices. One study conducted with 118 participants that suffer from musculoskeletal disorders concluded that 96.8% of the inquired patients would prefer to use an exoskeleton over other ADs, while 84.1% favor the availability of these kinds of devices in care homes [51]. Furthermore, another study that interviewed patients suffering from muscular dystrophy, showed that 66.7% of participants would also favor exoskeletons in comparison to other devices [52].

Exoskeletons can improve the quality of life and the overall psychological and physical state of the patient. This section will focus on the state of the art and future prospects concerning exoskeletons used for medical purposes, both active and passive, and targeted towards the lower limbs and the upper limbs.

2.4.1 Lower Limb Exoskeletons

Lower limb exoskeletons are the most used in the healthcare exoskeleton industry, as it is estimated that in the US alone, 11.7 million people report difficulty walking [53]. Various conditions can cause lower-limb paralysis, such as spinal cord injuries, with a prevalence of 54 cases per one million people in the US [54] and multiple sclerosis, that affects 193 in every 100 000 people in Europe [55]. Spinal cord injuries can be rehabilitated but multiple sclerosis tends to deteriorate the patient's health and ability to walk over time. Therefore, both assistive and rehabilitative exoskeletons are important to improve the quality of life of people with difficulty walking. Assistive exoskeletons allow the user to complete movements that aid their day-to-day tasks and can be worn regularly. For example, assistive lower limb exoskeletons can allow individuals that could only walk with the help of crutches to walk independently. On the other hand, rehabilitative exoskeletons are used in physiotherapy to train an individual's muscles or nervous system to move unassisted. Exoskeletons can be both assistive and rehabilitative, as often using a device to

increase current capabilities can in turn augment the user's own abilities.

The lower limb contains three joints, the hips (three DOFs), the knees (two DOFs), and the ankles (three DOFs), with a total of eight DOFs. Most active exoskeletons currently available actuate on one of the joints, while passive exoskeletons rely on springs or dampers to minimize the strain on the lower limb joints.

Two exoskeletons are described in the next sections, both passive and active.

MIT Ankle Exoskeleton

The Massachusetts Institute of Technology (MIT) exoskeleton was developed by The Biomechatronics Group, one of the research groups within the MIT Media Lab. This exoskeleton features an autonomous electric-powered ankle exoskeleton that augments the walking capabilities of the user, presented in figure 2.7. However, this exoskeleton also includes passive features that aid in the locomotion of the user and decrease the overall weight of the exoskeleton, by eliminating the usage of heavy and large power sources and actuators. In fact, an exoskeleton that adds a spring in parallel with the legs was proved to reduce the metabolic energy consumed in hopping by 24% [56]. On the other hand, the passive features of the MIT ankle exoskeleton can reduce the metabolic cost of walking by 15% [57]. These devices are named quasi-passive exoskeletons.

The active part of the exoskeleton consists of four subsections: fiberglass struts attached to the foot of the user, a unidirectional actuator attached to the anterior part of the struts, lithium polymer batteries, and a controller placed on the waist of the user. Although each battery weighs around 800 g, studies suggest that the exoskeleton reduces the metabolic cost by 80-200%, overcoming the additional mass added by the power sources. Currently, the exoskeleton has an estimated range of 8 km, but it is expected that the number of batteries could increase until a range of 40 km is obtained, while still providing a metabolic benefit [58].

Figure 2.7: MIT ankle autonomous exoskeleton

MIT has also developed a knee joint exoskeleton that features a clutch to lock the knee at peak extension and unlocked during free movement, reducing the metabolic cost by 25%.

ReWalk

The ReWalk, pictured in figure 2.2 (b) on page 9, is an FDA-approved exoskeleton suitable for people who have suffered from spinal cord injuries and are paraplegic. This bilateral exoskeleton actuates on the knee and hip joints so that patients are able to walk and sit. The users can control the movement of the exoskeleton through a remote control while the batteries and controls are stored in a backpack. The exoskeleton uses a closed-loop control system that controls the movements at the hips and knees, while

the ankle joint is articulated using a spring. Sensors in the exoskeleton detect flexion of the upper body and indicate to the system that a step should be initiated, which enables walking at a maximum speed of 22 km/h. As the activation of the exoskeleton is initiated by the user and hip and knee flexion are limited, the exoskeleton prevents falls. Furthermore, the device can be paired with other walking aids to ensure the safety and stability of the user.

Studies conducted with patients using the ReWalk conclude that most users are satisfied with the device and all participants were able to walk 100 m with crutches after 14 sessions [59, 60]. However, for the exoskeleton to be used daily for assistive purposes, several extra sessions are necessary for the user to completely assimilate the control of the device. The main recorded limitations of this exoskeleton are the difficulty in putting on and adjusting the device, as well as the learning period it takes for the user to fully control it.

2.4.2 Upper Limb Biomechanics

The upper extremity of the body consists of the hand, wrist, forearm, elbow, arm, and shoulder complex, as it can be seen in figure 2.8 (a). Excluding the movement of the hand and fingers, the arm has seven degrees of freedom, presented in figure 2.8 (b).

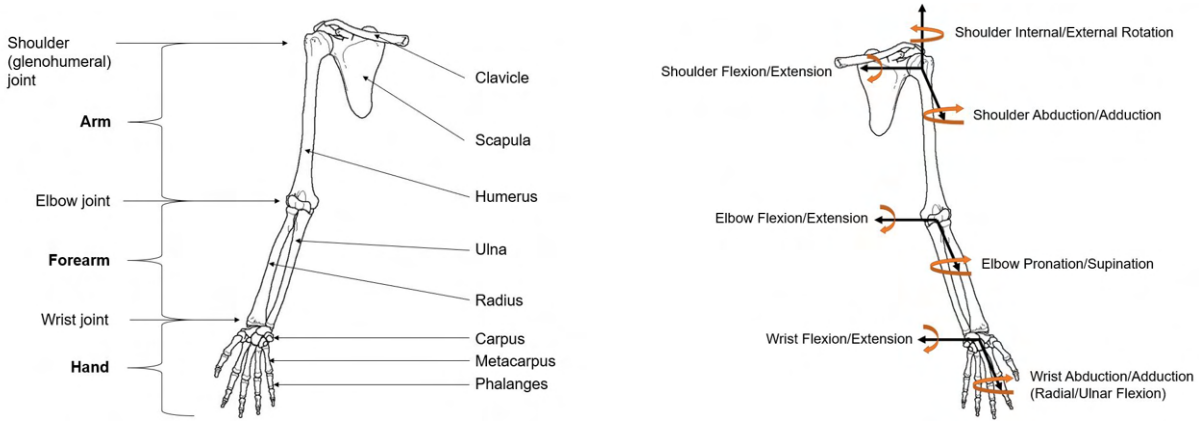

(a) Upper limb parts and main bones of the upper extremity

(b) Degrees-of-freedom of the upper limb

Figure 2.8: Biomechanics of the upper limbs, adapted from [61]

Although the study conducted in [24] provides the ROM necessary to perform the ADLs specified in table 1.2, the anatomical ROM of the arm joints is much wider and will, therefore, be considered when designing the exoskeleton. Figure 2.9 represents the maximum ROM recorded in literature according to [62–64].

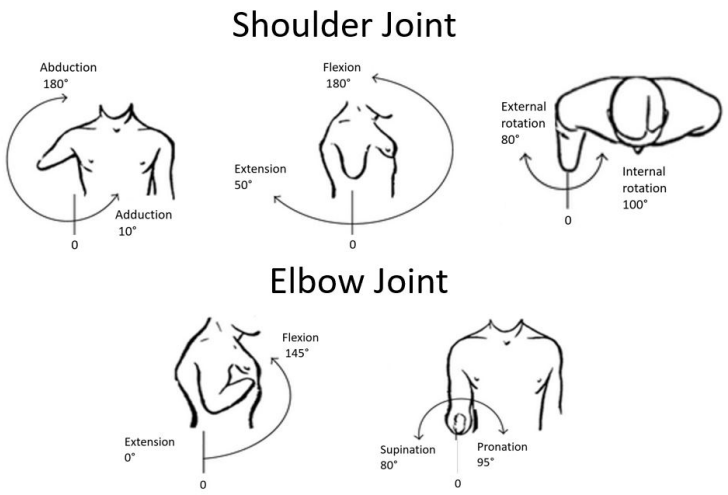

Figure 2.9: Range of motion of the human arm, adapted from [64]

2.4.3 Active Exoskeletons

Active or powered upper limb exoskeletons are often also known as wearable robots. These devices work in parallel with the movement of the upper limbs, enhancing their mobility and providing additional torques for the muscles and the joints.

Actuation Principle

In rigid exoskeletons, the energy is sourced via either pneumatic or hydraulic fluid pressure, or through electric current. The energy source dictates the type of actuation used.

Electric actuation is the most commonly used actuation in exoskeletons, as it is widely available in the market and is easily installed and controlled. However, in comparison with pneumatic and hydraulic actuators, electric actuators have a high impedance and, consequently, cause an increase in stiffness of the exoskeleton. This fact restricts the safety of the exoskeleton, especially when the control system malfunctions. For this reason, there are currently exoskeletons that incorporate an elastic element, such as hydraulic pistons or springs, in series with the electric motor to provide a more secure form of control. In the exoskeleton industry, electric DC motors are more widely used as they provide increased portability and wearability to the system, in comparison with AC motors.

Regarding soft exoskeletons, electric actuation is often used to control tendon-driven structures, especially in hand exoskeletons that usually only require one actuator to provide the user with the ability to grasp objects. In comparison with hydraulic and pneumatic actuators, tendon-driven electric actuators are easier to set up, maintain and install. Furthermore, these systems allow for a more ergonomic design, as the actuators are less cumbersome and provide reliable and straightforward control of the exoskeleton.

Pneumatic actuation is lighter and has a lower impedance in comparison with electric actuation but it is often more cumbersome. In particular, Pneumatic Artificial Muscles (PAMs) are widely used in medical

applications and have been used both in rigid and soft-bodied exoskeletons. These artificial muscles consist of a bladder enveloped with a flexible mesh membrane that is pressurized in order to contract or extend the muscle. PAMs are lightweight and compliant systems, that mimic the biological muscle, resulting in a better experience for exoskeleton users. Furthermore, research on a similar actuation system but using hydraulic fluid has been studied by the Tokyo Institute of Technology, and provides a strength-to-weight ratio five to ten times higher than conventional electric motors and hydraulic cylinders [65].

Hydraulic actuation is the least common type of actuation in active exoskeletons, mainly due to their heaviness and slow response time. Additionally, hydraulic actuators are often noisy, which can negatively impact the user's experience, and potential fluid leaks would be extremely dangerous. Consequently, most exoskeletons that use hydraulic actuators are fixed or used in conjunction with electric actuators.

Furthermore, the use of other actuation principles is being studied and introduced into the exoskeleton market. For example, MR and ER fluids, that have variable viscosity according to the applied magnetic or electric fields, are being studied as means to achieve active variable energy dissipation. Systems using these fluids could provide haptic force feedback, especially applicable to exoskeletons for tremor suppression.

In the following sections, several upper limb active exoskeletons with various actuation principles are analyzed.

2.4.4 Upper Limb Active Exoskeletons

MyoPro

The MyoPro exoskeleton, presented in figure 2.10 (a), is a powered assistive exoskeleton commercialized by Mmyomo and originally developed in a collaboration between MIT and Harvard Medical School, in the early 2000s. Similar to other devices in this section, the MyoPro functions in conformance to myoelectric signals received from the surface of the skin of the user, that activate the motors to move the limbs according to the patient's intentions.

(a) Structure and components of the MyoPro 2 Motion G

(b) MyoPal concept

Figure 2.10: Myomo exoskeletons [66]

There are, at the time of writing this thesis, three models of the MyoPro, that vary in terms of complexity and number of degrees of freedom. The range of motion of each joint is calibrated according to

the user's preferences and their current passive range of motion. Although dependent on the customized device, the MyoPro weighs approximately 1.8 kg and offers the ability to lift objects weighing up to 3.6 kg.

Currently, the MyoPro exoskeleton is only available for adolescents and adults, more specifically veterans. Each device is custom-made to each patient through a fiberglass molding of the patient's arm. Consequently, the MyoPro is highly customized and involves multiple fittings with the patient to ensure maximum comfort and effectiveness. However, presently, a new device named MyoPal is being developed for children that are lightweight and smaller, as shown in figure 2.10 (b). The myopic will be flexible enough to accompany the child's growth and meant to be used both for assistive and rehabilitative purposes. Although the price of the exoskeleton is not explicitly stated on the company's website, as it varies according to the patient, it is sub-intended that the cost is substantial, with the "Neurorehab" directory informing that it surpasses 8500 € [67].

Although clinical case studies have proved the efficacy of the MyoPro in rehabilitating and assisting patients recovering from various conditions, such as chronic stroke and brain injury, some limitations of this device were still observed. One study conducted by Dunaway found that throughout the clinical tests the MyoPro had technical malfunctions and that it can be improved in terms of weight, battery life, and impermeability [68]. Multiple studies also noted the fact that this device is extremely expensive and requires the regular assistance of specialists [69–71].

Power Jacket REALIVE

The REALIVE power jacket developed by Panasonic, presented in figure 2.11, is one of the first soft medical exoskeletons for rehabilitation of the upper-limb movement of patients with one-sided paralysis. This exoskeleton is actuated through compressed air and when the incorporated sensors detect the movement of the unaffected limb of the user, the movement is mirrored on the paralyzed arm. Although Panasonic intended to commercialize the exoskeleton in 2009, it never came to fruition and it was discontinued. At the time of writing this thesis, there are no commercialized soft upper limb medical exoskeletons.

Figure 2.11: REALTIVE power jacket [72]

Single-joint Hybrid Assistive Limb (HAL-SJ)

The HAL exoskeleton is a cyborg-type robot with the objective of supporting and assisting the user's bodily functions, developed by Cyberdyne, a Japanese robotics and technology company. For the upper limb, Cyberdyne offers the single-joint type exoskeleton, presented in figure 2.12. This device assists in the flexion and extension of the elbow joint through a power unit placed in the elbow. The exoskeleton weighs 1.5 kg and can operate for up to 120 minutes. The HAL-SJ controls the movement of the elbow joint by monitoring bioelectric signals of the superficial muscles around a joint or through a small controller that allows the operator to alter the setting and the motion status, as well as to start or stop the device.

Figure 2.12: HAL single-joint type upper limb exoskeleton [73]

Although on the Cyberdyne website the single-joint type HAL is classified as non-medical, this device has been used for rehabilitative and assistive purposes for patients that suffered from a stroke [74, 75]. Both studies conducted followed the post-stroke recovery of patients with upper limb paralysis and concluded that the HAL-SJ is effective in improving the upper limb function in the chronic phase of a stroke, depending on the severity of the injuries sustained by the users. Furthermore, in rehabilitation, the HAL-SJ is extremely useful, as it provides valuable sensory feedback information when performing physiotherapy in a patient.

However, as the exoskeleton only has one degree of freedom, its assistance is limited and can only be used without other structures in the elbow joint. Consequently, the HAL can function as a rehabilitative exoskeleton but not necessarily as an assistive device to help in daily tasks. Furthermore, although there is no specified cost of the single joint HAL, a full HAL suit is expected to cost upwards of 15,000 € [67].

2.4.5 Upper Limb Passive Exoskeletons

As the exoskeleton industry is moving towards adopting softer and less mechanical-appearing exoskeletons, passive exoskeletons have become, in recent years, more appealing. Passive exoskeletons eliminate the need to incorporate actuators that require a large amount of energy to compensate for gravity and, consequently, increase the weight and the size of the exoskeleton. Additionally, passive exoskeletons are, in general, safer than active exoskeletons [76].

The principle of passive exoskeletons is to compensate the force of gravity passively using either counterweights or elastic elements such as elastic bands or springs. As counterweights add mass and inertia into the system, elastic elements are more desirable. Furthermore, although elastic bands introduce nonlinearities into the system, they are more compact than springs.

Although there are numerous passive exoskeletons for the upper limbs, like the ones designed in [77–79], that use springs to compensate gravity, their principle is very similar to the WREX and, consequently, it would be redundant to analyse these exoskeletons. Therefore, only the WREX exoskeleton is described in detail, in section 2.4.6.

2.4.6 The WREX

As described in section 2.1, the Wilmington robotic exoskeleton (WREX) is a mechanical arm orthosis by Jaeco Ortophedic. The main goal of the WREX is to reduce the dependence of its users on others for personal care by providing a zero-gravity experience. According to the manufacturer's website, two similar exoskeletons are available, one for children and one for adults. Both exoskeletons can be made to fit a custom-made bodysuit or a wheelchair.

The WREX has two segments, one for the arm and another for the forearm, connected together through the elbow joint and the shoulder joint, that create a four-degrees-of-freedom exoskeleton, as represented in figure 2.13. It is important to note that the DOF provided by the rotating element placed in the back of the user is not considered as the usage of the solid vest precludes its usage. The elbow joint allows the user movements of elbow flexion and extension and the shoulder's internal and external rotation, while the shoulder joint allows for flexion and extension, and abduction and adduction. However, the supination and pronation of the elbow are not allowed through the exoskeleton, although this DOF is not essential to perform the ADLs defined in table 1.2. For both versions of the exoskeleton, both in metal and 3D printed, the material of the links is steel. For the upper arm link, there are two parallel links that ensure that the elbow joint remains vertical as it rotates. In the wheelchair-mounted version, this link is telescopic and, therefore, adjustable for various upper arm lengths: 15 to 19 cm, 21.5 to 24 cm, 24 to 26.7 cm, and 29.2 to 33 cm. It is, therefore, not suitable to adapt to the growth of a child nor to multiple people. The forearm link is manufactured through a mold and customized for each user. The elastics placed on the joints have different levels of stiffness to accommodate individuals with different arm weights. Usually, the fitting and adjusting during the manufacturing process of the WREX require the children to be present on three separate occasions in the Jaeco Ortophedic laboratory [25]. According to the "NeuroRheab" directory, the price of a WREX ranges from 1700 to 4300 €.

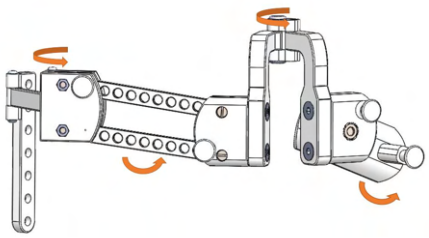

Figure 2.13: CAD model of the WREX and its four degrees-of-freedom

Focusing on the pediatric WREX model, as mentioned in section 2.1, several studies regarding patients' experience with the WREX have been performed. These articles give a powerful insight into the

limitations of the WREX, beyond the fact that it is not adaptable to the size of the user throughout their growth. It is important to note that all the articles described in the following paragraphs conclude that, overall, the patients who use the WREX improve their performance of essential tasks and quality of life.

In a 2006 article by Rahman et al. [25], the experiences of five ambulatory children with arthrogryposis are described. In this experiment, the WREX and a back brace were custom-made, as presented in figure 2.14 (a). Although four of the five children continued to use the WREX throughout the duration of the study, only one relied on it daily to eat. Most of the children had to return to the laboratory more than once for further adjustments and part replacements. The four children who were not home-schooled stated that, due to the fact that removing the device is necessary to make a trip in a car or bus, for example, the transportation and subsequent mounting of the WREX is inconvenient. Furthermore, subjects with ulnar deviation, such as the one pictured in figure 2.14 (b), had much more difficulty using the WREX as it does not provide support for elbow pronation and supination.

(a) Patient using the WREX and their custom-made back brace

(b) Patient that suffers from ulnar deviation using the WREX to eat

Figure 2.14: Ambulatory patients using the WREX [25]

In another study published in 2007 [26], the subjects are 20 non-ambulatory patients from 4 to 20 years-old, that suffer from multiple disorders that impair their arm movements. As the wheelchair-mounted WREX is adjustable to various sizes, four devices were rotated through the subjects while the forearm link was cast for each patient. Most patients reported that the process of removing and attaching the WREX to the wheelchair was impractical and required the help of another person. Furthermore, it was largely reported that the WREX interfered with the joystick of the wheelchair and its tray, and limited the motion of the wrist. Moreover, it is referenced in the study that adjusting the WREX to each individual was a task that required much skill and could only be done by professionals.

More recently, in 2017, another study [19] was performed with 25 children with ages ranging from 2 to 21 years old that used the WREX regularly for up to 25 months, 15 being ambulatory and the remaining non-ambulatory. The exoskeleton was manufactured and fitted by a team that included a physician, a therapist, and an engineer. For young children, the device was well accepted but, as the children grew older, especially the active ambulatory ones, the device was reported to be incommodious and often cause bullying by the patient's peers. Additionally, the parents who participated in the study noted that it is important that the child has someone available to tighten the screws and align the exoskeleton.

Through the observations and conclusions drawn in the three studies described in the previous paragraphs, it is possible to summarize the main aspects to improve on the WREX:

- **The exoskeleton is expensive**: As mentioned in section 1.1, most disabled children live in lower-income households and countries and, consequently, it is likely that a device that can cost up to 4300 € would be unattainable. Furthermore, the fact that the WREX requires multiple fitting sessions in the Jaeco laboratory is prohibitive to families who do not have the means to travel to the US on multiple different occasions. Therefore, the exoskeleton should be obtainable for anyone with access to a 3D printer or via an institution that can afford to make an investment in a 3D printer, to manufacture multiple exoskeletons at a low cost for underprivileged children.
- **The exoskeleton requires multiple fittings and adjustments**: Although the wheelchair-mounted exoskeleton has a telescopic arm link, it is limited to certain sizes and the forearm link is always custom-made. The entire exoskeleton should be adjustable to various users, ages and sizes. Furthermore, the device should not require numerous fittings and subsequent adjustments, that entail the presence of many experts and the patient and be easily adaptable to any person.
- **The exoskeleton is difficult to mount, especially in the wheelchair**: The exoskeleton should be easy to put on and take off, however, as most patients lack movement in both arms to different degrees, it is difficult to create a device that would not require the help of another person. Nevertheless, the exoskeleton should have an easy and intuitive assembly that allows for anyone without any previous knowledge to be able to mount it. Additionally, to reduce mounting and dismounting, the exoskeleton should be comfortable and rigid enough to withstand everyday usage.
- **The exoskeleton is difficult to transport**: The device should be more portable. Either the child should be able to wear it in any circumstances without being uncomfortable or risking damaging the parts, or the parts should be bendable or retractable to allow for compact storage.
- **The exoskeleton restricts movement**: The joints should be less rigid and allow for fluid movement, and not interfere with the movement of the wrist. The exoskeleton should aid in elbow pronation and supination which is extremely important for patients with ulnar deviation. For this reason, a wrist or hand orthosis could be incorporated.
- **The exoskeleton is cumbersome and incommodious**: The exoskeleton should be less mechanical-looking and more aesthetically pleasing. Furthermore, it should be less bulky and have a better connection with the body of the user, so that it moves in accordance with what the user intends and does not interfere with the environment. For the exoskeletons that are mounted to a body orthosis, the device becomes even more inconvenient as this orthosis severely constricts the movement of the user. Consequently, a new form of attaching the exoskeleton to the patient that is suitable and comfortable for both ambulatory and non-ambulatory users should be designed.

Although some of these challenges can be directly addressed through 3D printing, others have to be mitigated through a redesign of the exoskeleton. In the next section, solutions are provided and tested in order to improve the WREX in both these areas.

Chapter 3

First Prototype

The first step in the project of the exoskeleton is to design and construct a preliminary prototype in order to identify its limitations and better understand the challenges of 3D printing using polylactic acid (PLA) filament and how to solve them.

This chapter focuses on the process of 3D printing the first prototype. In the first section, various 3D printing processes are described. The process of Fused Deposition Modeling (FDM), used to print the prototype, and its parameters are presented and thoroughly analyzed. Then, the filaments used to manufacture the prototype are characterized and, after the WREX model is completed, the prototype is designed. Finally, with the physical model of the prototype printed, areas of improvement are identified.

3.1 3D Printing

The traditional way for the industrial production of solid objects is subtractive manufacturing. This type of manufacturing, as the name suggests, consists of removing material from a solid block, using processes such as milling or lathe, until the final shape is obtained. However, in the 1980s, a new form of manufacturing, named Additive Manufacturing (AM) and also known as 3D Printing (3DP), was introduced. This form of production is the opposite of subtractive manufacturing as it consists of adding layers of a certain material to create a three-dimensional part. Therefore, 3D printing allows for the manufacturing of more complex shapes while wasting less material as it is not dependent on indirect consumables such as molds and fixtures.

As 3DP patents created in the past by pioneers of the field are expiring and the processes are being improved, this technology is becoming increasingly more accessible not only for manufacturers but also for personal use. In fact, according to a study [80] conducted by Reichelt Elektronik that surveyed 1000 UK consumers in 2018, 6% of the people claimed to own an AM system while 17% showed interest in acquiring one. Furthermore, as per the 2018 Wohlers Report [81], around 550,000 desktop 3D printers were sold in 2018, almost twice the amount of the same sales in 2015.

On a larger scale, the use of 3DP in industries is also increasing. According to the 2021 Wohlers Report [82], the 3D printing industry grew 7.5% despite the COVID-19 pandemic. This number, despite

being lower than the 27.4% average of the last ten years, means that, at the end of 2020, the additive manufacturing market has expanded to almost 11 billion euros.

The manufacturing of 3D printed parts can be done through multiple processes, as presented in the diagram in figure 3.1, in which the material is deposited, joined, or solidified, while controlled by computer software for Computer-Aided Design (CAD) and Manufacturing (CAM).

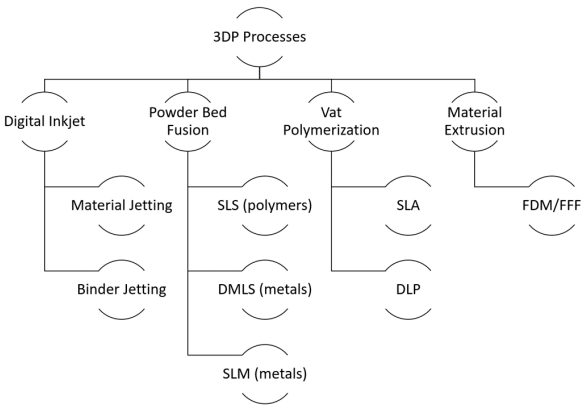

Figure 3.1: Principal 3D printing processes

A summary of the main processes and their most important characteristics are presented in table A.1 of appendix A. As the 3D printing process used to construct the prototype is Fused Deposition Modelling (FDM), only this process is described in the following section. Further information regarding the 3DP processes presented in figure 3.1 is available in appendix A.

3.1.1 Fused Deposition Modelling (FDM)

The most widely used 3D printing process, holding about a 69% share in 3D printing technologies [83], and the one used to manufacture the exoskeleton in the present thesis, is Fused Deposition Modelling (FDM), also known as Fused Filament Fabrication (FFF). This process was developed in the early 1990s and consists of heating plastic filament until plastified and depositing a layer in a heated bed through a heated extruder to build a 3D part according to the CAD data provided to the printer. The nozzle is mounted on a mechanical stage that moves in the x-y plane to produce the desired geometry of a layer, as represented in figure 3.2. Once a layer has been constructed, the platform moves in the z-direction to begin the next layer. Each layer quickly solidifies and bonds with the previous one.

In FDM, a computer program transforms the CAD model into G-code, a commonly used CNC programming language. In a process commonly known as slicing, the software mathematically orients and divides the part into layers. Afterward, the program combines movement, extrusion, heating, and sensing commands together in a sequence that is interpreted and executed by the 3D printer. The various printing parameters selected by the user and read by the 3D printer strongly influence the quality of the final product. These parameters must be optimized to maximize the dimensional accuracy, surface finish, and mechanical properties of the components while also taking into account economic factors such as printing time and the quantity of filament necessary to operate. As these process variables strongly influence the final result of the 3D printing process, there are several studies in literature that establish

an experimental relationship between these factors and the mechanical properties of the final product.

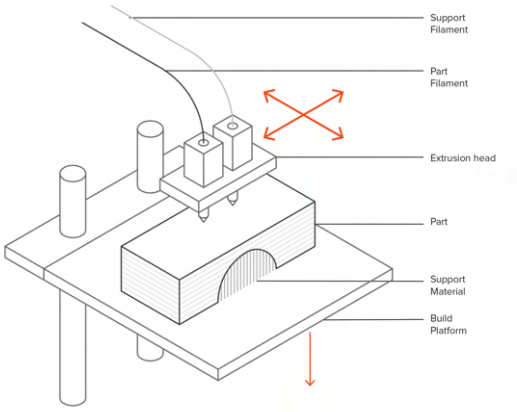

Figure 3.2: Schematic the FDM 3D printing process [84]

One of the most important parameters to take into account is the infill density and the shell, or wall, thickness. To reduce the print time and the quantity of material consumed, FDM parts are generally not solid. This means that each layer is composed of an outer shell that traces the outer perimeter of the part, and the interior is filled with a low-density structure named the infill. A 0% infill density means that a part is hollow while a 100% infill creates a solid part, as schematized in figure 3.3.

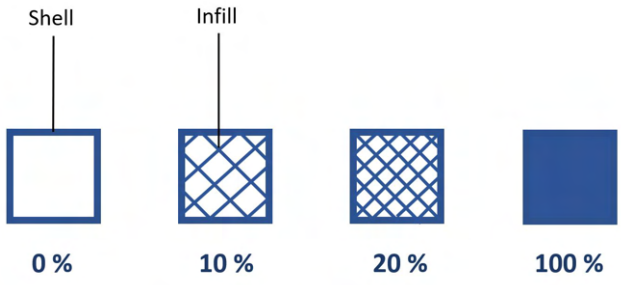

Figure 3.3: Internal geometry of FDM printed parts with different infill density

The infill percentage is one of the most important parameters to consider when 3D printing a part, as it strongly influences its mechanical properties. In an article [85] written by H. Gonabadi et al. and published by The International Journal of Advanced Manufacturing Technology that explores the influence of various printing parameters in the mechanical properties of the parts, the following stress-strain curve of tensile test pieces with different infill percentages was obtained. In figure 3.4 it is clear that, although parts with a higher infill percentage have higher Young's modulus and ultimate tensile strength, they also become more brittle as the infill percentage increases.

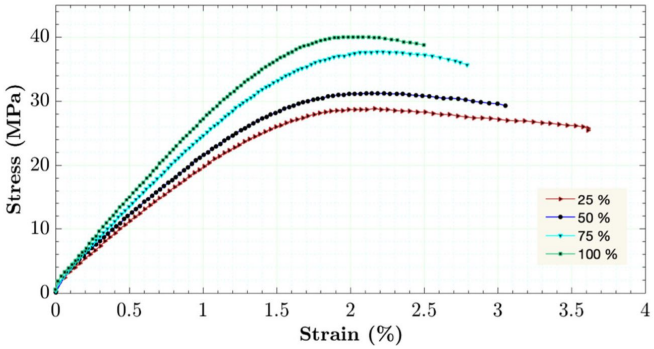

Figure 3.4: Tensile stress-strain curves for different infill percentages of 3D FFF-printed PLA [85]

The adhesion between each layer is also an important factor when considering 3D printed parts, and the bond strength between the different layers is lower than the base strength of the material. Consequently, FDM parts are anisotropic: their strength in the z-direction is always lower than in the x-y plane. Therefore, the best mechanical properties are obtained when the deposition orientation direction is the same as the direction of application of the tensile load, as represented in figure 3.5.

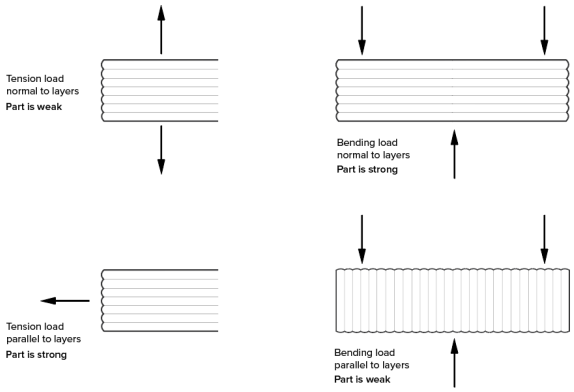

Figure 3.5: Print orientation and its influence on a parts' strength in a certain direction [84]

For this reason, print orientation is extremely important to assure that the part has the best possible mechanical properties. In fact, in the article written by H. Gonabadi et al. mentioned previously [85], the effect of print orientation in the stress-strain curve of tensile test pieces was notable, as presented in figure 3.6.

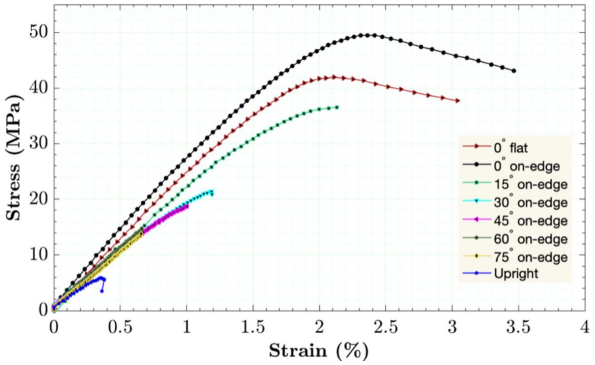

Figure 3.6: Tensile stress-strain curves for different build orientations of 3D FFF-printed PLA [85]

A summary of other important parameters to take into account and their influence on the properties of the 3D printed parts are presented in table A.2 of annex A.

Warping is a common defect in FDM printed parts as when the material solidifies and cools, it contracts. Differential cooling introduces internal stresses that cause the part to deform. This defect can be prevented by controlling the bed temperature and by increasing its adhesion to the part. Using fillets instead of sharp edges not only increases the structural integrity of the part but also helps mitigate warping. Other design best practices followed throughout this thesis are described in length in volume 25 of the book "Additive Manufacturing" [86] and in [87].

Although FDM has improved greatly in recent years, since the first patents expired, there are still many challenges to overcome to make FDM a viable solution for mass production in various fields. One of the main challenges of this 3DP technology for applications that require high-quality parts is obtaining adequate dimensional accuracy, especially for complex parts, and reduced surface roughness. For these reasons, post-processing might be necessary not only to remove support structures but also to provide a good surface finish. It is, however, important to note that for industrial FDM the accuracy significantly improves from ± 0.15% with a lower limit of ± 0.2 mm for desktop FDM 3D printers to ± 1% with a lower limit of ± 1.0 mm, and the support structures are water-soluble, which improves the overall quality of the final product [84].

Currently, the most commonly used materials in FDM are thermoplastics such as acrylonitrile butadiene styrene (ABS) and polylactic acid (PLA). However, this technology can work with a wide range of materials, and, recently, there have been successful uses of metallic, ceramic, bioglass, carbon fibers, and biological materials [88]. The most commonly used filaments in FDM printing and their characteristics, based on the software Optimatter, are presented and compared in figure 3.7.

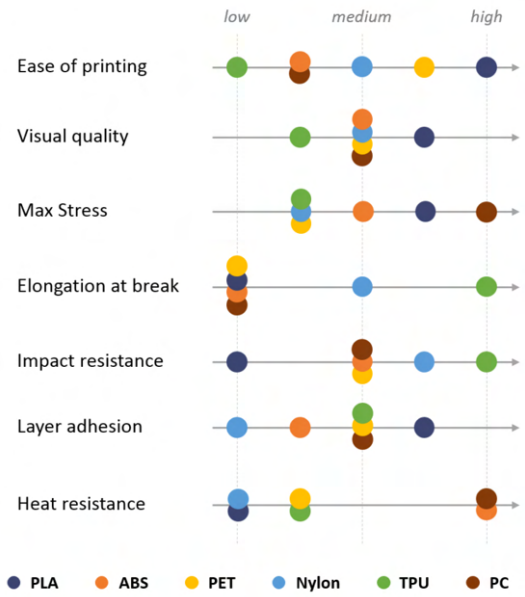

Figure 3.7: Comparison of the characteristics of six commonly used polymers in FDM [89]

In the future, it is expected that more materials will be able to be 3D printed, especially biodegradable and sustainable materials. Furthermore, material waste is expected to be eliminated by using supportless

prints. Furthermore, to overpass the limitations of FDM, the hybridization of this process with other 3DP technologies, to enhance the dimensional accuracy and resolution of 3D prints, is being studied [90]. In terms of software, real-time monitoring and control of the 3D printer are being developed so that necessary calibrations can be implemented throughout the process, improving the quality of the final part [91].

3.2 PLA Filament

Polylactic Acid (PLA) is the thermoplastic polymer used in the construction of the WREX, as well as in the exoskeleton designed in this thesis. PLA is a biodegradable material that is relatively inexpensive, making it one of the most commonly used materials in FDM 3D printing. It is also biobased, as it is obtained by fermenting a product with a high amount of carbohydrates, usually sugar cane or corn. In the case of the latter, the starch is separated from the corn and mixed with acid or lactic monomers to form dextrose. Afterward, lactic acid is produced through glucose fermentation, creating the main component of PLA. Furthermore, PLA filament is one of the easiest to print with as print temperature is lower than other materials such as ABS, enabling better surface details and features, and it is not as susceptible to warping and clogging. Additionally, PLA is available in a large range of different colors, which allows for easy customization of the exoskeleton according to the user's preferences. As children place great importance on colors, it is likely that the exoskeleton would be perceived as more aesthetically pleasing and encourage regular usage of the orthosis.

The filament used during the course of this thesis is TECBEARS PLA transparent filament with the characteristics indicated in table 3.1.

Table 3.1: Characteristics of the PLA filament used, provided by the manufacturer

Diameter	1.75 mm
Dimensional Accuracy	± 0.02 mm
Recommended extrusion temperature	200℃ - 230℃
Recommended bed temperature	60℃ - 80℃

As the mechanical properties of the PLA filament are not provided by the manufacturer and the properties of the final part are strongly influenced by the printer parameters, the stress-strain curve obtained by H. Gonabadi et al., presented in figure 3.8, and the resulting data will be considered. These properties concern PLA FDM printed parts with a 25% triangular infill, a shell thickness of t = 1.2 mm, and a flat orientation, and are presented in table 3.2. As the ultimate compressive strength can not be obtained through the uniaxial tension test, the value of this property was obtained through the information provided by MakerBot for a standard resolution and infill in [92].

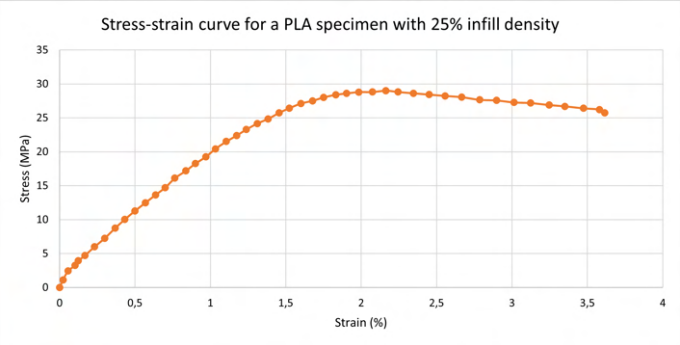

Figure 3.8: Graphic of the stress-strain curve obtained for a PLA FDM printed specimen with a 25% triangular infill [85]

Table 3.2: PLA mechanical properties, considering a 25% triangular infill density [85], [92]

Ultimate tensile strength (MPa)	29
Ultimate compressive strength (MPa)	17.9
Ultimate tensile strain (%)	2.15
Poisson's ratio	0.31
Elastic modulus (GPa)	2.05
Failure strain (%)	3.4

3.3 TPU Filament

The parts that connect the exoskeleton to the wearer's body can not be manufactured with PLA, as their material must be flexible to adapt to the user's limb and its dimensions, and comfortable. Therefore, the parts in direct contact with the user's body are printed using Thermoplastic Polyurethane (TPU) filament.

TPU is a durable and flexible thermoplastic elastomer that is smooth and comfortable on the skin and can be 3D printed with a standard desktop FDM printer. TPU consists of a linear segmented block copolymer with alternating sequences of hard and soft segments whose ratio and molecular weight of the reacting compounds create a large variety of different properties and flexibility. TPU has good mechanical properties, with high tensile strength and elongation at break, and resistance to abrasion and wear.

However, 3D printing TPU entails some difficulties, primarily since TPU filament is hygroscopic. For this reason, it absorbs moisture extremely easily when openly in contact with the environment. Therefore, this filament should always be kept in a low humidity environment, ideally in an air-tight package. On the other hand, TPU should also be printed in low velocities in comparison with PLA printing and the speed should remain constant, to avoid clogging the extrusion head, which is especially important in non-direct extruders. Additionally, TPU is printed at a higher temperature than PLA.

The TPU filament used to 3D print the prototype is the GEEETECH TPU gray filament, whose characteristics are presented in table 3.3.

Table 3.3: Characteristics of the TPU filament used, provided by the manufacturer

Diameter	1.75 mm
Dimensional Accuracy	± 0.05 mm
Recommended extrusion temperature	190℃ - 220℃
Recommended bed temperature	50℃ - 60℃

3.4 CAD Model

The CAD model for the 3D printing process is designed taking the WREX model as a starting point. SolidWorks [93] is the software used throughout this thesis for modeling purposes. The new exoskeleton design should tackle the main problems that the WREX suffers from, as mentioned in section 2.4.6. Therefore, the redesigned exoskeleton should be:

- Adjustable to various users of different ages and sizes;
- Easy to put on and take off, without requiring multiple fittings;
- Less rigid and allow for better movement, minimizing the interference with the environment;
- Comfortable and aesthetically pleasing.

Furthermore, the WREX design must also be modified taking into account design guidelines that facilitate the 3D printing process and maximize the mechanical properties of the final part.

It is also important to note that, although standards concerning medical exoskeletons were researched with the intention of following existing norms throughout the design process, there are still no ASTM or ISO standards available for medical assistive exoskeletons. At the moment, the standards available concern mostly industrial exoskeletons or rehabilitative medical robotic devices [94]. In fact, the ISO 13482:2014 standard, ”Robots and robotic devices — Safety requirements for personal care robots”, solely includes non-medical exoskeletons in its scope. However, in 2017, ASTM international created the F48 committee dedicated to creating various exoskeleton standards to be followed by manufacturers and various standards relevant to the present thesis are currently in development [95].

However, as the exoskeleton is considered a medical device, the Medical Device Reporting (MDR) regulation, that contains mandatory requirements for manufacturers published by the US Food and Drug Administration (FDA) can be consulted. Similarly, ISO 20417 for medical devices includes product information regulations and ISO/TR 20416 provides guidance on monitoring the safety, performance and usability of the device in everyday use [96].

3.4.1 WREX CAD Model

The original WREX CAD model was obtained through the website GrabCad, available in [97]. To convert the 3D model to SolidWorks, Alibre, the original software, was downloaded to obtain the dimensions and the geometry of the parts in order to redesign the exoskeleton. As the solid vest to which the

exoskeleton arms are attached is not available in the model downloaded, one was modeled, according to pictures and dimensions provided by JAECO, as illustrated in figure 3.9.

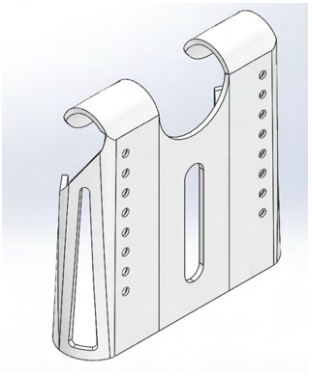

(a) CAD model of the WREX vest

(b) WREX mounted on a rigid vest

Figure 3.9: WREX vest

Afterward, the parts were assembled to create a model, presented in figure 3.10, consistent with the real WREX.

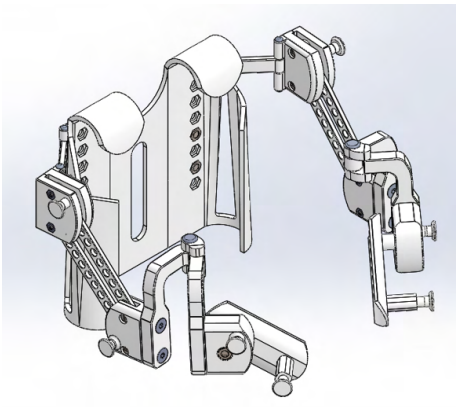

Figure 3.10: WREX redesigned CAD model in SolidWorks

This assembly features various connecting elements, mainly standardized fasteners and nuts that are cataloged in table 3.4. However, some elements, specifically the pins that allow rotation in the shoulder and the elbow joint were not industrially available and were designed solely for the exoskeleton.

Table 3.4: WREX standardized connecting elements and respective designation

Number of Elements	Designation
12	Nut: ISO 4035 - M8
2	Nut: ISO 1034 – M8
4	Screw: ISO 1207 – M8 X 16
2	Screw: ISO 1208 – M8 X 35
8	Screw: ISO 1207 – M6 X 20
8	Screw: ISO 10642 – M8 X 16

3.4.2 Prototype CAD Model

The WREX parts presented previously were then modified to construct the prototype CAD model, presented in figure 3.11. Each part and the respective modifications are described in the following sections.

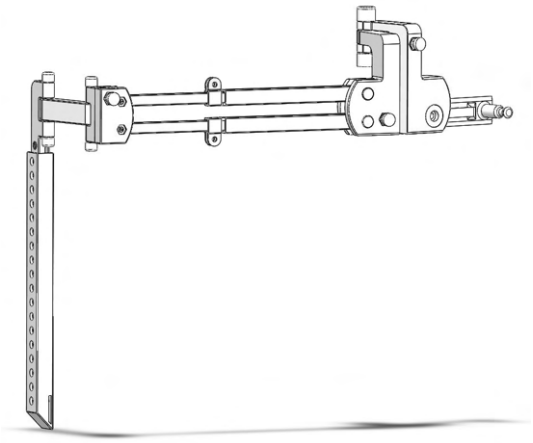

Figure 3.11: CAD model of the first prototype

Forearm Link

The forearm link is the part that connects the exoskeleton to the forearm of the user. In the WREX, this connection is made through two Velcro straps, as seen in figure 3.9 (b), and the forearm link is made out of polyethylene, a lightweight and durable thermoplastic that is not 3D printed. Instead, this link is custom-made for each user, through the casting of the forearm to obtain a mold [26]. To provide maximum comfort, a solid foam material is usually applied to the interior of this part, in contact with the skin of the wearer.

As pictured in figure 3.12 (a), the forearm link of the CAD WREX model is a thin curved part, to fit the forearm of the user, with an element that connects to the forearm joint and other that support the elastic. A second part, presented in figure 3.12 (b), is connected to the red surface of the forearm link, where the elastic is placed. The blue circular surface is mounted to the inside of the forearm joint with a pin that allows for rotation. The pin is held in place by a nut placed on the green surface.

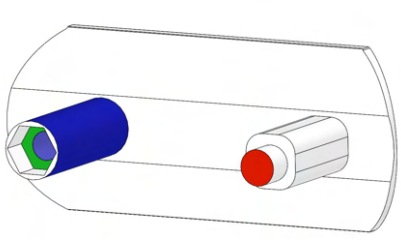

(a) WREX CAD model of the forearm link

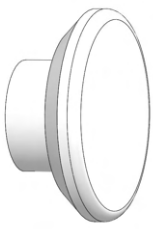

(b) WREX CAD model of the forearm link elastic support feature

Figure 3.12: Forearm link of the WREX

For the prototype model, various changes were made to the original part. Firstly, the elastic support element is incorporated into the actual part, to increase strength and facilitate the manufacturing process. On the other hand, the connection between the forearm link and the joint introduces a critical section where the part would most likely fail due to friction between the two parts, represented in red in figure 3.13 (a). Furthermore, the friction between the two surfaces of the joint and of the link could also cause failure. For this reason, a new connection was modeled, as seen in figure 3.13 (b), that reduces the wear of the forearm joint. The new mechanism introduces a new part, represented in gray, that rotates as the forearm link rotates, reducing the friction between the two parts.

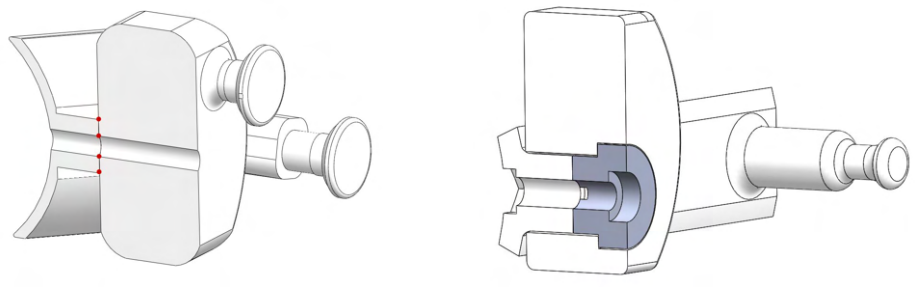

(a) WREX CAD model of the connection between the forearm link and joint

(b) CAD model of the new connection between the forearm link and joint

Figure 3.13: CAD model of the connections between the forearm link and joint

Although the printing process would be facilitated if the part had a large flat surface, this is not possible as the part should adapt to the forearm of the user. Therefore, supports are used during the printing process so that the part is printed in the most favorable orientation. However, to fit a larger range of users of various ages and sizes, the curvature of the part is decreased and so is its height. On the other hand, the length of the forearm link is increased to 14 cm, to fit both a 2-year-old child and an adult. Additionally, the Velcro straps responsible for securing the part to the forearm of the user are substituted for a single-wide 3D printed TPU strap, placed in the middle of the forearm joint and adjustable to the forearm circumference of the user, according to the dimensions presented in table 1.1, as illustrated in figure 3.14.

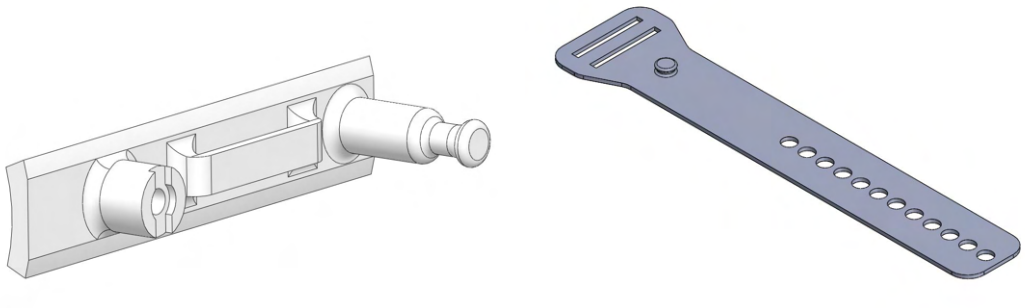

(a) CAD model of the redesigned forearm link

(b) TPU strap

Figure 3.14: Redesigned forearm link

Elbow Joint

The elbow joint allows the elbow's flexion and extension and is composed of two parts that rotate around each other: the forearm joint, colored in blue, and the arm joint, colored in pink in figure 3.15.

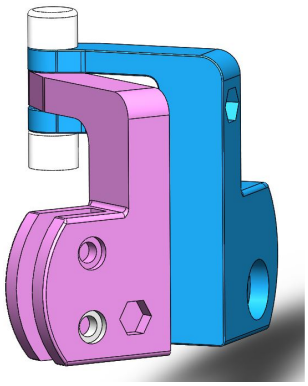

Figure 3.15: CAD model of the elbow joint and its components

Forearm joint In the WREX CAD model, seen in figure 3.16 (a), the forearm joint is composed of two separate parts connected through two bolts. This design hampers the mounting of the exoskeleton and decreases the joints' mechanical resistance. Therefore, in the redesign of the forearm joint, the two parts are combined into one. However, as this eliminates flat faces that would serve as the base surface for the printing process, and printing the part vertically would decrease its mechanical strength, the element where the elastic is placed is made into a separate part. As presented in figure 3.16 (b), the part where the elastic is placed so that the red surfaces are coincident, which also allows for easier placement of the elastic band. Furthermore, the top part of the WREX forearm joint where a pin is placed was also altered to increase the mechanical resistance and decrease the risk of failure when connecting the part to the upper arm joint. Other modifications were made to accommodate the new connection between the forearm joint and the link, illustrated in figure 3.16 (b).

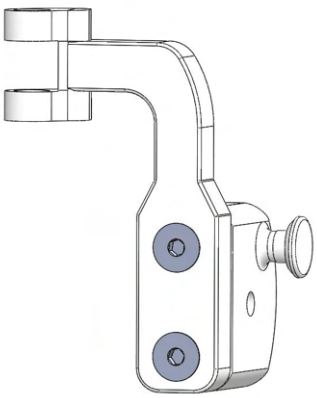

(a) WREX CAD model of the forearm joint

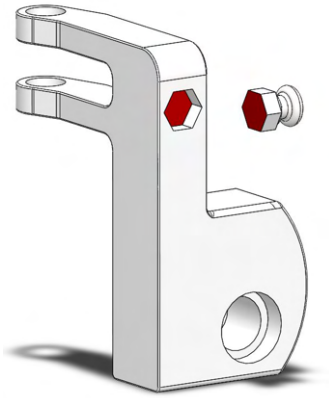

(b) CAD model of the redesigned forearm joint

Figure 3.16: CAD models of the forearm joint

Arm joint The WREX CAD model of the arm joint is similar to the forearm joint except for the fact that there is an introduction of certain features that allow the connection to the arm link. This connection is made through a bolt with a threaded tip and a nut that secures this element. The arm link is then placed in the unthreaded part of the bolt, mimicking the shoulder's flexion and extension.

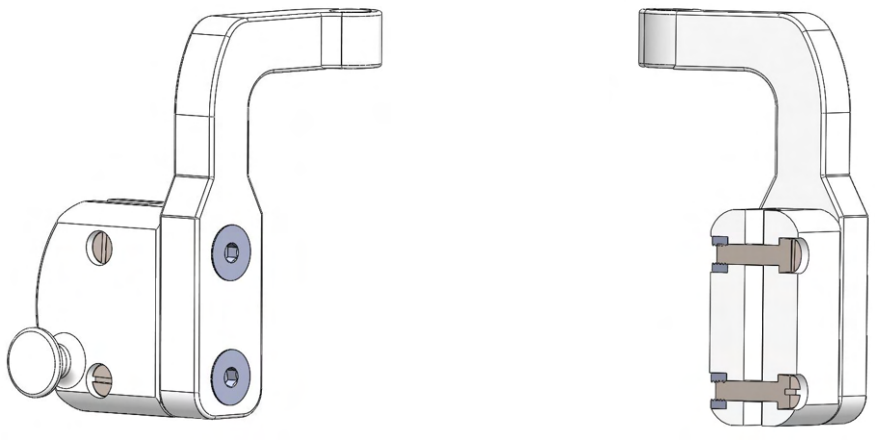

(a) WREX CAD model of the arm joint

(b) WREX CAD model of the arm joint with a cut to its connection to the arm links

Figure 3.17: WREX CAD models of the arm joint

The redesigned arm joint, illustrated in figure 3.18, is similar to the redesigned forearm joint as the two parts were combined into one and a flat surface was created to provide the most favorable printing orientation. Furthermore, the nut was no longer necessary as the threaded tip of the bolt is secured to a thread in the part itself, securing this feature.

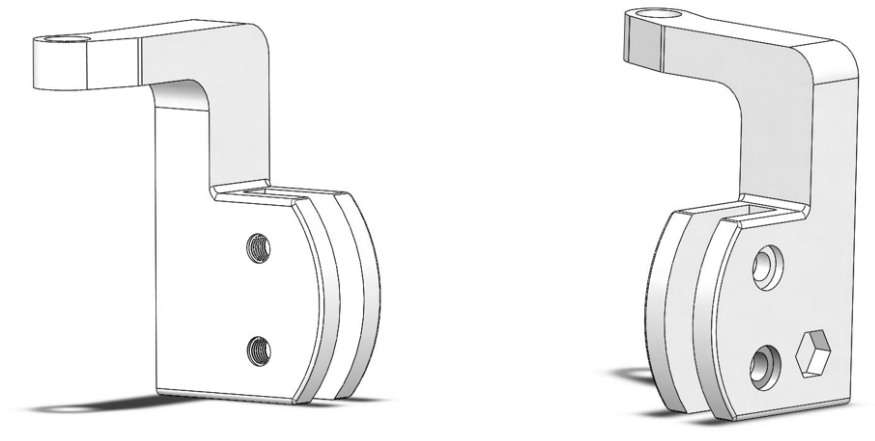

(a) CAD model of the redesigned arm joint

(b) CAD model of the redesigned arm joint and the feature where the bolt is placed

Figure 3.18: CAD models of the redesigned arm joint

Arm link

As mentioned previously, the exoskeleton should be adaptable to multiple people and fit the same user throughout their growth. For this reason, the arm link is a crucial element that should extend and retract to the length of the upper part of the user's arm. As referenced in table 1.1, the minimum length of this link should be 17.3 cm, to fit a 2-year-old child, and extend to 36.6 cm, to fit an average adult.

For this purpose, various options were explored and, for each one, a sample was 3D printed to assess structural resistance and examine the ergonomics of the design.

The first option is the most similar to the original WREX design but features a telescopic rail, modeled in figure 3.19. This design requires two B18.3.4M – 8x1.25 bolts and allows for an extension from 17.3 cm to 34.0 cm, which does not fulfill the objective to fit an average adult. The 3D printed sample, pictured in figure 3.20, fractured in the section circled in blue, and was extremely fragile, particularly in bending. For these reasons, this option was discarded.

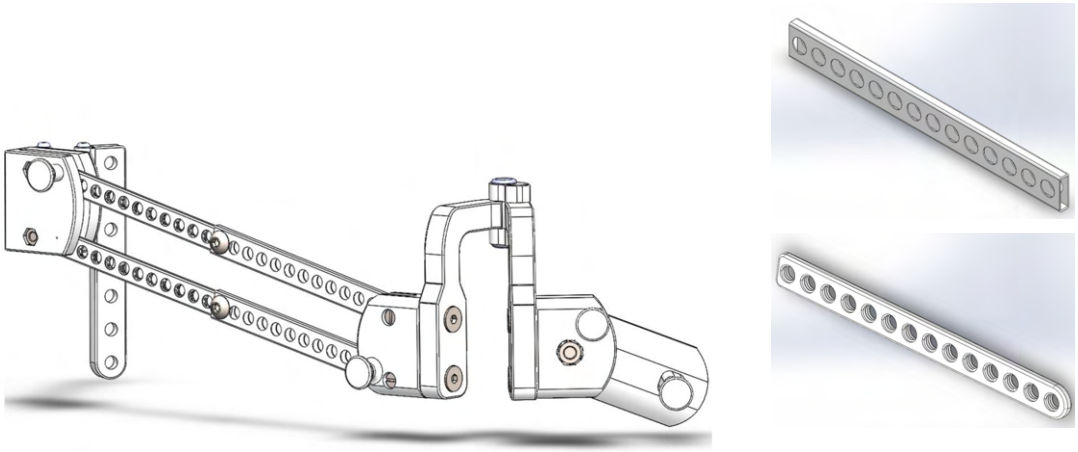

Figure 3.19: CAD model of the first option of the arm link

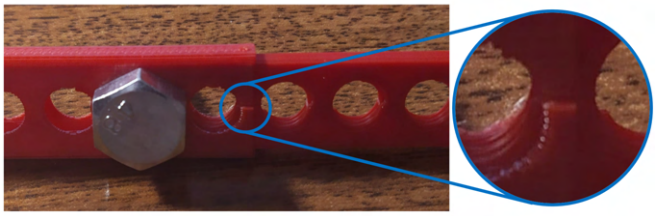

Figure 3.20: 3D printed sample detail of the first option

The second option is presented in figure 3.21 (a) and is similar to the first except for the fact that the width of the cross-section is increased, to enhance the rail's strength. In this option, the cross-section of the parts is a square and, for this reason, the 3D printed sample, pictured in figure 3.21 (b), did not fracture and was more resistant, particularly in bending. However, this option contributes more to the mechanical appearance of the exoskeleton, making it more cumbersome and also increasing the interference with the environment. Furthermore, the fact that there are holes for the bolt throughout the entirety of the length of the parts decreases its mechanical strength. Consequently, a third option is explored.

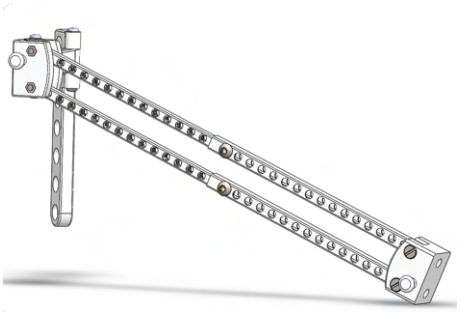

(a) CAD model of the second option of the arm link

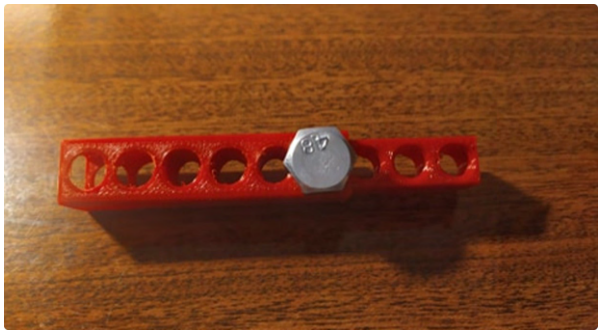

(b) 3D printed sample of the second option

Figure 3.21: Second option of the arm link

The concept of the third option was influenced by the telescopic locks available in the market and presented in figure 3.22.

Figure 3.22: Various types of telescopic locks available in the market [98]

Thereupon, the third option features a lock that is tightened and untightened through a bolt, as presented in figure 3.23 (a). This option eases the length adjustment process for the user, in comparison to the previous options, as the bolt does not need to be completely removed from the part, but only tightened when the intended position is reached. The 3D printed sample, pictured in figure 3.23 (b), used the same telescopic rails as the second option, to reduce material waste.

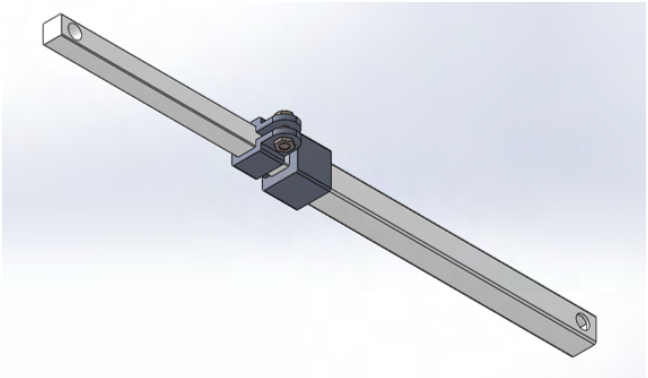

(a) CAD model the third option of the arm link

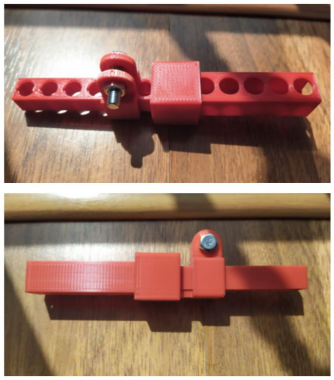

(b) 3D printed sample of the third option of the arm link

Figure 3.23: Third option of the arm link

The present option has a more ergonomic design in comparison with previous ones and also allows for the width of the cross-section of the rails to be decreased, creating a less incommodious design. However, some improvements were made before the manufacturing of the prototype, namely to simplify the 3D printing process and to increase the mechanical strength of the part, and the lock was combined into the outer telescopic rail, as presented in figure 3.24.

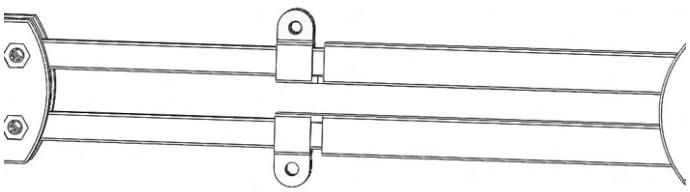

Figure 3.24: CAD model of the final option selected for the arm link

Shoulder joint

The shoulder joint is composed of two parts that are joined together via threaded bolts, as shown in figure 3.25.

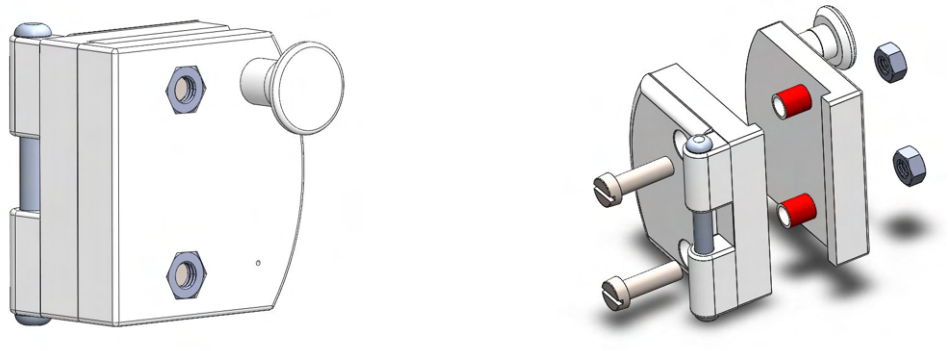

(a) WREX CAD model of the assembled shoulder joint

(b) Exploded view of the WREX CAD model of the shoulder joint

Figure 3.25: WREX CAD model of the shoulder joint

One of the main problems of the shoulder joint is that the arm link parts move freely around and throughout the surfaces colored in red, hindering the ease of movement of the user. For this reason, as presented in figure 3.26, the redesigned shoulder joint axle features a notch where the arm link is placed, restricting its movement along the joint. Furthermore, the axle is placed through the blue surface of the other part of the shoulder joint, securing the connection between the two parts. Similar to the elbow link, the pin is 3D printed and the elastic support element is a separate component that is subsequently assembled into the part, creating a flat surface to facilitate the printing process.

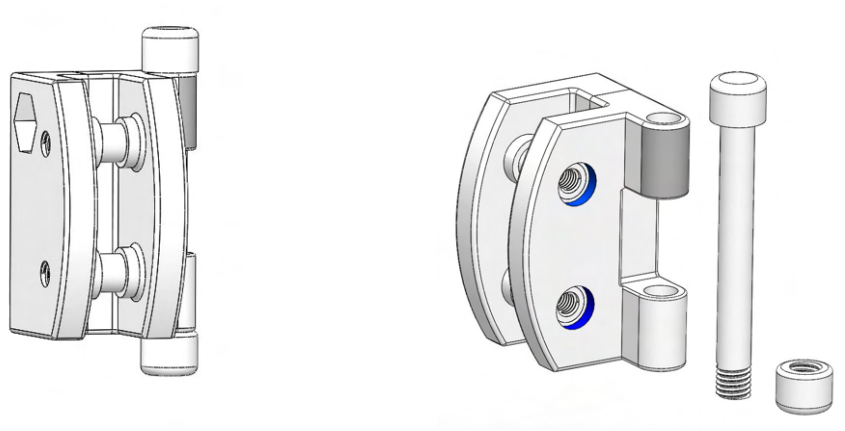

(a) Redesigned CAD model of the assembled shoulder joint

(b) Redesigned CAD model of the shoulder joint and its pin

Figure 3.26: Redesigned CAD model of the shoulder joint

Shoulder link

The shoulder link connects the shoulder joint to the back link. The only changes made for the redesigned exoskeleton are increasing the width of the cross-section and maintaining it constant throughout the part, to increase the resistance of the component and to avoid sharp edges, as presented in figure 3.27.

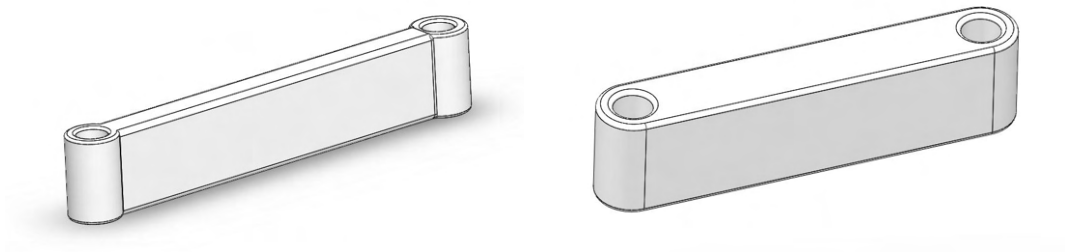

(a) WREX CAD model of the shoulder link

(b) Redesigned CAD model of the shoulder link

Figure 3.27: CAD model of the shoulder link

Back link

Originally, the back link is attached to the vest but, in the redesign, the back link is secured directly to the user's body, as presented in figure 3.28. In the upgraded exoskeleton, the back link is secured to the chest and to the hips of the user via straps that go through the telescopic rails. As mentioned in table 1.1, a strap that surrounds the hips, or the chest, of an adult user would have to measure 94.8 cm, which is impossible to print in a standard desk FDM 3D printer. Therefore, the straps must be substituted by a ribbon or a belt. For the link to be adjustable through the growth of the user, it must extend from 24.4 to 52.0 cm. Although a telescopic lock mechanism similar to the one selected for the arm links could be used, a telescopic rail similar to the second option of the arm link presented previously is employed to explore which option is, in reality, more ergonomic for the user and more structurally sound.

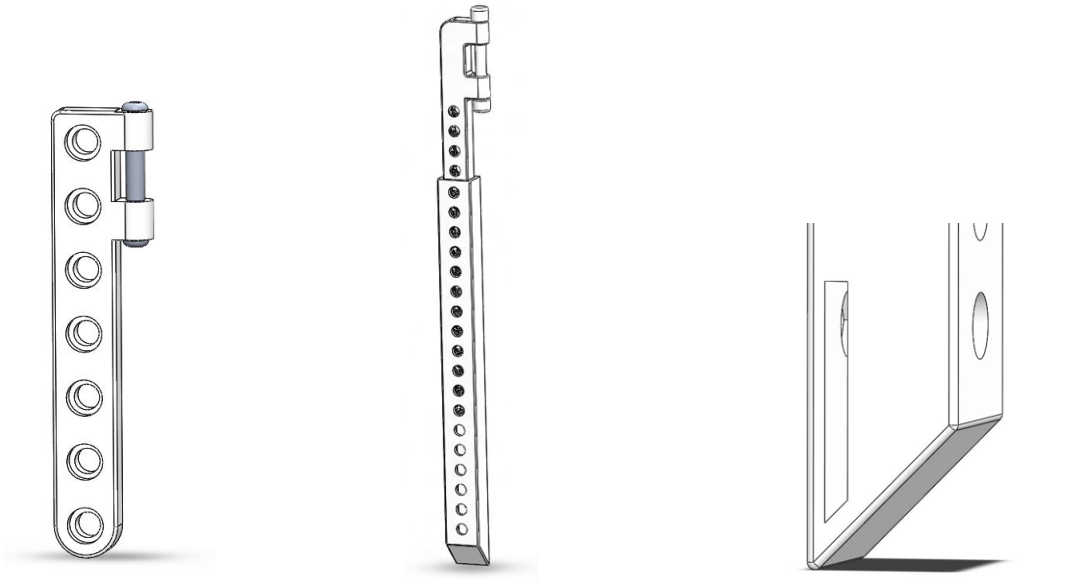

(a) WREX CAD model of the back link

(b) Redesigned CAD model of the back link

(c) Detail of the redesigned back link

Figure 3.28: CAD models of the back link

3.5 3D Model Printing

In order to 3D print the redesigned CAD model, a Creality CR-10 printer [99] was used, whose properties can be consulted in table A.3 of appendix A. Furthermore, for high quality 3D printed parts, the printing parameters presented in table A.4 of appendix A, were inserted in the software Simplify3D [100], which converted the STL part files into G-Code.

The parameters implemented are obtained through various sources, specifically [101–104], and through experiences with multiple samples, testing different properties and reaching an improved solution for the printer parameters. It is also important to note that, for the manufacturing process of the first prototype, an infill of 8%, and not the 25% mentioned previously in section 3.2, is set to save both time and filament. For TPU, the parameters used are extremely important to ensure a successful print and were obtained through trial and error and various failed prints. Firstly, as TPU is a flexible material, clogging often occurs, especially when the 3D printer features a Bowden extruder, as is the case in Creality CR-10. To mitigate this problem, the speed is low and must remain constant throughout all printing phases, retraction is disabled, and the extruder temperature is increased to 230 °C.

According to the properties presented above, the redesigned parts described in the previous section were printed and the time and quantity of material used to print each part are presented in table A.6 of appendix A. Before printing each part, the bed was covered in hair spray to increase adhesion to the printing platform and reduce warping.

3.6 Areas of Improvement

3.6.1 General Observations

The 3D printed first prototype of the exoskeleton, being worn while performing the ADL of brushing hair, is photographed in figure 3.29.

Figure 3.29: First prototype of the exoskeleton

Although there are many improvements to be made before printing the final prototype, the first prototype provides the range of motion necessary to perform all the ADLs defined in section 1.3, as observed in figure A.1 of appendix A.

The exoskeleton was easy to put on by the user, albeit a second person significantly simplifies the process, and is comfortable. However, the exoskeleton is cumbersome because of the fact that, when performing certain movements, the exoskeleton does not stay connected to the body as expected and the telescopic rails of the arm link unlock. Furthermore, various problems occured during and due to the 3D printing process.

As there are still many limitations of the first prototype, due to either design features or to the printing process in itself, the following sections focus on the necessary improvements to implement before printing the final prototype.

3.6.2 Design Aspects to Improve

Arm link

The arm link composed by the telescopic rails does not lock in place when the user performs sharp and abrupt movements. In these situations, the arm link extends its length and it is necessary to untighten the bolt, reposition the outer telescopic rail in its initial placement and tighten the bolt again. This limitation, although not completely impairing the usage of the exoskeleton, would be a great inconvenience for the user and must, therefore, be mitigated.

For this reason, a groove was added to the inner telescopic rail and a tongue to the outer telescopic rail to hold these parts together during the usage of the exoskeleton. A sample of the rails with these new features was 3D printed, to test ergonomics and if the locking mechanism is more reliable. In the preliminary stage of the design, two types of notches were modeled and printed, as presented in figures 3.30 and 3.31.

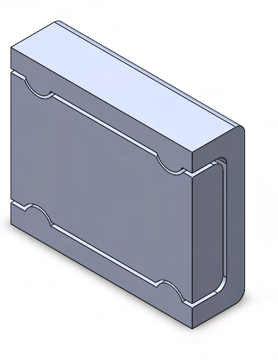

(a) CAD model of the first option of the telescopic rail with grooves

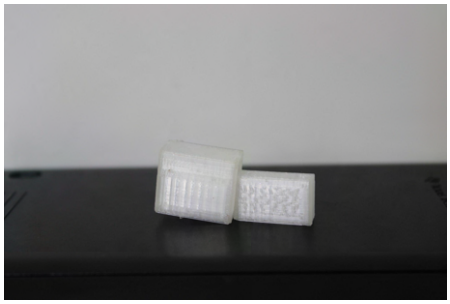

(b) 3D printed sample of the first option

Figure 3.30: First option of the telescopic rail with grooves

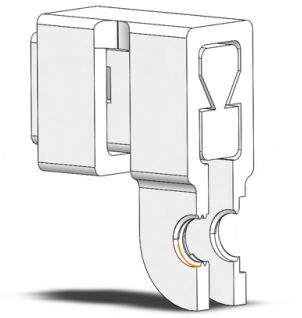

(a) CAD model of the second option of the telescopic rail with grooves

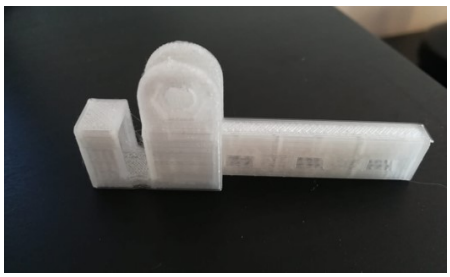

(b) 3D printed sample of the second option

Figure 3.31: Second option of the telescopic rail with grooves

The first option can not be utilized as the two rails do not fit each other. On the other hand, increasing the clearance between the two parts would result in a mechanism that would not lock in place. The second option, although allowing for the parts to lock, increases the difficulty in maneuvering the telescopic rails to obtain the length required. Therefore, the second option was modified, placing the notches closer to the opening of the outer telescopic rail, to facilitate the movement between the two rails while still providing a secure locking mechanism, as pictured in figure 3.32 (a).

It is, however, important to note that for this mechanism to work the part has to be printed with the largest section as the base, as illustrated in figure 3.32 (b), due to the fact that, for the telescopic rails to easily move, the locking feature of the outer bar has to be pressed open by the user. As this creates shear forces acting on the part, if the part is printed with a vertical orientation, it breaks.

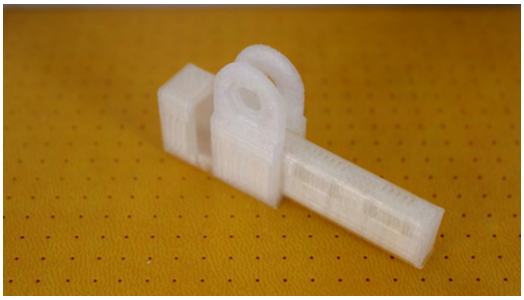

(a) 3D printed sample of the redesigned arm telescopic rail

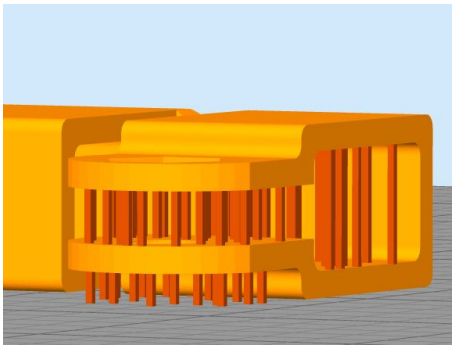

(b) Print orientation of the outer telescopic rail

Figure 3.32: Redesigned telescopic rail with grooves

Connection to the limbs

During the usage of the exoskeleton, it was also noticed that the connection to the user's body was not enough to provide a stable and comfortable experience for the user. It was observed that this problem was predominantly evident in the elbow and shoulder joint, as when extending the arm the exoskeleton would not comply, as noticeable by figure 3.33.

Figure 3.33: Connection of the first prototype to the body of the user

Consequently, it is necessary to add a connection to the body in the elbow link and another in the shoulder link. The forearm link was extended, to permit the positioning of a second strap closer to the elbow joint, without interfering with its range of motion. Additionally, the handle was removed to allow for a strap with a larger width to be placed in its position, also simplifying the part's design and the attachment process.

When it comes to the shoulder joint, a slot was added that permits the addition of another strap that connects this joint to the shoulder of the user. Similarly, the same feature was added to the back link, so that a new connection between this part and the back of the user is added.

With these design modifications, presented in figure 3.34, four TPU straps are necessary to connect the exoskeleton to the user's body. As the build volume of the 3D printer used is not sufficient to print the connection of the upper part of the back link, another strap, for example, a ribbon, can be used. Furthermore, an additional strap is required to join the back link to the hips of the user, similar to the first prototype. Although this strap can also not be 3D printed due to size, a simple belt can be used.

(a) Redesigned forearm link

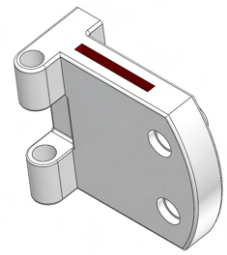

(b) Redesigned shoulder joint connection

(c) Redesigned back link connection

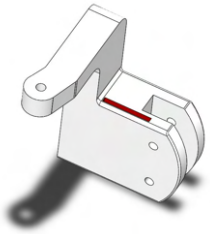

(d) Redesigned elbow link

Figure 3.34: Redesigned connection features to the body of the user

Back link

The mechanism for locking the back joint is not only extremely inconvenient for the user to lock into place, especially without the help of another person, but its holes also significantly decrease the part's resistance to stress. Therefore, the same locking mechanism as the arm link is be applied to the final part.

Wear

Wear is the removal of a material on a surface when friction with another surface occurs, often when two parts are in repeated relative movement to each other. The wear rate of a certain part depends on its geometry and mechanical properties, on the load applied, and on the hardness of the material. There are various wear mechanisms but, for the purpose of the thesis, only three are considered.

Adhesive wear occurs when one part in frictional contact with another suffers plastic deformation and transferring or removal of material from one another ensues. Fretting wear is a type of adhesive wear that takes place when there is repeated and cyclical movement between two parts, causing the removal of material from one or both contact surfaces. Abrasive wear happens when a hard rough surface is in

contact with a softer surface. An article [105] published by R. Aziz, M. I. Ul Haq, and A. Raina, in 2020, where wear tests and subsequent surface analysis are performed on FDM 3D printed PLA samples, with a pin-on-disc tribometer with a steel disc, concluded that the removal of material in the sample occurs due to both adhesion and abrasion. Therefore, it is probable that these wear mechanisms cause wear in the exoskeleton surfaces in contact with steel screws, particularly when there is rotation around these parts.

Various printing parameters and overall conditions have been shown to have an effect on the wear of FDM 3D printed PLA parts. In a 2021 paper [106] where tribological studies of 3D printed PLA parts are performed reported that the wear rate increases proportionally with the layer thickness and the infill density, as the distortion effect dominates the bond effect, and when the infill angle is increased from 45° to 90°. In another similar study [107], it was shown that build orientation also influences the wear resistance of PLA 3D printed parts as horizontally printed parts have a higher wear rate than parts printed vertically or in a 45° orientation. Furthermore, a smooth surface finish of the component significantly reduces the wear suffered, as the contact area is minimized. The influence of these parameters is taken into account in the 3D printing process and in the selection of its parameters, to improve wear resistance whenever possible.

Taking the information provided in the previous paragraphs into account, several design measures can be taken to reduce the wear in the exoskeleton. Firstly, unthreaded screws can be used to reduce the contact area between the PLA and the steel. The clearance between the bolts and the 3D printed parts surface, for static components, should also be reduced to decrease friction between the parts. On the other hand, to reduce the wear between rotating parts and pins, a rubber O-ring can be placed between the top of the pins and the component. If the wear problem persists, a rubber sleeve can also be placed between the body of the screw and the part. However, this final solution was not employed as it hindered the rotation and consequent fluid movement of the exoskeleton.

3.6.3 3D Printing Challenges and Solutions

During the 3D printing process, several challenges arose either due to the process in itself or due to design features.

Dimensional Accuracy

A problem that occurred recurrently during the printing process was that certain parts did not match as expected and as modeled in SolidWorks. This issue ensued even though clearances were set for the necessary parts. Specifically, a transition fit of 0.2 mm was set for parts that were fixed to each other, and a clearance fit of 0.3 mm for parts that would have rotating or translating movements. This problem resulted in many parts having to be reprinted several times, wasting time and material.

To mitigate this problem, a test was performed. Firstly, two thin plates were printed: one with cylinders and one with holes with diameters from 3 mm to 32 mm, as presented in figure 3.35. The diameter of the holes and the cylinders were then measured three separate times using a digital caliper, with a resolution

of 0.05 mm and uncertainty of $\pm$0.05 mm. The dimensions obtained were compared with the dimensions initially modeled.

Figure 3.35: Dimensional test plate with holes (left) and cylinders (right)

Table A.5 in appendix A presents the results obtained of the theoretical diameter defined in SolidWorks, during the design process, and the average value of the diameter measured with the digital caliper.

As the results suggest, the difference between the theoretical diameter and the true diameter is more significant in holes. It is also possible to observe that the error increases proportionally to the diameter, both for the plate with the cylinders and the plate with the holes. Furthermore, it is also notable that the difference between the two diameters can reach values of up to 0.4 mm, which explains why many parts did not match well with others, even with clearances between the two set during the design process. In fact, the true diameter of the cylinders is always larger than the true diameter of a hole with the same theoretical dimensions. To mitigate this problem, the graphs presented in figure 3.36 provide the equation of the linear regression between the theoretical and the true diameter that is used to estimate the dimension of the diameter to establish in the CAD model so that the intended dimension can be obtained.

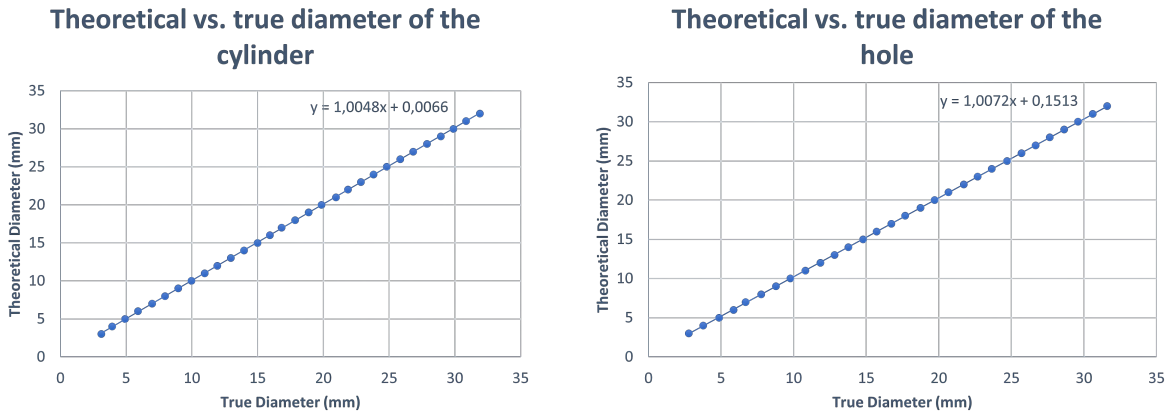

Figure 3.36: Graphs of the theoretical diameter in function of the true diameter, for both plates

Clearance Fit and Transition Fit

Although in the previous section the problem of dimensional accuracy was addressed, it is still not clear what clearance fit and transition fit should be established. Therefore, the cylinders photographed

in figure 3.37 were printed and the plate with holes was re-purposed to serve as the part where the cylinders are fitted into.

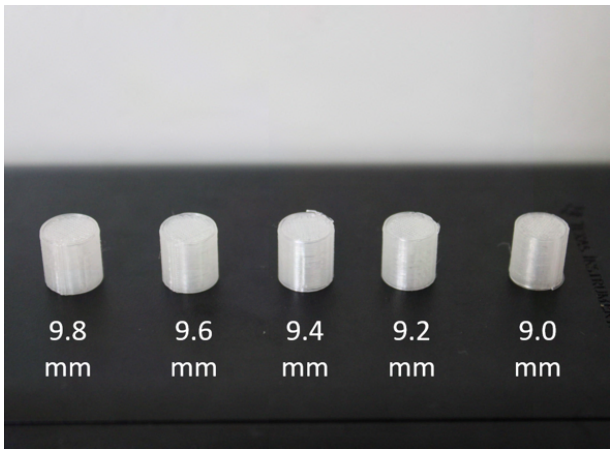

Figure 3.37: 3D printed cylinders

The cylinders were then placed in the plate's 10 mm hole, as photographed in figure 3.38. As expected, the 9.8 mm cylinder did not match, since, according to the previous section, the hole actually measures 9.78 and the cylinder has a 9.74 mm diameter, creating a clearance between the two parts of only 0.02 mm. The 9.6 mm cylinder has an interference fit with the hole. On the other hand, the 9.4 mm cylinder can fit into the hole easily, providing a transition fit. The 9.2 mm cylinder allows for rotation and translation movements through the hole and, finally, the 9.0 mm cylinder can be loosely placed in the hole.

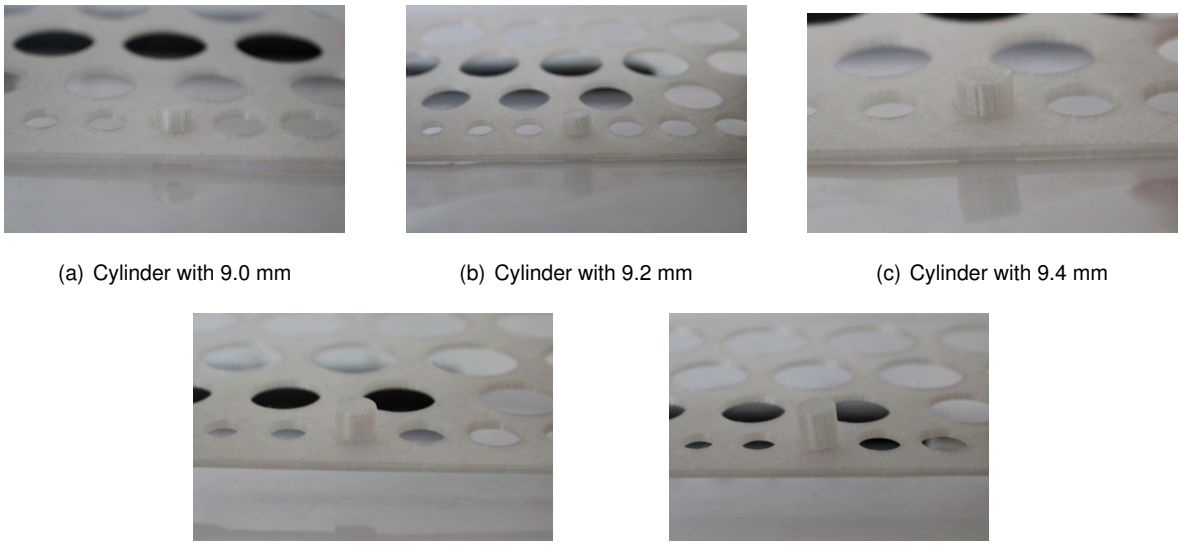

(a) Cylinder with 9.0 mm (b) Cylinder with 9.2 mm (c) Cylinder with 9.4 mm

(d) Cylinder with 9.6 mm (e) Cylinder with 9.8 mm

Figure 3.38: Cylinders with various diameters placed into a 10 mm hole

This test provides multiple conclusions regarding the clearances that will be used in the design of the final prototype while taking into account that the dimensions established in the CAD model will be the ones obtained through the equations presented in the last section. For parts that need a transition fit,

a distance of 0.2 mm should be provided, while parts that rotate or translate through each other should have a clearance fit of 0.3 mm.

3D printing with TPU

As noticeable in figure A.1 presented in appendix A, the TPU straps mentioned in section 3.4.2 were not actually used due to the fact that the 3D printed straps failed during their first usage, in the section indicated by the blue circle in figure 3.39. It can also be observed that the surface finish and the overall quality can be improved. Furthermore, during the printing process, it was possible to hear a tingling sound, which indicates that, during the extrusion of the TPU filament, water was being evaporated. This means that, although the TPU filament was only exposed to the environment for approximately 3 hours, the high relative humidity of the air was enough to infiltrate the filament.

For this reason, to dry the filament before printing, several actions can be taken. The TPU filament can be placed in a greenhouse the day before usage 25 °C below its glass-transition temperature. However, as a greenhouse was not available and the manufacturing of the exoskeleton should be available to anyone with access to a 3D printer, this option was discarded. Alternatively, the TPU filament can be placed in an environment with a dehumidifier to prevent the absorption of humidity but, for the same reason as the first solution, this option was discarded. Instead, the TPU filament was placed in the oven at 70 °C for one hour. This solution is available for most people and takes the least time to implement, providing good results as illustrated in figure 3.39 (b).

(a) 3D printed TPU strap

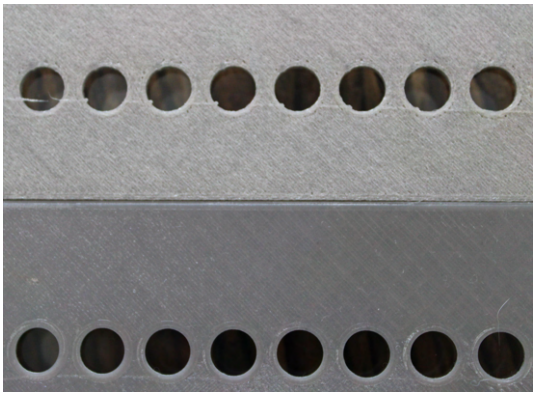

(b) Comparison between the first TPU print (top), with humidity, and the final TPU strap (bottom), previously dried

Figure 3.39: TPU straps

With the design process completed, it is now possible to analyze the structure of the prototype in the next chapter.

Chapter 4

Engineering Calculation Notes

In the present chapter, the structural analysis of the exoskeleton is performed. For this purpose, after the safety factor is determined, a kinematic model of the exoskeleton is established that determines the maximum torsional moment in each joint, the starting point to proceed with the analytical calculations. After the safety of each part is assessed, the design is modified when it does not comply with the safety criteria.

4.1 Safety Factor

In the present case, the safety factor has to account for multiple factors such as the risk of injury for the user, financial loss of the manufacturer, uncertainty regarding 3D printed parts, and others. The Pugsley method is employed to determine the safety coefficient, using equation 4.1.

$$n_s = n_{sx} \times n_{sy} \tag{4.1}$$

The term n_{sx} accounts for three factors that influence the reliability of the part. These factors are graded on a scale that measures their accordance to reality: *vg* $\equiv$ *very good*; *g* $\equiv$ *good* ; *f* $\equiv$ *fair*; or *p* $\equiv$ *poor*:

- **A**: Quality of materials, workmanship, maintenance, and inspection - **good**

  The exoskeleton is fabricated using good quality PLA filament and optimal 3D printing properties but there is no further maintenance of the part. However, depending on the entity that is responsible for printing the exoskeleton and the 3D printer used, the properties and quality of the parts can change.

- **B**: Control over applied load - **fair**

  Although the maximum permissible load is indicated to the users, there is no guarantee that it will not be surpassed. Moreover, situations that create a shear force applied to the exoskeleton, such as accidentally hitting a door with the arm, are not accounted for in these calculations.

- **C**: Accuracy of stress analysis, experimental data, or experience with similar designs or devices - **fair**

  As it will be explained further in sections 4.4 and 5.1, there are several limitations in both the analytical and finite-element analysis of 3D printed parts. These limitations hamper the accuracy of the stress analysis. On the other hand, the experimental data available for similar parts is scarce and, consequently, the material properties used do not fully correspond to reality. Furthermore, 3D printed parts can have a decreased resistance to stress depending on the part orientation and the direction of applied force.

According to the Pugsley's table, it is determined that $n_{sx} = 2.3$.

The term n_{sy} accounts for two other factors that measure the financial and personal impact of the failure of the exoskeleton. The impact is graded through the following scale: *vs* $\equiv$ *very serious*; *s* $\equiv$ *serious*; *ns* $\equiv$ *not serious*. The value of the term n_{sy} is, then, determined to be 1.

- **D**: Danger to personnel - **Not serious**

  If the exoskeleton fails, the user will not suffer from any physical damage as their arm will only return to its natural position. Therefore, the risk of personal harm is considered not serious.

- **E**: Economic impact - **Not serious**

  When a part eventually fails another one can be easily and inexpensively printed, minimizing the economic impact for both the user and the manufacturer.

Using these values of n_{sx} and n_{sy}, equation 4.1 can be solved and the value of the safety coefficient is determined to be $n_s = 2.3$.

4.2 Kinematic Model

To proceed with the analytical stress analysis it is necessary to find a kinematic model that represents the movement of the exoskeleton when in use. This kinematic model allows the determination of the torque being supported by each joint in every stage of the movement and, therefore, serves as a starting point for the stress analysis.

The exoskeleton proposed has five DOFs, considering that the rotation of the shoulder is not constrained by a solid vest, as is the case in the WREX exoskeleton. Gravity is to be completely compensated by the elastics placed in the joints. The gravity compensation provided is a function of the joint angles so that the muscular effort necessary is minimized to perform a certain task. Taking this into account, in the following section, the Denavit-Hartenberg convection [108] is used to represent the position of the exoskeleton.

4.2.1 Denavit–Hartenberg Convention

An overview of the Denavit-Hartenberg convection and its constraints is provided in appendix B. Applying the rules of this notation, it is possible to draw the simplified kinematic model of the exoskeleton,

represented in figure 4.1, and to place the coordinate frame following the assumptions mentioned in appendix B and schematized in figure B.1. Therefore, the coordinate frame is placed, as illustrated in figure 4.2.

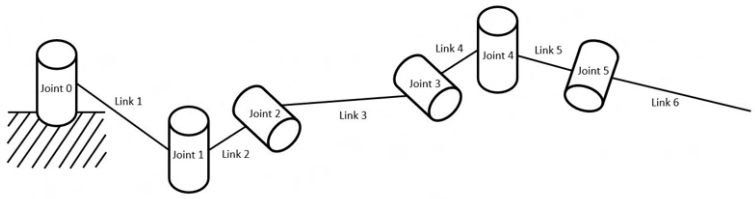

Figure 4.1: Simplified kinematic model of the exoskeleton

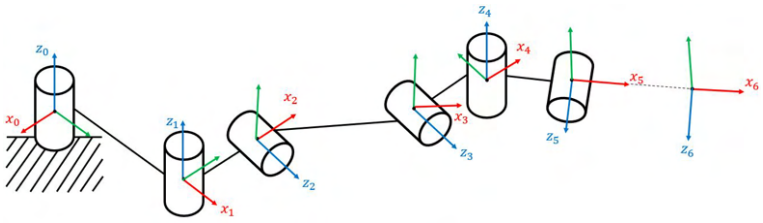

Figure 4.2: Kinematic model of the exoskeleton with respective axis frames placed according to the Denavit-Hartenberg convention

It is considered that $\theta_4 = -\theta_3$ since, due to the geometry of the exoskeleton, joints 2 and 3 remain parallel at all times. According to the kinematic diagrams, it is possible to reach the Denavit-Hartenberg parameters, represented in table 4.1. The schematic representation of these parameters is presented in figure B.1 of appendix B. Although this table has six rows, indicating a priori that there are six DOFs, as $\theta_4 = -\theta_3$, there are only five DOFs.

Table 4.1: Denavit-Hartenberg parameter table

Joint j	θ_j (°)	α_j (°)	d_j (cm)	a_j (cm)
1	θ_1	0	0	8
2	θ_2	90	0	1.9
3	θ_3	0	0	25
4	- θ_3	-90	0	8.5
5	θ_5	90	0	9.5
6	θ_6	0	0	5.5

As the exoskeleton is only attached to the limb of the user in the forearm and as the elastics that support the arm are not considered at this stage, the kinematic model only considers that there are applied loads in link 6. The weight of the upper part of the arm is considered to be supported by the shoulder of the user. Consequently, this load comprises the weight of the forearm and the hand of an adult, 1.76 kg according to [109], and a small object weighing 0.5 kg, that the user is holding. Therefore, the value of P_{load} is 22.6 N. As the momentum caused by a load is higher the larger the distance between

the point of application and the center of mass of the link, the case where an adult is wearing the exoskeleton is considered. Consequently, the distance between the point of application of the load and the center of mass of the link is 313 mm, as represented in figure 4.3. It is also considered that the exoskeleton is fully extended, to maximize the torque in each joint.

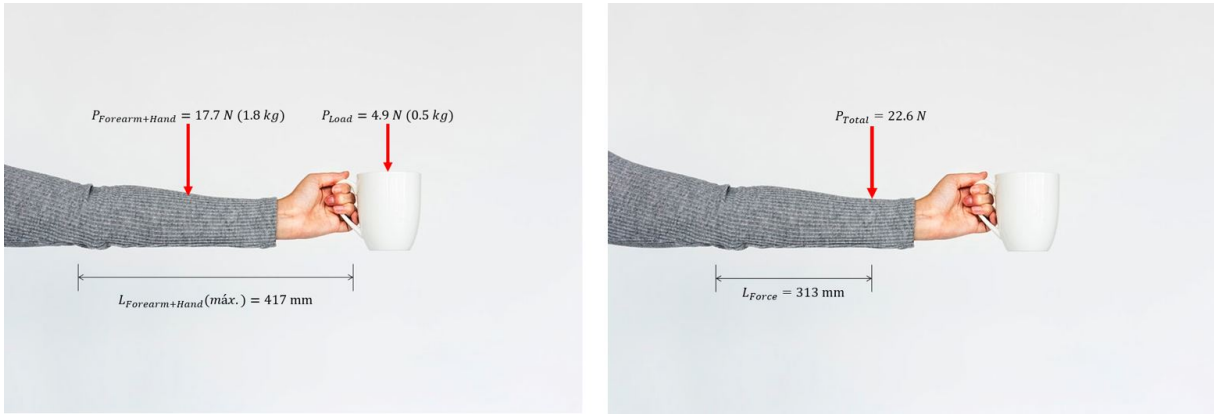

Figure 4.3: Loads applied in link 6 of the exoskeleton

4.3 Dynamic Model

The dynamic model of the exoskeleton can be expressed according to the Euler-Lagrangian formulation, defined in equation 4.2.

$$M(q)\ddot{q} + C(q,\dot{q}) + G(q) + f(\dot{q}) + D(\dot{q}) = \tau - J_e^T F_e \tag{4.2}$$

Where:

- $q = [\theta_1, \theta_2, \theta_3, \theta_5, \theta_6]^T$ is the vector of the degrees of freedom;
- $M(q)$ is the inertia matrix;
- $C(q,\dot{q})$ is the Coriolis and centrifugal vector;
- $G(q)$ is the gravitational vector;
- $f(\dot{q})$ is friction forces vector;
- $D(\dot{q})$ is the damping vector;
- τ is the vector of applied torques at the actuated joints, obtained from the Denavit–Hartenberg Convention;
- J_e^T is the transposed extended Jacobian matrix;
- F_e is the vector of external forces applied by the human and/or external load.

As this model has the sole objective to find the loads that are applied in the exoskeleton for a given position, static conditions are considered and, therefore, $\dot{q}$ and $\ddot{q}$ are zero. Furthermore, as all the forces

considered are caused by weights that are accounted for in the $G(q)$ vector, the vector of external forces is also null. Therefore, equation 4.2 can be simplified to equation 4.3.

$$G(q) = \tau \tag{4.3}$$

The previous equation is useful to obtain the torque that each joint has to apply, τ, so that, in static conditions, for a given exoskeleton configuration, q, to counter the force of gravity. This equation perfectly captures the objective of the exoskeleton, which is to create a zero-gravity sensation for the user.

4.3.1 Results

To encounter the maximum torque at each joint and the position in which it occurs, MATLAB's Symbolic Math Toolbox was used. This toolbox automatically generates a function that outputs the maximum torsional moment in joints 2, 3, and 5, as all other joints are only subjected to bending moments, and the position in which it occurs. The upper and lower limits of the angle of each joint are set according to the anatomical range of motion represented in figure 2.9. The results obtained are represented in table 4.2.

Table 4.2: Maximum torsional moment in each joint and the position at which it occurs

Joint j	Maximum torsional moment (N.m)	θ_3 °	θ_5 °	θ_6 °
2	16.50	0	0	0
3	10.81	-	0	0
5	6.75	-	-	0

The torsional moments obtained for each joint are used in the next section to compute the load that each part is carrying.

4.4 Analytical Calculations

For the analytical calculations, the properties of the PLA filament of table 3.2 are considered. However, as mentioned in section 3.1.1, in FDM 3D printing, the parts are composed of an outer shell and an infill. As indicated in table A.4 in appendix A, there are two outline shells and, as the nozzle diameter is 0.4 mm, the wall thickness of the 3D printed parts is $t = 0.8mm$. For this reason, and to consider the worst-case scenario, formulas for thin-walled sections are applied.

However, in pure uniaxial tension, or compression, the formula considered is simply $\sigma_F = \frac{F}{A}$, as the material properties considered concern a tensile test performed on a specimen with a 25% infill density and a uniaxial compression test for a standard infill specimen. The remaining formulas used are directly obtained or deducted from Shigley's "Mechanical Engineering Design" [110]. For closed thin-walled tubes, the shear stresses that develop throughout the cross-section due to a torsional moment (T), τ_T , are calculated using the following equation, where t is the wall thickness and A_m is the area enclosed by the section's median line.

$$\tau_T = \frac{T}{2 \times t \times A_m} \tag{4.4}$$

For the transverse shear stress and the normal bending stress, the general formulas are applicable to both full and thin-walled sections. The beam represented in figure 4.4 and its coordinate axis are used as a reference for the positioning of the axis throughout the present stress analysis.

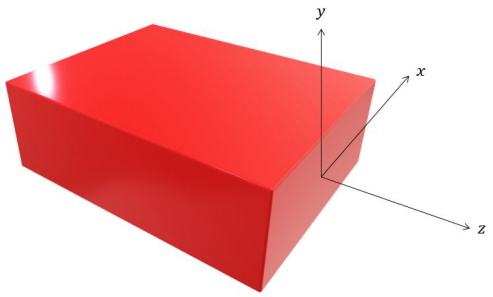

Figure 4.4: Basic beam and representation of the positioning of the coordinate axis

The transverse shear stress, caused by the shear force V, can be obtained directly through equation 4.5, in the section that has a distance of y_1 in relation to the neutral axis,

$$\tau_V = \frac{V \times Q}{I \times b} \tag{4.5}$$

where b is the width of the section at $y = y_1$, I is the second moment of area, and Q is the first moment of the area, both in respect to the neutral axis. Q can be computed through equation 4.6.

$$Q = \int_{y_1}^{c} y \, dA = \overline{y}' A' \tag{4.6}$$

In the previous equation, c is the distance between the neutral axis and the edge of the section, A' is the area of the section between y_1 and c, y' is the distance in the y-direction from the neutral plane to the centroid of the area A'. These variables are schematized in figure 4.5.

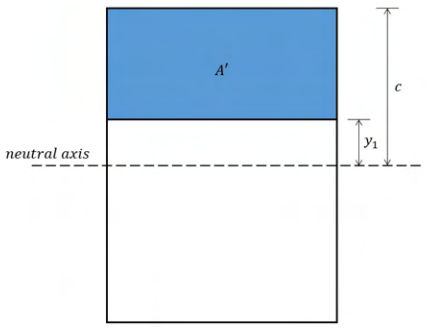

Figure 4.5: Schematic representation of the variables necessary to compute the first moment of area

To obtain the maximum transverse shear stress, y_1 is considered to be the vertical coordinate of the section in which the stress is maximum, which usually occurs at $y_1 = 0$, where the term $\overline{y}'A'$ reaches its maximum value.

When it comes to the normal stresses for beams in bending, the stress varies linearly with the distance from the neutral axis. The maximum stress, therefore, occurs at the maximum distance from the neutral axis. For a bending moment around the x-axis, M_x, the y-axis, M_y, or both, equation 4.7 can be used to compute the maximum normal stress, σ_z, the load generates

$$\sigma_z = +\frac{M_x \times y}{I_x} - \frac{M_y \times x}{I_y} \tag{4.7}$$

where I_x is the second moment of area about the x-axis and I_y is the second moment of area about the y-axis.

With the general formulas obtained, it is possible to derive the particular equations applicable for the two types of thin-walled cross-sections encountered in the exoskeleton: circular and rectangular, represented in figures 4.6 and 4.7, respectively.

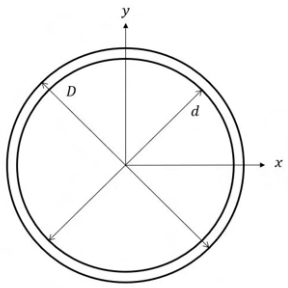

$$\tau_T = \frac{T}{(D-d) \times (\frac{D/2+d/2}{2})^2 \times \pi} \tag{4.8}$$

$$\tau_V = \frac{2 \times V}{((D/2)^2 - (d/2)^2) \times \pi} \tag{4.9}$$

$$\sigma_{Mx,y} = \frac{M_{x,y} \times \frac{D}{2}}{I_{x,y}} \tag{4.10}$$

$$I_x = I_y = \frac{\pi}{64}(D^4 - d^4) \tag{4.11}$$

Figure 4.6: Formulas to compute the stresses in a circular thin-walled part, [110]

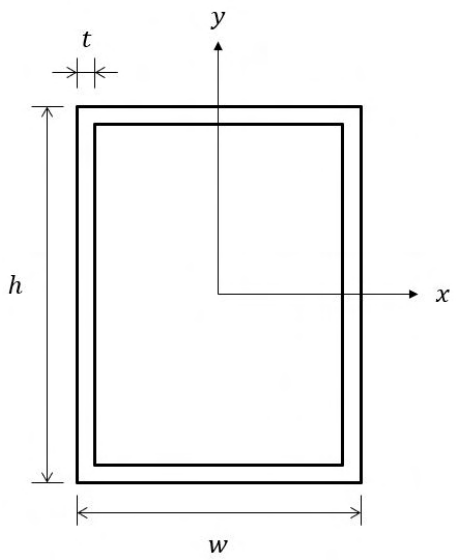

$$\tau_T = \frac{T}{2 \times t \times (w-t)(h-t)} \tag{4.12}$$

$$\tau_{Vx} = \frac{V_x \times Q_y}{2 \times t \times I_y} \tag{4.13}$$

$$\tau_{Vy} = \frac{V_y \times Q_x}{2 \times t \times I_x} \tag{4.14}$$

$$\sigma_{Mx} = \frac{M_x \times \frac{h}{2}}{I_x} \tag{4.15}$$

$$\sigma_{My} = \frac{M_y \times \frac{w}{2}}{I_y} \tag{4.16}$$

$$I_x = \frac{1}{12}(h^3 w - (h-2t)^3(w-2t)) \tag{4.17}$$

$$Q_x = w\frac{h}{2}\frac{h}{4} - (\frac{h}{2} - t)(w-2t)(\frac{\frac{h}{2}-t}{2}) \tag{4.18}$$

$$I_y = \frac{1}{12}(w^3 h - (w-2t)^3(h-2t)) \tag{4.19}$$

$$Q_y = h\frac{w}{2}\frac{w}{4} - (\frac{w}{2} - t)(h-2t)(\frac{\frac{w}{2}-t}{2}) \tag{4.20}$$

Figure 4.7: Formulas to compute the stresses in a rectangular thin-walled part, [110]

Since the PLA filament is brittle, as the fracture strain is less than five percent, i.e, $\epsilon_f < 5\%$, the effect of stress concentrations near discontinuities of the part must be considered in static loading conditions. Therefore, before comparing the maximum stress with the strength of the material, the nominal stress must be multiplied by the geometric stress concentration factor, K_t. The stress concentration factors are obtained through Shigley's "Mechanical Engineering Design" [110] and through "Peterson's Stress Concentration Factors" [111] books.

The maximum shear and normal stresses applied in a component depend on the transverse section analyzed. Consider, as an example, a thin-walled rectangular section represented in figure 4.8 subjected to various stresses.

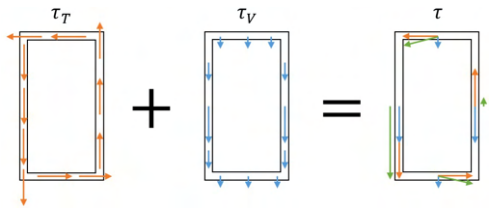

(a) Normal stresses applied in a thin-walled rectangular cross section

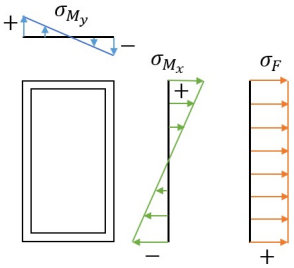

(b) Shear stresses applied in a thin-walled rectangular cross section

Figure 4.8: Schematic of stresses applied in a thin-walled rectangular cross-section

It is evident in figure 4.8 (a) that the maximum shear stresses occur on the mid-section of the left side of the cross-section. In this case, to obtain the maximum shear stress, it would only be necessary to sum the torsional stress and the transverse stress. Additionally, if there were shear forces applied in perpendicular directions, the maximum transverse stress would be given by $\tau_{Vmax} = \sqrt{\tau_{Vx}^2 + \tau_{Vz}^2}$. On the other hand, through figure 4.8 (b), the maximum normal stress occurs in the top left corner of the section and is given by $\sigma_{Zmax} = \sigma_F + \sigma_{Mx} + \sigma_{My}$. However, if the part's ultimate compressive strength is lower than the ultimate tensile strength, as is the case with 3D printed PLA, it is necessary to consider the maximum compressive stress $\sigma_{Zmax_c} = -\sigma_F + \sigma_{Mx} + \sigma_{My}$. Although this stress is lower, since the part is weaker in compression, the right bottom corner of the rectangle might be the critical section. Whilst the previous schematic serves only as an example, the principles mentioned are applied to determine the maximum stresses in the components of the exoskeleton.

After obtaining the maximum shear and normal stresses the part is under, a failure theory must be selected to assess the structural integrity of the part being studied. As brittle materials do not display a yield strength, the ultimate tensile and compressive strengths are used to characterize the mechanical behavior of the material. To take a conservative approach, the Brittle Coloumb-Mohr (BCM) theory, written in equation 4.21 is employed.

$$\begin{aligned} \sigma_A &= \tfrac{S_{ut}}{n}, & \sigma_A \geq \sigma_B \geq 0 \\ \tfrac{\sigma_A}{S_{ut}} - \tfrac{\sigma_B}{S_{uc}} &= \tfrac{1}{n}, & \sigma_A \geq 0 \geq \sigma_B \\ \sigma_B &= -\tfrac{S_{uc}}{n}, & 0 \geq \sigma_A \geq \sigma_B \end{aligned} \tag{4.21}$$

The principal stresses σ_A and σ_B are obtained through equation 4.22.

$$\sigma_A, \sigma_B = \frac{\sigma_z + \sigma_y}{2} \pm \sqrt{(\frac{\sigma_z - \sigma_y}{2})^2 + \tau_{zy}^2} \tag{4.22}$$

With all the equations necessary obtained, the next section focuses on assessing the safety of the critical parts of the exoskeleton and, when necessary, redesigning certain features.

4.4.1 Forearm Link

To calculate the load that the elastic band is exerting on the forearm link, the basic formula of the moment, $M = F \times b$ is used. Since the maximum torsional moment of the elbow joint has already been computed and is presented in table 4.2, and the arm of the moment can be obtained through the CAD model, the maximum force that the elastic performs can be easily calculated. Therefore, $F = \frac{6.75}{0.0512} = 131.84$ N.

To calculate the stresses exerted in the forearm link, the part is considered to be a simple parallelepiped, with a hole where the part is connected to the elbow joint and a cylinder that secures the elastic. In figure 4.9, the static load case of the simplified forearm link is represented, including the force and the moment that P_{Total}, defined in figure 4.3 in page 54, creates. The free-body diagrams of the forearm link are represented in figure 4.10.

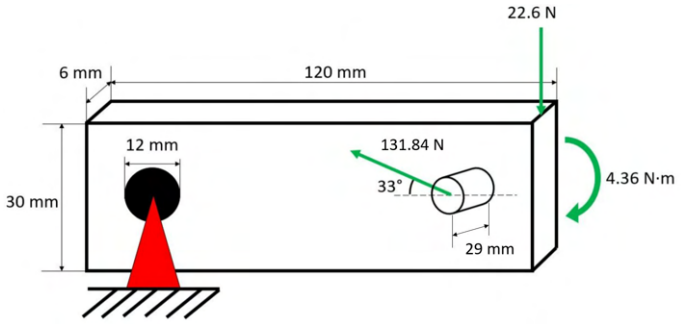

Figure 4.9: Schematized forearm link and loads

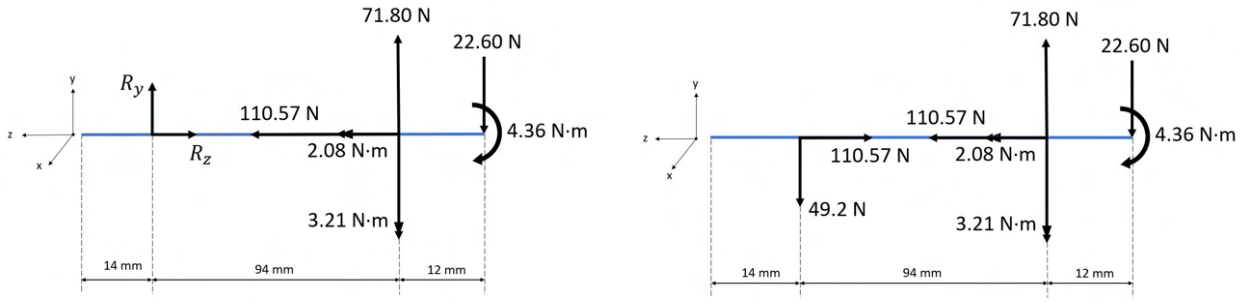

Figure 4.10: Free-body diagram of the forearm link

Considering the stress concentration factors represented in figure 4.11, the stresses can be computed.

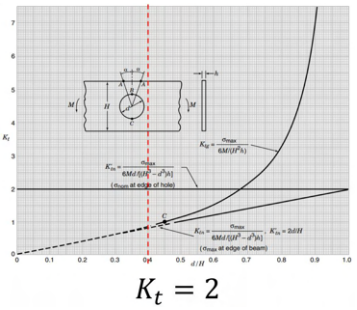

(a) Chart of the theoretical stress concentration factor for a bar in in-plane bending of a thin beam with a circular hole [111]

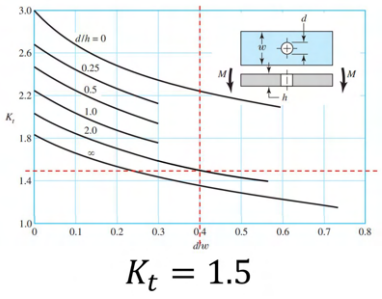

(b) Chart of the theoretical stress concentration factor for a rectangular bar with a transverse hole in bending [110]

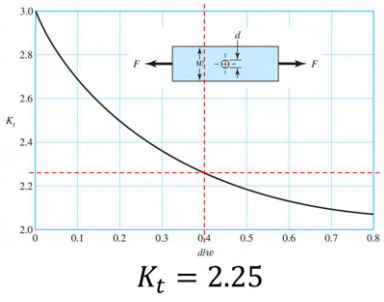

(c) Chart of the theoretical stress concentration factor for a bar in tension or simple compression with a transverse hole [110]

Figure 4.11: Stress concentration factors for the forearm link

Initially, a safety factor of 0.5 was obtained and, therefore, some modifications must be done to the part. Therefore, the width of the part is increased to $w = 22\,mm$ and the number of shell outlines is increased to eight so that the wall thickness increases to $t = 3.2\,mm$. This value of the wall thickness is used for the remainder of the parts analyzed. As an increase in wall thickness translate in an increase in ultimate tensile and compressive strength [112] and as the mechanical properties considered concern a specimen with a 1.2 mm wall thickness, it is expected that the real mechanical properties of the 3D printed parts are better than the ones indicated in table 3.2. However, to take a conservative approach, these properties are still considered.

The calculation of the maximum stresses with the new configuration according to 4.7 is presented in figure 4.12, along with the effort diagram of the part, following the convention indicated in the figure.

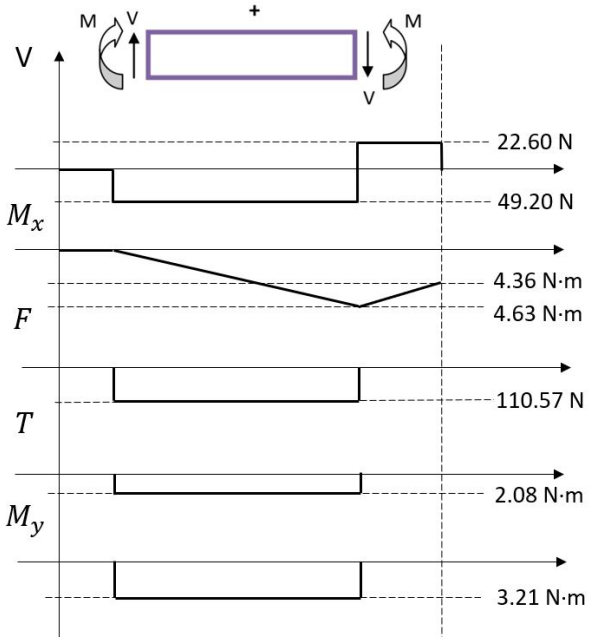

$$I_x = 32.41 \times 10^{-9}\, m^4$$

$$I_y = 19.15 \times 10^{-9}\, m^4$$

$$Q_x = 1.39 \times 10^{-6}\, m^3$$

$$\tau_T = \frac{2.08}{2\times 0.0032\times(0.022-0.0032)(0.030-0.0032)} = 0.64\,\text{MPa}$$

$$\tau_{Vy} = \frac{49.20\times 1.39\times 10^{-6}}{2\times 0.0032\times 32.41\times 10^{-9}} = 0.33\,\text{MPa}$$

$$\sigma_{Mx} = 2\frac{4.63\times\frac{0.030}{2}}{32.41\times 10^{-9}} = 4.28\,\text{MPa}$$

$$\sigma_{My} = 1.5\frac{3.21\times\frac{0.022}{2}}{19.15\times 10^{-9}} = 2.76\,\text{MPa}$$

$$\sigma_F = 2.25\frac{110.57}{0.03\times 0.022} = 0.38\,\text{MPa}$$

$$\sigma_z = -\sigma_F \pm (\sigma_{Mx} + \sigma_{My}) = 6.66 \text{ or } -7.42\,\text{MPa}$$

$$\tau_{zy} = \tau_T + \tau_V = 0.97\,\text{MPa}$$

$$1/n = \frac{0.12}{29} - \frac{-7.54}{17.9} \longrightarrow \textbf{n =2.35}$$

Figure 4.12: Calculation of the stresses exerted in the forearm link and the safety coefficient

With the changes mentioned previously, the stresses decrease and the safety coefficient rises to $n = 2.35$, which is in accordance with the safety factor established previously.

4.4.2 Forearm Elastic Support

In the forearm link, the elastic support feature carries a load of 131.84 N presented in figure 4.13 along with the subsequent stress and safety factor calculations, according to figure 4.6 and equations 4.21 and 4.22. The failure of the part occurs in the section represented in red, as it is where the loads reach their maximum value.

To obtain the stress concentration factor, the chart of figure 4.14 is used. Although the situation the chart refers to does not completely correspond to the current situation, it is still used considering that the larger diameter, $D = 28\,mm$, corresponds to the larger diameter of the red surface. The stress concentration factor obtained must be multiplied by σ_{My}.

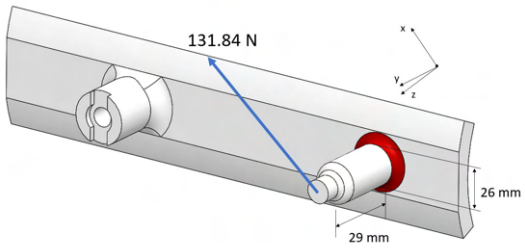

$$I_x = I_y = \frac{\pi}{64}(0.026^4 - (0.020)^4) = 14.58 \times 10^{-9}\, m^4$$
$$\tau_{V_x} = \frac{2 \times 131.84}{((0.026/2)^2 - (0.020/2)^2) \times \pi} = 1.22\,\text{MPa}$$
$$\sigma_{My} = 1.4 \times \frac{131.84 \times 0.029 \times \frac{0.026}{2}}{14.58 \times 10^{-9}} = 4.77\,\text{MPa}$$

$$\sigma_A = 0.29, \sigma_B = -5.06\,\text{MPa}$$
$$1/n = -\frac{-5.06}{17.9} + \frac{0.29}{29} \longrightarrow n = \mathbf{3.42}$$

Figure 4.13: Calculation of the stresses exerted in the forearm elastic support feature and the safety coefficient

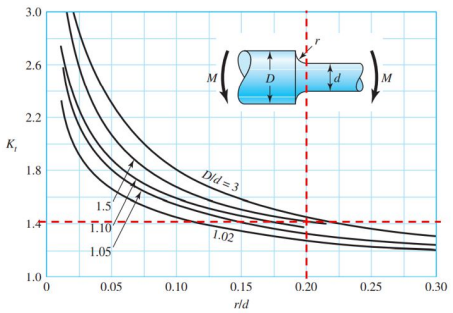

$$K_t = 1.4$$

Figure 4.14: Chart of the theoretical stress concentration factor for a shoulder fillet in bar of circular cross-section in bending [110]

It is, however, important to note that as the forearm link is printed horizontally and due to the anisotropic nature of 3D printed parts, the elastic support feature, when subjected to shear forces perpendicular to the layer orientation, has a lower ultimate tensile strength than the one considered. Consequently, if the stress-strain curve of the material is considered to be similar to the curve obtained in a tensile test for a sample printed upright, as represented in figure 3.6, the ultimate tensile strength significantly decreases. Therefore, although a safety coefficient of $n = 3.42$ may seem excessive, this coefficient takes into account that the mechanical properties of this link are worse than expected.

4.4.3 Arm Link

To understand the influence that the elastic is performing on the arm link, it is first necessary to study the elbow link where the elastic support is located and the load the elastic band exerts on it. The elbow link is subject to the force P_{Total} mentioned previously, which translates into the load represented in figure 4.15 (a). The calculations regarding this figure and section of the arm link are presented in appendix B.

It is considered that the two beams that compose the arm link are purely in tension or compression. Taking this assumption into account, the load case of the elbow link is represented in figure 4.15 (b). As a state of equilibrium between all loads must be reached, the unknown value of the forces F_1, F_2, and F_3 can be determined. Applying the static balance equations, the system of equations 4.4.3 can be solved.

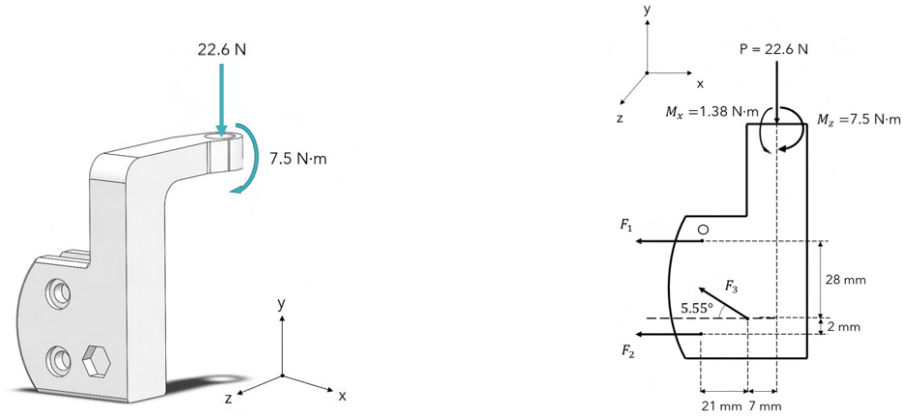

(a) Loads applied in the elbow link

(b) Load case of the elbow link

Figure 4.15: Schematic of the loads applied in the elbow link

$$\begin{cases} \sum F_x = 0 \\ \sum F_y = 0 \\ \sum M_{zO} = 0 \end{cases} = \begin{cases} -F_1 - F_2 - F_3 \times cos(5.55) = 0 \\ -22.6 + F_3 \times sin(5.55) = 0 \\ 21 \times F_3 \times sin(5.55) - 28 \times cos(5.55) \times F_3 - 30 \times F_2 - 22.6 \times 28 - 7500 = 0 \end{cases} \leftrightarrow$$

$$\leftrightarrow \begin{bmatrix} -1 & -1 & -cos(5.55) \\ 0 & 0 & sin(5.55) \\ 0 & -30 & 21 \times sin(5.55) - 28 \times cos(5.55) \end{bmatrix} \begin{bmatrix} F_1 \\ F_2 \\ F_3 \end{bmatrix} = \begin{bmatrix} 0 \\ 22.6 \\ 22.6 \times 28 + 7500 \end{bmatrix} \leftrightarrow \begin{cases} F_1 = 239.77N \\ F_2 = -472.35N \\ F_3 = 233.68N \end{cases} \tag{4.23}$$

It is now evident that the upper beam member is in tension and the lower beam in compression. Consequently, it is only necessary to calculate the stresses exerted in the lower telescopic rail, as the value of F_2 is larger and as the material's strength is lower in compression. Calculating the stresses in each telescopic rail, inner and outer, while assuming that the beams are perfectly connected and behave as a single part, can be easily done through equation $\sigma = F/A$ and by multiplying it with the stress concentration factor obtained through figure 4.16. These calculations are represented in figure 4.17.

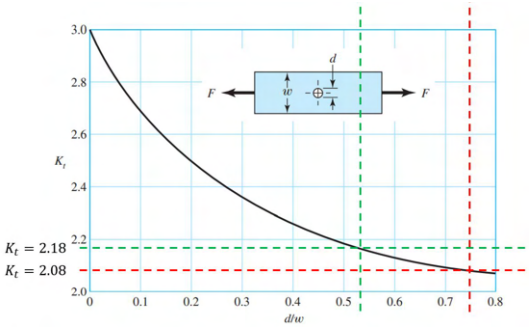

Figure 4.16: Chart of the theoretical stress concentration factor for a bar in tension or simple compression with a transverse hole [110]

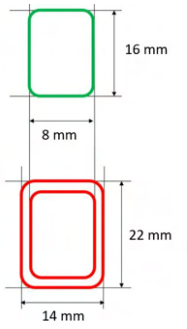

$$\sigma_{Finner} = K_t \frac{F}{A} = 2.08 \frac{472.35}{8 \times 16} = 7.67\,\text{MPa} \longrightarrow n = \frac{17.9}{7.67} = \mathbf{2.33}$$
$$\sigma_{Fouter} = K_t \frac{F}{A} = 2.18 \frac{472.35}{22 \times 14 - 8 \times 16} = 5.72\,\text{MPa} \longrightarrow n = \frac{17.9}{5.72} = 3.13$$

Figure 4.17: Calculation of the stresses exerted in lower telescopic rails

As the lower safety coefficient is lower than $n_s = 2.3$, the parts satisfy the safety criteria.

4.4.4 Elbow link elastic support

It is also necessary to study the elastic support of the elbow joint. Unlike the elastic support of the forearm link, this feature fits into the joint and supports the load F_3 determined previously through the system of equations 4.24, as represented in figure 4.18. As the safety coefficient initially obtained is extremely low, with a value of $n = 0.6$, significant modifications must be done to ensure that the part satisfies the safety criteria. Firstly, this part will be printed with an infill density of 100%, so that the part is solid. Therefore, according to [85] and [92], the same sources used to determine PLA properties with a 25% infill density, the ultimate tensile strength is equal to 40 MPa and the ultimate compressive strength rises to 93.8 MPa. With the part being now solid, it is necessary to apply formulas for a regular circular cross-section, obtained through [110] and indicated in figure 4.18. Furthermore, the diameter of the section was increased to $d = 13mm$. The stress calculations performed for this new case are presented in figure 4.18 using the stress concentration determined by figure 4.19, and it is determined that the part complies with the safety criteria.

Due to the anisotropic properties of 3D printed parts and as the elastic support is subjected to shear stresses in the direction that the part is weaker, this component can not be printed vertically on its largest flat surface. Consequently, the part must be printed horizontally, with the aid of supports.

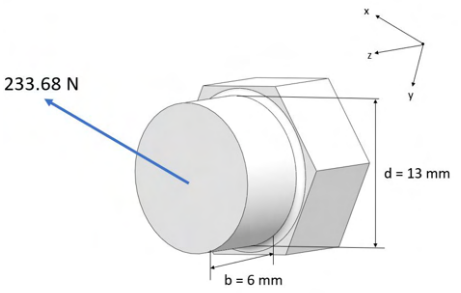

$$I_x = I_y = \frac{\pi \times d^4}{64} = 1.40 \times 10^{-9}\, m^4$$
$$\sigma_{My} = 1.3 \times \frac{233.68 \times 0.006 \times \frac{0.013}{2}}{1.40 \times 10^{-9}} = 8.46\,\text{MPa}$$
$$\tau_{Vx} = \frac{4V}{3A} = \frac{4 \times 233.68}{3 \times \pi (0.013/2)^2} = 2.35\,\text{MPa}$$

$$\sigma_A = 9.07\,\text{MPa}, \sigma_B = -0.61\,\text{MPa}$$
$$\frac{9.07}{40} - \frac{-0.61}{93.8} = \frac{1}{n} \longrightarrow \textbf{n = 4.27}$$

Figure 4.18: Calculations of the stresses applied in the elastic support feature in the elbow link

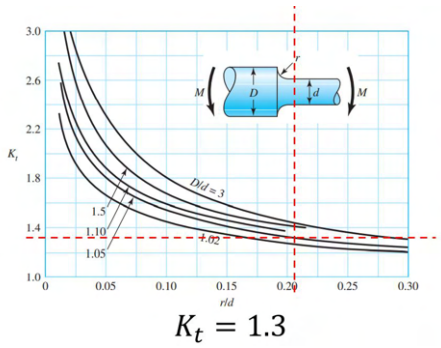

Figure 4.19: Chart of the theoretical stress concentration factor for a shoulder fillet in bar of circular cross-section in bending [110]

4.4.5 Back pin

As steel bolts with the dimensions necessary were unavailable, the back pins were 3D printed. Analyzing the pin positioned in the shoulder joint, it is assumed that the loads are transferred to the pin as represented in figure 4.20.

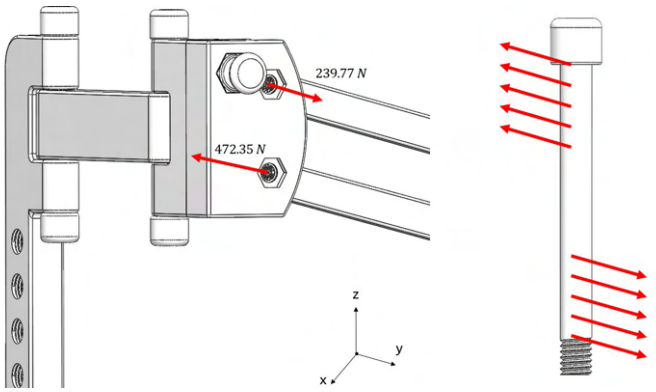

Figure 4.20: Loads applied to the pin

Considering that the pin is fixed in the middle section by both the shoulder joint and the shoulder link, the part can be represented by two cantilever beams subjected to a distributed load, as schematized by figure 4.21. To compute the stresses, since the diameter of the part is $D = 6\,mm$ and the wall thickness $t = 3.2\,mm$, the part is considered solid.

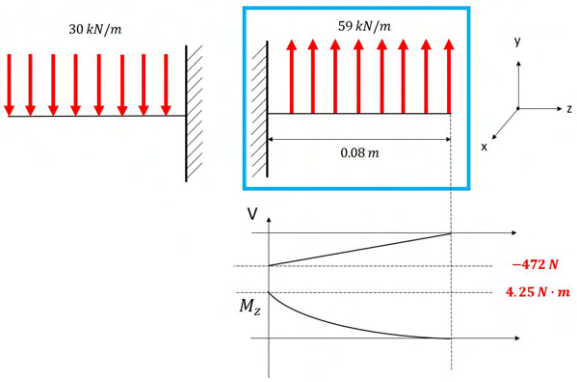

$$I_x = I_y = \frac{\pi \times D^4}{64} = 63.62 \times 10^{-12}\, m^4$$

$$\sigma_{Mx} = \frac{4.25 \times \frac{0.006}{2}}{63.62 \times 10^{-12}} = 200.41\,\text{MPa}$$

$$\tau_{Vy} = \frac{4V}{3A} = \frac{4 \times 472}{3 \times \pi (0.006/2)^2} = 22.26\,\text{MPa}$$

$$\sigma_A = 202.85\,\text{MPa}, \sigma_B = -2.44\,\text{MPa}$$

$$\frac{202.85}{40} - \frac{-2.44}{93.8} = \frac{1}{n} \longrightarrow \textbf{n = 0.20}$$

Figure 4.21: Effort diagram and calculations of the stresses applied in the pin

According to the calculations presented previously, the safety coefficient obtained is significantly lower than the safety factor established. Furthermore, this part is printed vertically, since the only flat surface it possesses is the top, which severely hinders the mechanical resistance of the part, as explained by figure 3.5 in page 28. Consequently, this part can not be manufactured through 3D printing.. Therefore, the M5 ”Chicago” screws with various lengths pictured in figure 4.22 were used. These screws feature an unthreaded outer surface, which allows them to be employed as pins. As these bolts are manufactured using zinc-plated low carbon steel and, according to the manufacturer, correspond to SAE grade 2. Therefore, the minimum ultimate tensile strength of these bolts, according to [110], is 510 MPa which strongly increases the resistance of the pins. These screws are used not only as pins, but throughout the assembly to reduce wear, as mentioned in section 3.6.2, and to facilitate its assembly.

Figure 4.22: Chicago screws used as pins in the exoskeleton assembly

4.4.6 Shoulder Link

The loads that the pin endures are transferred to the shoulder link as schematized by figure 4.23. The width of the rectangular section is $w = 16\,mm$. Applying the stress concentration factors obtained in figure 4.24, the stresses are calculated in the following figure. As the safety coefficient obtained is higher than $n_s = 2.3$, the part satisfies the safety criteria.

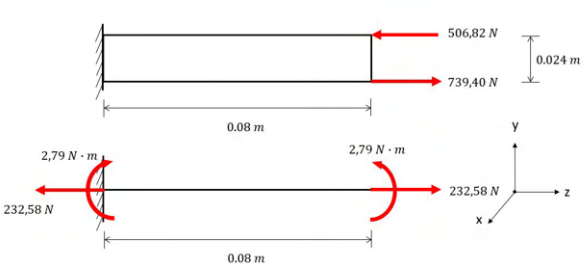

$$I_x = 14.07 \times 10^{-9}\, m^4$$

$$\sigma_{Mx} = 1.8 \frac{2.79 \times 0.024/2}{14.07 \times 10^{-9}} = 4.28\,\text{MPa}$$

$$\sigma_F = 2.19 \frac{F}{A} = 2.19 \frac{232.58}{0.016 \times 0.024} = 1.33\,\text{MPa}$$

$$\sigma_z = 1.33 \pm 4.28\,\text{MPa} \longrightarrow \begin{cases} \sigma_A = 5.61, \sigma_B = 0\,\text{MPa} \\ \sigma_A = 0, \sigma_B = -2.95\,\text{MPa} \end{cases}$$

$$\longrightarrow \begin{cases} n = 29/5.61 = \mathbf{5.17} \\ n = 17.9/2.95 = 6.07 \end{cases}$$

Figure 4.23: Loads applied in the shoulder link and calculations of the stresses applied

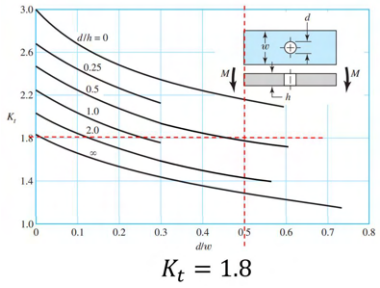

(a) Theoretical stress concentration factors for a bar in bending and in tension with a transverse hole [110]

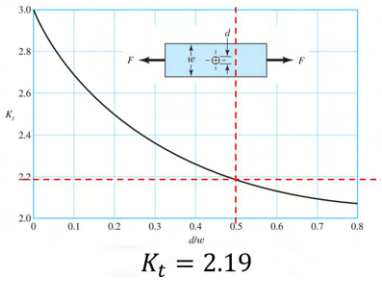

(b) Theoretical stress concentration factors for a bar in bending and in tension with a transverse hole [110]

Figure 4.24: Stress concentration factors for the shoulder link

4.4.7 Back link

As schematized in figure 4.25, the back link is composed of two telescopic rails considered to behave as a cantilever beam, similar to the arm link. It is subjected to a load opposite to the shoulder link analyzed in the previous section.

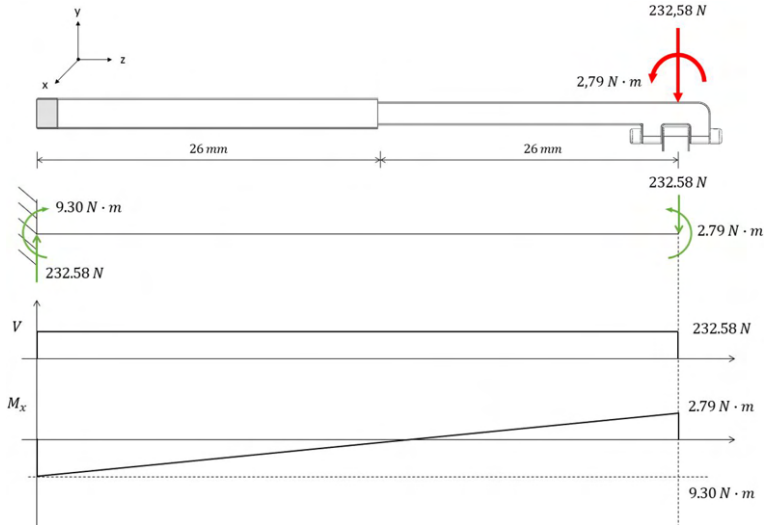

Figure 4.25: Back link loads and effort diagram

As the wall thickness of the outer telescopic bar is 3 mm, and the shell thickness defined in the 3D printing process is 3.2 mm, this component is manufactured as a solid part. The stresses are computed in figure 4.26.

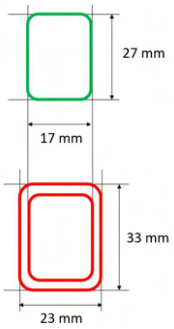

$$I_x = 20.16 \times 10^{-9}$$
$$Q_x = 8.81 \times 10^{-7}$$
$$\sigma_{Mx} = \frac{9.30 \times 0.027/2}{20.16 \times 10^{-9}} = 6.22\,\text{MPa}$$
$$\tau_{V_y} = \frac{232.58 \times 8.81 \times 10^{-7}}{2 \times 0.0032 \times 20.16 \times 10^{-9}} = 1.59\,\text{MPa}$$

$$I_x = 40.99 \times 10^{-9}$$
$$Q_x = 1.58 \times 10^{-6}$$
$$\sigma_{Mx} = \frac{9.30 \times 0.033/2}{40.99 \times 10^{-9}} = 3.74\,\text{MPa}$$
$$\tau_{V_y} = \frac{232.58 \times 1.58 \times 10^{-6}}{2 \times 0.003 \times 40.99 \times 10^{-9}} = 1.49\,\text{MPa}$$

Figure 4.26: Calculation of the stresses exerted in the back telescopic rails

As the stresses are higher for the inner telescopic bar, it is the critical section. Consequently, applying equations 4.21 and 4.22, the safety coefficient is found to be **n = 2.71**.

For comparison purposes, if the part was to have the initial locking mechanism described in section 3.4.2, and according to the chart through which it is possible to obtain a theoretical stress concentration factor of 1.8 for a bar in bending with a transverse hole represented in figure 4.24, the safety coefficient of the inner bar would decrease to $n = 1.57$ and not comply with the safety criteria established.

The fatigue failure analysis was not performed for various reasons. Firstly, as mentioned previously, as the exoskeleton is 3D printed if a part fails it can be easily and promptly replaced by another. On the other hand, it is not likely that the exoskeleton would fail due to fatigue as there are many other events that regularly occur that would damage the exoskeleton before fatigue failure. For example, if the exoskeleton is left in direct exposure to sunlight or placed near hot surfaces, it can be easily damaged. Additionally, as illustrated in figure 3.5, if the exoskeleton is subjected to a shear force it could easily fail. Therefore, if the user accidentally moves their arm into another object, it is very likely that the part in contact would break. Lastly, performing the fatigue failure analysis for polymers and, in particular, 3D printed PLA, is difficult and out of the scope of the present thesis. For more information on the fatigue behavior of 3D printed PLA, the author recommends [113, 114].

Although the analytical calculations are completed and the exoskeleton was redesigned to ensure that the parts comply with the safety criteria established, it is not certain that the parts will not fail. Various assumptions were made in regards to both the behavior of the components and the transfer of the load throughout the exoskeleton. Additionally, most parts were simplified in the calculations, ignoring fillets, curvatures, and other features that influence the mechanical resistance of the parts. Furthermore, although mostly the material properties of a specimen with an infill of 25% were considered, it is printed with a different printer, parameters, and filament than the ones used in the present thesis. Consequently, the properties considered do not completely depict the real behavior of the parts printed. On the other hand, the anisotropic behavior of the material is not taken into account. To better understand the mechanical behavior of the exoskeleton and to confirm that it verifies the safety criteria, a finite element analysis is performed in chapter 5.

Chapter 5

Finite Element Analysis

The finite element analysis (FEA) is a tool commonly used in engineering and in mechanical design for several analyses, including structural. In this chapter, an FEA is performed on the exoskeleton. The framework of the analysis in this specific case is introduced, including the material properties considered, mesh and constraints. In the final section, the results of the analysis are presented and discussed.

5.1 Finite Element Method

The finite element method (FEM) consists of subdividing a domain into smaller, simpler portions, named finite elements. These elements are connected to each other at nodes and make up a mesh that covers the entirety of the domain that is analyzed. This discretization is useful as it simplifies the process of satisfying the equilibrium equations since the elements analyzed are discrete. The finite elements used can be unidimensional line elements, usually used in beams when the larger dimension of the cross-section is at least ten times lower than the length of the element, surface elements, which are 2-dimensional and usually consist of triangular or quadrilateral elements suitable to analyze thin surfaces, or solid elements, that require a larger computational power but are used when line or surface elements are not applicable.

Each element is defined by a vector u that contains the degrees of freedom of all the nodes of the element. For a 3D beam element, for example, there would be six degrees of freedom per node. The displacement of each node can be obtained through the nodal forces and moments vector, f, through equation $\{f\} = [k]\{u\}$. The term [k] is the element's stiffness matrix, a square matrix whose number of columns and rows is the number of degrees of freedom per node, that defines the displacement of each node for a certain set of forces and moments applied. The element stiffness matrix of all the nodes is combined to create [K], the global stiffness matrix. The global stiffness matrix is then used to compute the displacements through equation 5.1.

$$\{F\} = [K]\{U\} \tag{5.1}$$

To solve equation 5.1, the boundary conditions of each node and the external loads applied must be specified. For example, if a certain node has all its degrees of freedom fixed, the elements of the U vector concerning that node should be set to 0. Afterward, the equation can be solved by inverting the K matrix. However, inverting this matrix, especially when there are thousands of degrees of freedom involved, is not efficient. Therefore, finite element software are usually employed to iteratively obtain the displacement through various methods. Abaqus uses the Newton method for nonlinear analysis [115].

The steps mentioned previously are performed on the software Abaqus [116] to analyze the structural behavior of the exoskeleton.

5.2 FEA Setup

To analyze the exoskeleton model it is necessary to resort to a dynamic nonlinear analysis, since the presence of an elastic material creates a nonlinear problem, with a time step of 0.1 seconds.

5.2.1 CAD Model

To facilitate the FEA and reduce the necessary computational time and cost, the CAD model of the exoskeleton is simplified. For this reason, all fillets with a radius of less than 5 mm were deleted, the elastic supports and the connecting element from the forearm link to the elbow joint were merged into other parts, the curvature of the forearm link and the locking mechanism of the telescopic rails were eliminated, and all the connecting elements such as bolts and nuts were omitted. Furthermore, the clearances designed to allow the assembly of different 3D printed parts were excluded and the elastic bands were modeled. The comparison between the original model and the simplified model is represented in figure 5.1.

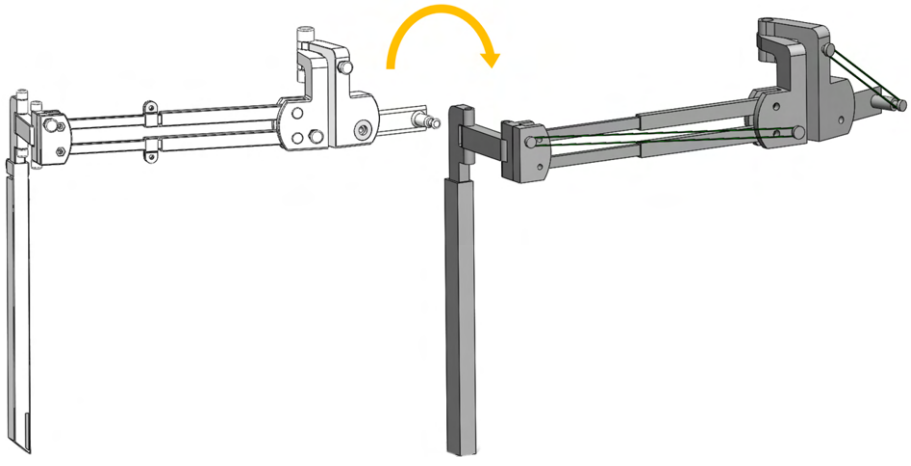

Figure 5.1: Comparison between the original CAD model (left) and the CAD model used to perform the FEA (right)

5.2.2 Material Properties

The FEA of 3D printed parts has some particularities mainly due to the infill of the components. In literature, there have been articles that perform the analysis considering the internal cellular structure of the 3D printed parts such as in [117]. Additionally, I. Gonabadi et al. [118] use finite element microstructural modeling to investigate the effect of 3D printing parameters such as infill density and build orientation. However, in the present FEA, due to both the complexity of the parts and the subsequent assembly, and the excessive computation cost and time, the components of the exoskeleton are treated as solid parts and the internal cellular nature of the parts is only taken into account in the material properties of the PLA. Since a nonlinear analysis is performed, it is necessary to input the stress-strain curve of the PLA filament with a 25% infill density, as presented in figure 3.8.

The material of the elastic element is rubber. Rubber-like materials, named elastomers, are very elastic materials that endure large deformations even when a relatively small load is applied. Elastomers generally have a low Young's modulus and a high failure strain in comparison to other polymers. To model the behavior of these polymers in the FEA software it is necessary to use a hyperelastic material model. Hyperelastic models are used for modeling elastomers in which there is a large strain and nonlinear behavior. Although there are several hyperelastic models proposed in the literature and available in Abaqus that describe the material's behavior through a strain energy density function, the Ogden hyperelastic model is considered [119].

In the Odgen model, the strain energy density is expressed according to the principal stresses in the three directions of the strain tensor, λ_1, λ_2 and λ_3, through equation 5.2.

$$W = \sum_{i=1}^{N} \frac{\nu_i}{\alpha_i}(\lambda_1^i + \lambda_2^i + \lambda_1^i - 3) + \sum_{k=1}^{N} \frac{1}{D_k}(J-1)^{2k} \tag{5.2}$$

Where N is the order of the model, ν_i and α_i material constants, and D_i an incompressible parameter. If $N = 1$ the model is equivalent to the neo-Hookean model and if $N = 2$ the model is identical to the Mooney-Rivlin hyperelastic model. When the order of the model is equal to 3 ($N = 3$), as is the case of the current FEA, it is suitable to model elastomers that undergo strains of up to 700%.

The input parameters for the Ogden model were obtained directly through the Abaqus online database, which provides experimental data for rubber in uniaxial tension, biaxial tension, and pure shear [120].

5.2.3 Mesh

The finite elements used to discretize the exoskeleton are quadratic, or second-order, elements. These elements can have curved edges, realistically simulating geometric curvatures subsequent of the deformation, whereas the edges of first-order elements must remain straight. Furthermore, the analysis is performed using three-dimensional 10-nodes tetrahedral elements. For the PLA printed parts, $C3D10$ elements were used. However, for the elastic bands, it was necessary to use $C3D10HS$ elements that exhibit improved convergence when the material approaches the incompressible limit, i.e, when the material's Poisson's ratio is higher than 0.45, as is the case with rubber, and allowed the convergence of the simulation.

All parts were meshed independently and various mesh controls were applied mostly to curved surfaces or in the vicinity of holes, where the mesh was not uniform. The total number of elements used in the analysis is 87231, amounting to 145083 nodes.

5.2.4 Constraints

The constraints defined by the user in an FEA limit the motion of the exoskeleton and its degrees of freedom. The constraints should closely mimic what happens in reality in order to ensure that the results of the analysis are accurate. For the FEA, the exoskeleton was placed in the position at which the maximum torque occurs, as per table 4.2 in page 55. As the parts were meshed independently, the relations between each one are defined through constraints, interactions, and connectors.

For the joints, hinge connectors were imposed to constrain rotation, except around the axis in which it rotates, and translation. Furthermore, Multi-Point Constraints (MPCs) are applied in the holes to ensure that the joints are fully defined, without introducing the pins into the simulation. The telescopic rails are fixed in the maximum extension position, as the analysis is being performed in the configuration that maximizes the stresses applied. It is important to note that the forearm joint is fixed in every direction, to ensure the convergence of the solution.

The elastic bands are in contact with the elastic support features. This interaction is simulated using surface to surface contacts. It is assumed that the normal behavior of the surfaces is ”hard”, i.e, the surfaces separate when the contact pressure between them becomes zero or negative, and that the tangential behavior has a friction coefficient of $\mu = 0.3$.

5.2.5 Loads and Boundary Conditions

A decentered load is applied linearly over the analysis until its maximum value of 22.6 N is reached, as represented in figure 4.3 in page 54. Additionally, the bottom face of the back link is fixed in all directions, as this link is connected to the body through a belt.

With all the connectors, loads and constraints applied, and the part meshed, as presented in figure 5.2, the dynamic analysis was initiated. After completion, the results presented in the next section were obtained.

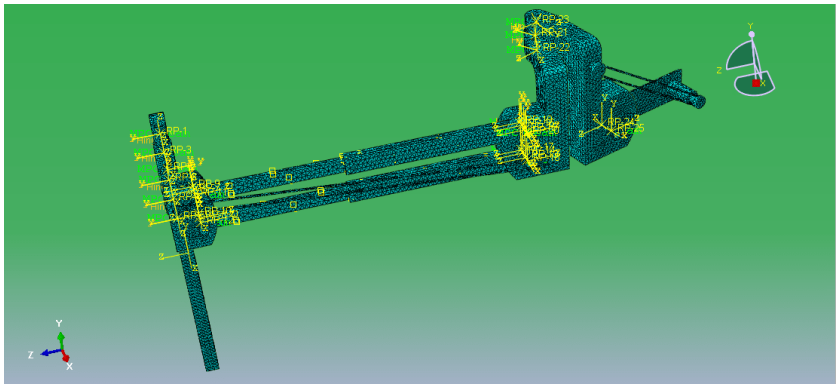

Figure 5.2: Configuration of the exoskeleton for the FEA

5.3 Results and Discussion

5.3.1 Displacement

The displacement of the exoskeleton obtained through the FEA analysis is represented in figure 5.3.

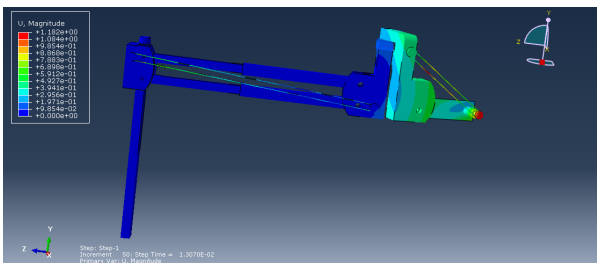

(a) Displacement at increment 50

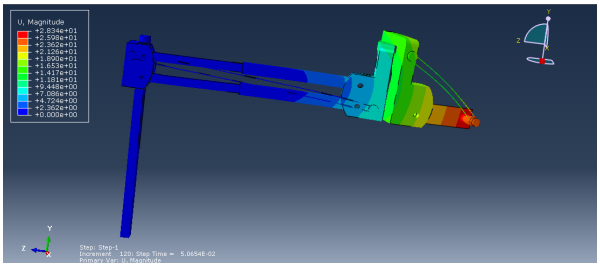

(b) Displacement at increment 120

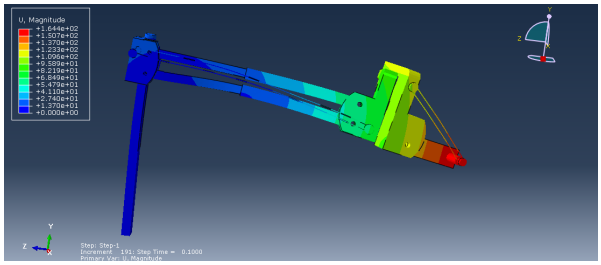

(c) Displacement at the final increment

Figure 5.3: Displacement of the exoskeleton, using a scaling factor of 5, in mm

It can be noticed that, until increment 120, the displacement of the structure of the exoskeleton is minimal, with a maximum displacement magnitude of approximately 2 mm in the forearm link. However, after this step, the elastic band is not sufficient to endure the increase in the load and the exoskeleton displaces more prominently. It is, consequently, clear that a regular elastic band with a 2 mm width is not sufficient to provide a zero-gravity sensation to an adult with an extended arm and, to provide this experience to a user in this configuration, the stiffness of the elastic band should be increased or more elastic bands could be added. Furthermore, after this instant, the exoskeleton deforms and the distance between the two elastic support features decreases, and the elastic bands deform, contrary to what would happen in reality.

Furthermore, when the total load of 22.6 N is applied, in increment 191, the maximum displacement of the exoskeleton occurs. As expected, the maximum magnitude of the displacement occurs in the forearm link and is equal to, approximately, 16 cm. This value is expected since the elastic does not impede the displacement of the exoskeleton when the total load is applied. In the upper arm part of the exoskeleton, however, the displacement is practically neglectable, as displacements of less than 5 mm are recorded.

5.3.2 Strain

The strain of the exoskeleton obtained through the FEA analysis is presented in figure 5.4.

Initially, the elastic bands and the elastic support features have the highest strains, while the structure

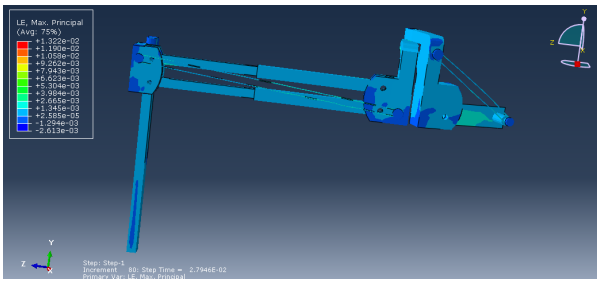

(a) Strain at increment 80

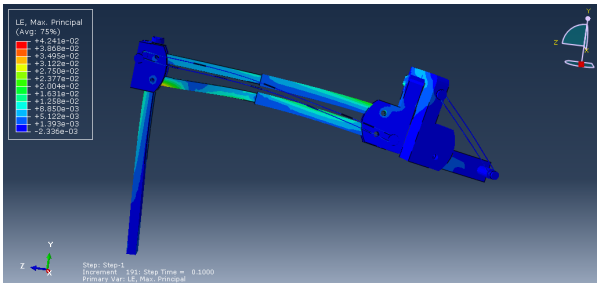

(b) Strain at the final increment

Figure 5.4: Strain of the exoskeleton

of the exoskeleton has neglectable strains. However, as the total load is applied, the elastic bands suffer from a compressive strain, as the exoskeleton deforms to a position where the length of the elastics is decreased, as explained in the previous section. At the final increment, the strain is mostly compressive, while the upper telescopic link is mainly in tension, as expected.

5.3.3 Von-Mises Stress

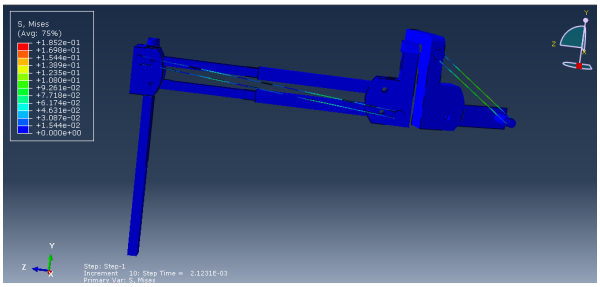

(a) Stress at increment 10

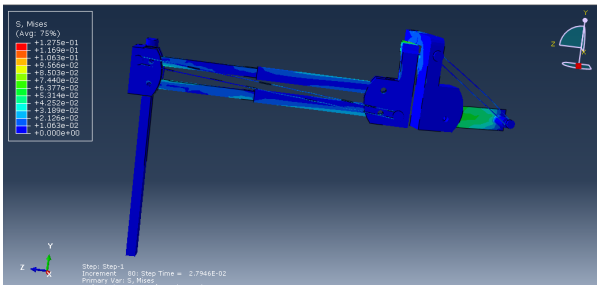

(b) Stress at increment 80

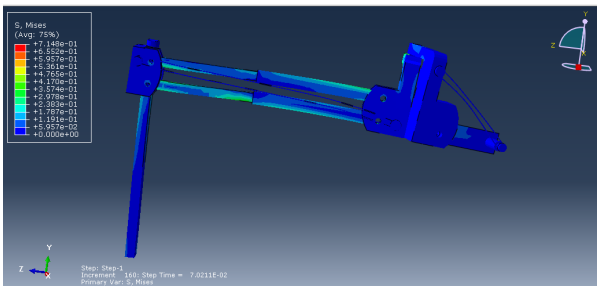

(c) Stress at increment 160

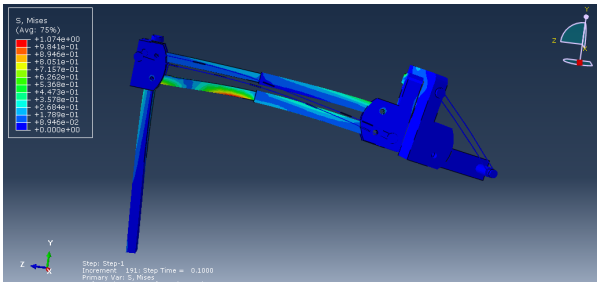

(d) Stress at the final increment

Figure 5.5: Von-Mises stress in the exoskeleton, in MPa

The results of the FEA regarding the Von-Mises stress are represented in figure 5.5. In the first instants, the only elements that suffer stress, although very little, are the elastics bands countering the load. Afterward, the stresses applied in the structure of the exoskeleton increase, particularly in the telescopic links. When the total load is applied, higher stress values are observed in the bottom telescopic link. This occurs due to the fact that the telescopic bars are fixed to one another and, consequently, the inner bar is constrained, causing an increase of stress in that section, as observed in figure 5.5 (d), a fact not taken into account in the analytical calculations.

However, it is noticeable that the elastic bands are not mirroring their true behavior and the assumptions made through the analytical analysis. Furthermore, as the parts are considered solid, it is normal that the stresses registered in the FEA are lower than the results obtained in chapter 4. For example, the maximum stress recorded is 1.074 MPa, in the telescopic rails, which is significantly lower than the stress of 7.67 MPa obtained in section 4.4.3.

Nevertheless, as in the analytical analysis, the parts that suffer the higher stresses are found to be the bottom bar of the telescopic upper arm link and the back link.

5.3.4 Final Observations

The FEA results are acceptable, as the behavior of the parts is reasonable, although more accurate in the initial steps when the elastic is countering the gravitational force. However, this analysis still entails several limitations.

To perform the FEA, the length of the elastic bands was assumed to be approximately double the distance between the elastic features. As, initially, the elastic is not being extended, it is not exerting any tension in the exoskeleton. This is not actually true as the elastic must be extended when mounted, to compensate for gravity. Therefore, the elastic bands in the FEA do not entirely simulate the actual behavior of these elements, which decreases the accuracy of the analysis. In the Von-Mises stress analysis, specifically, it is noticeable that the load is not exactly transferred through the exoskeleton as assumed previously in chapter 4, as the elastic bands do not exert a compressive load as high as expected in the final increments of analysis. Nevertheless, the first increments are considered to correctly depict the behavior of the exoskeleton and, when the total load is applied, it is possible to identify possible critical sections, and the stress distribution through the exoskeleton, although presenting lower values, is in accordance to the analytical analysis.

Additionally, to reduce computation time and cost, the parts were simplified, potentially erasing possible critical sections. The parts are also considered solid. Moreover, the anisotropic behavior of the material is not simulated, neglecting the effect of build orientation on the resistance of a part to certain loads.

To assure the safety of the exoskeleton, the limitations mentioned in the previous paragraphs would have to be mitigated, to obtain a more realistic analysis. Nevertheless, the FEA performed provides valuable information regarding the stress distribution and the load transfer in the exoskeleton, that corroborates the assumptions made in the analytical calculations.

Chapter 6

Final Prototype

In this chapter, the final design of the exoskeleton is presented and the process of 3D printing the final prototype is outlined. Additionally, the features of the final prototype are analyzed and the usage experience is described. Lastly, the overall cost of the exoskeleton is computed.

6.1 3D printing

The final CAD model, presented in the figure 6.1, is converted into G-code and 3D printed, to produce the prototype. This design includes all the improved components according to the areas of improvement identified in the first prototype, in chapter 3, and to the analytical calculations performed in chapter 4.

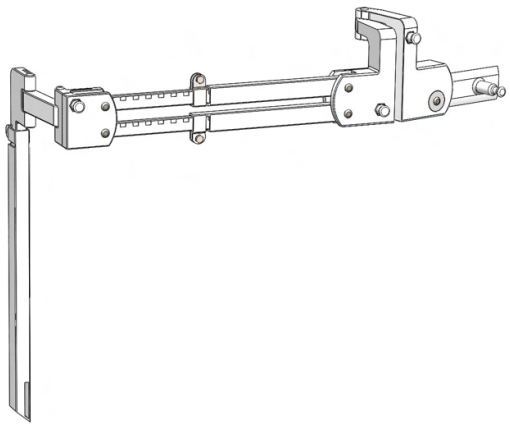

Figure 6.1: Final CAD design of the exoskeleton

The 3D printing process of the final prototype follows the parameters for PLA defined in table A.4, with the exception that the infill density is increased to 25%, and the number of outer perimeter shells is raised to eight. For the TPU straps, the infill density was increased to 20%. The build statistics of the 3D printing process of the final prototype presented in table 6.1, indicate that the 3D printed structure of the exoskeleton takes, approximately, 48 hours to print, excluding the time spent removing support features and preheating the bed and the extruder.

Table 6.1: Build statistics of the 3D printing of the final prototype

Part Name	Filament Material	Number of Parts	Filament Length	Material Cost	Printing Time
Strap	TPU	4	4426.9 mm	0.65 €	178 minutes
Elastic Support Element	PLA	3	854.4 mm	0.05 €	17 minutes
Shoulder Link	PLA	1	8817.7 mm	0.53 €	97 minutes
Forearm Link	PLA	1	14819.6 mm	0.89 €	173 minutes
Outer Telescopic Arm Link	PLA	2	7413.6 mm	0.44 €	90 minutes
Inner Telescopic Arm Link	PLA	2	4332.0 mm	0.27 €	42 minutes
Outer Telescopic Back Link	PLA	1	15821.2 mm	0.95 €	210 minutes
Inner Telescopic Back Link	PLA	1	19053.4 mm	1.15 €	208 minutes
Elbow Joint	PLA	1	72313.4 mm	4.35 €	741 minutes
Shoulder Joint	PLA	1	20464.7 mm	1.23 €	235 minutes
			Total	13.53 €	47 hours and 49 minutes

6.2 Final Exoskeleton

The final printed prototype, with the elastics and the bolts placed, is photographed while worn in figure 6.2. The full assembly of the exoskeleton is extremely lightweight, weighing only 0.47 kg with all the connecting elements and straps included. It can also be folded into a compact position, without any dismount necessary, that allows for easy transportation.

(a) Back view of the final exoskeleton prototype

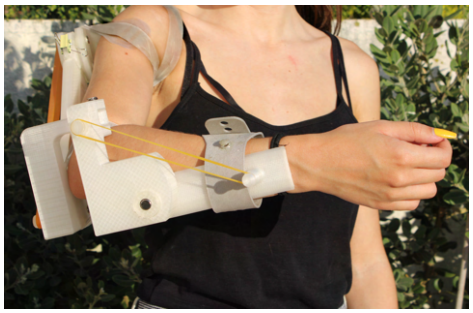

(b) Front view of the final exoskeleton prototype

Figure 6.2: Final prototype of the exoskeleton being worn

It is important to note that, in this prototype, a locking solution different from the screws previously used in the first prototype was implemented. As seen in figure 6.3 (a), foldback clips were used to lock the telescopic rail. This solution is practical as tightening the bolts is not necessary and, in case the necessary screws are not available, clips are easily obtainable. Rubber O-rings are also added to reduce wear on the surface of PLA 3D printed parts, as photographed in figure 6.3 (b).

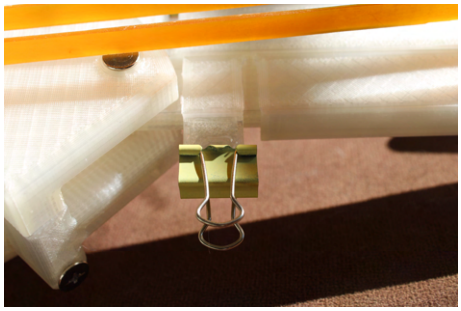

(a) Locking mechanism of the telescopic rails using a foldback clip

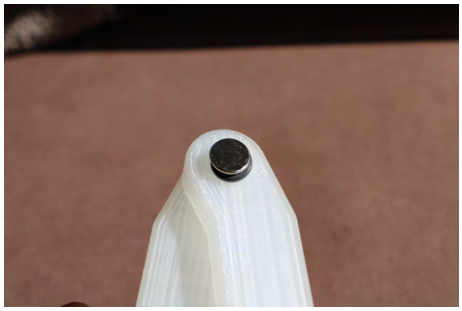

(b) Detail of a rubber O-ring

Figure 6.3: Details of the exoskeleton

6.3 Usage Experience

After mounted, the exoskeleton was relatively easy to put on. However, the help of another individual significantly facilitates the process and allows for the exoskeleton to be put on in less than one minute. The exoskeleton is comfortable, as the parts in direct contact with the user are manufactured in TPU, which is smooth and non-irritable on the skin. To secure the exoskeleton to the hips, using a belt both attached to the exoskeleton and to the pants provides a very secure fit that rarely requires adjustment. When worn, the exoskeleton, especially when manufactured with a transparent filament, is discrete and aesthetically pleasing.

The exoskeleton provides a flotation sensation where the upper limbs feel weightless. The arm movement requires very little effort, except when countering the elastic force, for example, to lower the arms. The structure can also be used for several hours throughout the day. To test how the exoskeleton behaves in various day-to-day activities, the exoskeleton was worn for a whole day. During this day, the exoskeleton was used in a car ride, without requiring any readjustments throughout or after the trip. Although with harsh movements and bending the vertical position of the elbow and shoulder joint necessary to ensure gravity compensation is compromised, it is rapidly corrected when a normal standing position is resumed. Even when used throughout a long period of time, the exoskeleton was not incommodious and it is easy to forget that it is being worn. The exoskeleton also permits the user to perform all essential ADLs defined in chapter 1. The joints are not rigid and the movement of the exoskeleton is smooth and fluid. As various connections to the body were added, the structure moves in accordance with the user's natural movement and is extremely compliant. For the same reason, the exoskeleton has minimal interference with the environment and it is possible to write or use the computer while wearing it.

Overall, the exoskeleton provides a satisfactory, and even enjoyable, usage experience, and the main limitations of the WREX regarding patients' experience with the exoskeleton are mitigated.

6.4 Cost Analysis

The total cost of the exoskeleton is computed in the following table. Table 6.2 also presents all the components that integrate the exoskeleton, apart from the 3D printed structure. To calculate the cost of the 3D printing process, it is necessary to take not only the filament cost into account but also the cost of the electricity consumed. As the 3D printer used consumes a power of 270 W and considering that the time spent preheating the bed surface and the extruder amounts to approximately two hours, the 3D printer works for 50 h. Therefore, as the average electricity price in Portugal at the moment of writing this thesis is 0.144 €/kWh, it is possible to calculate the electricity cost. It is important to note that all other prices considered, for connecting elements such as screws and bolts, the elastics, and even the filaments, vary according to the manufacture or retailer, for it is possible that the cost of the exoskeleton in other conditions can be significantly different.

Table 6.2: Cost analysis of the final exoskeleton

Category	Item	Quantity	Price	Total Cost
3D printing process	TPU filament	22.13 m	0.15 € / m	3.25€
	PLA filament	177.34 m	0.058 € / m	10.28 €
	Electricity	13 kWh	0.144 € / kWh	1.87 €
Screws	Chicago screw M5 x 60 mm	2	0.57 € / un.	1.14 €
	Chicago screw M5 x 40 mm	1	0.50 € / un.	0.50 €
	Chicago screw M5 x 35 mm	1	0.43 € / un.	0.43 €
	Chicago screw M5 x 30 mm	4	0.35 € / un.	1.4 €
	Hex Screw Grade AB ISO 4017 M5 x 10 mm	3	0.08 € / un.	0.24 €
	Hex Nut Grade C ISO 4035 M5	3	0.03 € / un.	0.09 €
Additional features	Small elastics (120*3 mm)	1	0.10 € / un.	0.10 €
	Large elastics (200*8 mm)	1	0.15 € / un.	0.15 €
	Rubber O-Ring M5	16	0.05 € / un.	0.80 €
	Foldback clips (optional)	3	0.15 € / un.	0.45 €
			Final Cost	20.25 €

According to the previous table, the exoskeleton's total material cost is 20.25 €, which represents a decrease of 98% in comparison with the cheapest version of the WREX. In case the user opts for a locking mechanism with foldback clips, the price slightly increases to 20.37 €.

However, it is important to note that the initial investment of acquiring a 3D printer is high. Currently, the price of the Creality CR-10 printer is 380 €, which already includes 0.5 kg of white PLA filament roll, enough to print the structure of the exoskeleton. Nonetheless, there are other options to 3D print the prototype without buying a 3D printer. Firstly, there are many businesses that 3D print CAD files usually for 1 € per hour. Additionally, in recent years, rental services of 3D printers are becoming widely available, providing access to a 3D printer for a week at an average cost of 50 €. Nevertheless, even including the cost of the 3D printer, the exoskeleton is notably cheaper than other similar commercially available exoskeletons. Consequently, the availability of the exoskeleton is significantly increased.

Chapter 7

Conclusions

7.1 Accomplishments

During the course of this thesis, various exoskeletons in multiple areas were analyzed which served as a basis for the design of a new and improved passive upper limb assistive exoskeleton. The final exoskeleton fulfills the objectives stipulated at the beginning of the project.

Firstly, the main goal of designing an exoskeleton that can be used throughout the childhood of the patient until adulthood was fulfilled, as the final design features flexible components that are easily adaptable to the limbs of the user, with practical and intuitive mechanisms. The design of the exoskeleton is ergonomic, with a focus on the patient's comfort, while efficiently assisting upper limb movement. The exoskeleton is easy and rapid to put on and take off, but commodious enough to be used regularly in day-to-day tasks and activities.

Through the final 3D printed prototype it is possible to demonstrate how the exoskeleton behaves when worn. All the essential ADLs initially stated can be comfortably performed while using the prototype. The exoskeleton provides a positive usage experience when worn, allowing compliant and fluid movement of the limbs by providing a zero-gravity sensation.

Since the exoskeleton designed and manufactured in this thesis can be replicated by anyone with access to a 3D printer, at a minimal cost, this project expands the availability of these devices to a significantly larger number of people and, particularly, to disadvantaged patients.

7.2 Future Work

To further ensure the structural integrity of the exoskeleton, the behavior of the exoskeleton when subjected to cycles of fatigue could be analyzed. Additionally, to guarantee more precise calculations, the anisotropic nature of 3D printed parts would have to be taken into account. As through analytical methods, the computation of stresses often implies various assumptions and simplifications, an in-depth FEA where the microstructure of the components is modeled, and the true behavior of the elastic bands is simulated, would culminate in an analysis that closely simulates the real behavior of the exoskeleton.

A simpler analysis considering an orthotropic material could also be performed.

As reported in [25], children with ulnar deviation are unable to eat when using the WREX. Future versions of the exoskeleton can include a mechanism to allow these patients to correct their hand position so that feeding-related tasks can be performed. In other words, an extra passive or active degree of freedom can be added, allowing for elbow pronation and supination. Furthermore, as several children with upper limb musculoskeletal disorders suffer from paralysis that extends to the wrist and the hands, a future redesign of the exoskeleton can include an extension to encompass the wrist and the hand.

The prototype of the exoskeleton was not tested in non-ambulatory users and, therefore, it is not possible to affirm whether it can be adapted and mounted to a wheelchair or sufficiently comfortable to be used by children while sitting in a wheelchair. Further testing of the exoskeleton could ensure that the device is suitable for non-ambulatory patients.

Furthermore, as the exoskeleton was only tested on able-bodied people, relevant and pertinent analysis and study of the experience of disabled patients with the exoskeleton was not performed. To assure that the exoskeleton is beneficial for people with disabilities and to identify potential areas of further improvement, it would be advantageous to perform a clinical study on subjects that suffer from upper limb paralysis.

References

[1] W. H. Organization. World report on disability. Report, World Health Organization, 20 Avenue Appia, 1211 Geneva 27, Switzerland, 2011. URL https://www.who.int/news-room/fact-sheets/detail/musculoskeletal-conditions.

[2] Musculoskeletal conditions, Feb 2021. URL https://www.who.int/news-room/fact-sheets/detail/musculoskeletal-conditions.

[3] B. M. Huisstede, S. M. Bierma-Zeinstra, B. W. Koes, and J. A. Verhaar. Incidence and prevalence of upper-extremity musculoskeletal disorders. a systematic appraisal of the literature. *BMC musculoskeletal disorders*, 7(1):1–7, 2006.

[4] U. N. Economic and S. C. for Western Asia (ESCWA). Accessibility for the disabled, 2004. URL https://www.un.org/esa/socdev/enable/designm/.

[5] T. Tokarski and D. Roman-Liu. Influence of disability type on upper-limb motor skills. *International Journal of Occupational Safety and Ergonomics*, 22(4):463–472, 2016.

[6] Y. Shen, P. W. Ferguson, and J. Rosen. Upper limb exoskeleton systems—overview. In *Wearable Robotics*, pages 1–22. Elsevier, 2020.

[7] A. Owen-Hill. URL https://blog.robotiq.com/a-beginners-guide-to-the-exoskeleton-industry.

[8] A. A. LLP. Global $1.9bn smart exoskeleton market by component, type, body part, application, and region - forecast to 2025, Sep 2019.

[9] L. Taylor. Musculoskeletal disorders in children and young people. URL https://oshwiki.eu/wiki/Musculoskeletal_Disorders_in_Children_and_Young_People#Symptoms_and_Effects_of_MSDs_in_Children_and_young_People.

[10] K. J. Little and R. Cornwall. Congenital anomalies of the hand—principles of management. *Orthopedic Clinics*, 47(1):153–168, 2016.

[11] Congenital limb disorders, Aug 2020. URL https://www.ortho-institute.org/patient-care/orthopedic-specialties/congenital-limb-disorders/?tabname=overview.

[12] Louisgoddard. Wrex, a 3d-printed robotic exoskeleton for disabled children, Aug 2012. URL https://www.theverge.com/2012/8/5/3219685/wrex-robotic-exoskeleton-arm-3d-printing.

[13] L. T. Staheli, J. G. Hall, K. M. Jaffe, and D. O. Paholke. *Arthrogryposis: a text atlas*. Cambridge university press, 1998.

[14] J. G. Hall. Arthrogryposis multiplex congenita: etiology, genetics, classification, diagnostic approach, and general aspects. *Journal of pediatric orthopedics. Part B*, 6(3):159–166, 1997.

[15] J. Pearn. Incidence, prevalence, and gene frequency studies of chronic childhood spinal muscular atrophy. *Journal of medical genetics*, 15(6):409–413, 1978.

[16] A. Theadom, M. Rodrigues, R. Roxburgh, S. Balalla, C. Higgins, R. Bhattacharjee, K. Jones, R. Krishnamurthi, and V. Feigin. Prevalence of Muscular Dystrophies: A Systematic Literature Review. *Neuroepidemiology*, 43(3-4):259–268, 2014. ISSN 0251-5350. doi: 10.1159/000369343. URL https://www.karger.com/DOI/10.1159/000369343.

[17] Physiopedia. Upper limb function in spinal cord injury — physiopedia,, 2020. URL https://www.physio-pedia.com/index.php?title=Upper_Limb_Function_in_Spinal_Cord_Injury&oldid=228501. [Online; accessed 7-March-2021].

[18] M. Gandolla, A. Antonietti, V. Longatelli, and A. Pedrocchi. The Effectiveness of Wearable Upper Limb Assistive Devices in Degenerative Neuromuscular Diseases: A Systematic Review and Meta-Analysis. *Frontiers in Bioengineering and Biotechnology*, 7:450, jan 2020. doi: 10.3389/fbioe.2019.00450.

[19] T. Shank, M. Eppes, J. Hossain, M. Gunn, and T. Rahman. Outcome Measures with COPM of Children using a Wilmington Robotic Exoskeleton. *The Open Journal of Occupational Therapy*, 5, jan 2017. doi: 10.15453/2168-6408.1262.

[20] K. Weber. Child anthropometry for restraint system design. Technical report, 1985.

[21] E. Churchill and J. T. McConville. Sampling and data gathering strategies for future usaf anthropometry. 1976.

[22] M. A. McDowell, C. D. Fryar, C. L. Ogden, and K. M. Flegal. Anthropometric reference data for children and adults: United states, 2003–2006. *National health statistics reports*, 10(5), 2008.

[23] C. Anglin and U. Wyss. Review of Arm Motion Analyses. *Proceedings of the Institution of Mechanical Engineers. Part H, Journal of engineering in medicine*, 214:541–555, feb 2000. doi: 10.1243/0954411001535570.

[24] I. A. Murray and G. R. Johnson. A study of the external forces and moments at the shoulder and elbow while performing every day tasks. *Clinical Biomechanics*, 19(6):586–594, 2004. ISSN 0268-0033. doi: https://doi.org/10.1016/j.clinbiomech.2004.03.004. URL https://www.sciencedirect.com/science/article/pii/S0268003304000531.

[25] T. Rahman, W. Sample, S. Jayakumar, M. King, J. Wee, R. R. Seliktar, M. Alexander, M. Scavina, and A. Clark. Passive exoskeleton for assisting limb movement. *Journal of rehabilitation research and development*, 43:583–590, aug 2006. doi: 10.1682/JRRD.2005.04.0070.

[26] T. Rahman, W. Sample, R. Seliktar, M. T. Scavina, A. L. Clark, K. Moran, and M. A. Alexander. Design and testing of a functional arm orthosis in patients with neuromuscular diseases. *IEEE Transactions on Neural Systems and Rehabilitation Engineering*, 15(2):244–251, 2007.

[27] exoskeleton (n.). URL https://www.etymonline.com/word/exoskeleton#etymonline_v_32863.

[28] C. King. The homeric corslet. *American Journal of Archaeology*, 74(3):294–296, 1970.

[29] V. Kumar, Y. V. Hote, and S. Jain. Review of exoskeleton: History, design and control. In *2019 3rd International Conference on Recent Developments in Control, Automation Power Engineering (RDCAPE)*, pages 677–682, 2019. doi: 10.1109/RDCAPE47089.2019.8979099.

[30] B. R. Fick and J. B. Makinson. Hardiman i prototype for machine augmentation of human strength and endurance. Technical report, GENERAL ELECTRIC CO SCHENECTADY NY SPECIALTY MATERIALS HANDLING PRODUCTS . . . , 1971.

[31] r. Mihailo Pupin Institute Robotics Laboratory. Robotics laboratory. URL https://www.pupin.rs/RnDProfile/history.html.

[32] B. Rupal, A. Singla, and G. Virk. *Lower Limb Exoskeletons: A Brief Review*. jan 2016.

[33] R. Bogue. Exoskeletons–a review of industrial applications. *Industrial Robot: An International Journal*, 2018.

[34] Y. Sankai. Hal: Hybrid assistive limb based on cybernics. In *Robotics research*, pages 25–34. Springer, 2010.

[35] Advanced technologies for movement rehabilitation. URL https://www.hocoma.com/.

[36] Rewalk robotics - more than walking, Dec 2020. URL https://rewalk.com/.

[37] Guardian® xo® full-body powered exoskeleton, Dec 2020. URL https://www.sarcos.com/products/guardian-xo-powered-exoskeleton/.

[38] K. Yamamoto, K. Hyodo, M. Ishii, and T. Matsuo. Development of power assisting suit for assisting nurse labor. *JSME International Journal Series C Mechanical Systems, Machine Elements and Manufacturing*, 45(3):703–711, 2002.

[39] K. L. English, N. J. Newby, K. J. Hackney, J. K. DeWitt, C. E. Beck, R. N. Rovekamp, R. L. Rea, and L. L. Ploutz-Snyder. Comparison of knee and ankle dynamometry between nasa's x1 exoskeleton and biodex system 4. 2014.

[40] N. Costa and D. G. Caldwell. Control of a biomimetic" soft-actuated" 10dof lower body exoskeleton. In *The First IEEE/RAS-EMBS International Conference on Biomedical Robotics and Biomechatronics, 2006. BioRob 2006.*, pages 495–501. IEEE, 2006.

[41] P. Agarwal and A. D. Deshpande. Exoskeletons: State-of-the-art, design challenges, and future directions. In *Human Performance Optimization*, pages 234–259. Oxford University Press.

[42] R. Ozawa, K. Hashirii, and H. Kobayashi. Design and control of underactuated tendon-driven mechanisms. In *2009 IEEE International Conference on Robotics and Automation*, pages 1522–1527, 2009. doi: 10.1109/ROBOT.2009.5152222.

[43] D. Hambling. Why russian military exoskeletons are not science fiction, Aug 2020. URL https://www.forbes.com/sites/davidhambling/2020/08/19/why-russian-military-exoskeletons-are-not-science-fiction/?sh=7f55254f648d.

[44] Home. URL https://www.suitx.com/.

[45] L. Van Engelhoven, N. Poon, H. Kazerooni, D. Rempel, A. Barr, and C. Harris-Adamson. Experimental evaluation of a shoulder-support exoskeleton for overhead work: Influences of peak torque amplitude, task, and tool mass. *IISE Transactions on Occupational Ergonomics and Human Factors*, 7(3-4):250–263, 2019.

[46] H. Kazerooni, W. Tung, and M. Pillai. Evaluation of trunk-supporting exoskeleton. In *Proceedings of the Human Factors and Ergonomics Society Annual Meeting*, volume 63, pages 1080–1083. SAGE Publications Sage CA: Los Angeles, CA, 2019.

[47] M. V. Pillai, L. Van Engelhoven, and H. Kazerooni. Evaluation of a lower leg support exoskeleton on floor and below hip height panel work. *Human factors*, 62(3):489–500, 2020.

[48] Skelex 360-xfr. URL https://www.skelex.com/skelex-360-xfr/.

[49] P. D. United Nations, Department of Economic and Social Affairs. World Population Ageing 2017 - Highlights. Technical report, United Nations, 2017. URL https://www.un.org/en/development/desa/population/publications/pdf/ageing/WPA2017_Highlights.pdf.

[50] C. E. Gray, J. D. Barnes, J. C. Bonne, C. Cameron, J.-P. Chaput, G. Faulkner, I. Janssen, P. T. Katzmarzyk, A. M. Kolen, S. R. Manske, et al. Results from canada's 2014 report card on physical activity for children and youth. *Journal of Physical Activity and Health*, 11(s1):S26–S32, 2014.

[51] B. S. Rupal, S. Rafique, A. Singla, E. Singla, M. Isaksson, and G. S. Virk. Lower-limb exoskeletons: Research trends and regulatory guidelines in medical and non-medical applications. *International Journal of Advanced Robotic Systems*, 14(6):1729881417743554, 2017.

[52] A. Kapeller, M. H. Nagenborg, and K. Nizamis. Wearable robotic exoskeletons: A socio-philosophical perspective on duchenne muscular dystrophy research. *Paladyn, Journal of Behavioral Robotics*, 11(1):404–413, 2020.

[53] S. Paul, M. Rafal, and A. Houtenville. 2020 annual disability statistics compendium. *Institute on Disability, University of New Hampshire*, 2020.

[54] A. Singh, L. Tetreault, S. Kalsi-Ryan, A. Nouri, and M. G. Fehlings. Global prevalence and incidence of traumatic spinal cord injury. *Clinical epidemiology*, 6:309, 2014.

[55] M. Pugliatti, S. Sotgiu, G. Rosati, et al. The worldwide prevalence of multiple sclerosis. *Clinical neurology and neurosurgery*, 104(3):182–191, 2002.

[56] A. M. Grabowski and H. M. Herr. Leg exoskeleton reduces the metabolic cost of human hopping. *Journal of Applied Physiology*, 107(3):670–678, 2009.

[57] C. J. Walsh, K. Endo, and H. Herr. A quasi-passive leg exoskeleton for load-carrying augmentation. *International Journal of Humanoid Robotics*, 4(03):487–506, 2007.

[58] L. M. Mooney, E. J. Rouse, and H. M. Herr. Autonomous exoskeleton reduces metabolic cost of walking. In *2014 36th Annual International Conference of the IEEE Engineering in Medicine and Biology Society*, pages 3065–3068. IEEE, 2014.

[59] A. Esquenazi, M. Talaty, A. Packel, and M. Saulino. The rewalk powered exoskeleton to restore ambulatory function to individuals with thoracic-level motor-complete spinal cord injury. *American journal of physical medicine & rehabilitation*, 91(11):911–921, 2012.

[60] G. Zeilig, H. Weingarden, M. Zwecker, I. Dudkiewicz, A. Bloch, and A. Esquenazi. Safety and tolerance of the rewalk™ exoskeleton suit for ambulation by people with complete spinal cord injury: A pilot study. *The journal of spinal cord medicine*, 35(2):96–101, 2012.

[61] V. Karas, V. M. Wang, A. Dhawan, and B. J. Cole. Biomechanical factors in rotator cuff pathology. *Sports medicine and arthroscopy review*, 19(3):202–206, 2011.

[62] J. A. Leal-Naranjo, M. Ceccarelli, C. T. Miguel, and D. Cafolla. An experimental characterization of human arm motion. 2016.

[63] P. LETIER and A. Preumont. *P. LETIER A. PREUMONT, Portable Haptic Arm Exoskeleton, Chapter 5 of Prototyping of Robotic Systems: Applications of Design and Implementation, Tarek Sobh Xingguo Xiong, Editors. pp.122-145, Information Science Reference, IGI Global, 2012.*, pages 122–145. 2012.

[64] S. K. Manna and S. Bhaumik. A Bioinspired 10 DOF Wearable Powered Arm Exoskeleton for Rehabilitation. *Journal of Robotics*, 2013:741359, 2013. ISSN 1687-9600. doi: 10.1155/2013/741359. URL `https://doi.org/10.1155/2013/741359`.

[65] P. H. Gøytil, D. Padovani, and M. R. Hansen. On the energy efficiency of dual prime mover pump-controlled hydraulic cylinders. In *Fluid Power Systems Technology*, volume 59339, page V001T01A016. American Society of Mechanical Engineers, 2019.

[66] Medical robotics solutions for stroke, bpi, upper limb paralysis, Sep 2021. URL `https://myomo.com/`.

[67] Myopro. URL `https://www.neurorehabdirectory.com/rehab-products/myopro/`.

[68] S. Dunaway, D. B. Dezsi, J. Perkins, D. Tran, and J. Naft. Case Report on the Use of a Custom Myoelectric Elbow–Wrist–Hand Orthosis for the Remediation of Upper Extremity Paresis and Loss

of Function in Chronic Stroke. *Military Medicine*, 182(7):e1963–e1968, 2017. ISSN 0026-4075. doi: 10.7205/MILMED-D-16-00399. URL https://doi.org/10.7205/MILMED-D-16-00399.

[69] H. T. Peters, S. J. Page, and A. Persch. Giving Them a Hand: Wearing a Myoelectric Elbow-Wrist-Hand Orthosis Reduces Upper Extremity Impairment in Chronic Stroke. *Archives of physical medicine and rehabilitation*, 98(9):1821–1827, sep 2017. ISSN 1532-821X (Electronic). doi: 10.1016/j.apmr.2016.12.016.

[70] G. Anderson, T. Beahrs, M. Kircher, and A. Shin. Use of Myoelectric Limb Orthoses for Elbow Flexion in Patients with Brachial Plexus Injury: A Case Series. *Journal of Prosthetics and Orthotics*, 33:1, nov 2019. doi: 10.1097/JPO.0000000000000284.

[71] S. Pundik, J. McCabe, S. Kesner, M. Skelly, and S. Fatone. Use of a myoelectric upper limb orthosis for rehabilitation of the upper limb in traumatic brain injury: A case report. *Journal of rehabilitation and assistive technologies engineering*, 7:2055668320921067, 2020. ISSN 2055-6683 (Electronic). doi: 10.1177/2055668320921067.

[72] Headquarters news. URL https://news.panasonic.com/global/press/data/en060925-6/en060925-6.html.

[73] Cyberdyne. URL https://www.cyberdyne.jp/english/products/HAL/.

[74] K. Hyakutake, T. Morishita, K. Saita, H. Fukuda, E. Shiota, Y. Higaki, T. Inoue, and Y. Uehara. Effects of Home-Based Robotic Therapy Involving the Single-Joint Hybrid Assistive Limb Robotic Suit in the Chronic Phase of Stroke: A Pilot Study. *BioMed Research International*, 2019:5462694, 2019. ISSN 2314-6133. doi: 10.1155/2019/5462694. URL https://doi.org/10.1155/2019/5462694.

[75] K. Saita, T. Morishita, K. Hyakutake, T. OGATA, H. FUKUDA, S. KAMADA, and T. INOUE. Feasibility of Robot-assisted Rehabilitation in Poststroke Recovery of Upper Limb Function Depending on the Severity. *Neurologia medico-chirurgica*, 60, mar 2020. doi: 10.2176/nmc.oa.2019-0268.

[76] R. L. Smith, J. Lobo-Prat, H. van der Kooij, and A. H. A. Stienen. Design of a perfect balance system for active upper-extremity exoskeletons. In *2013 IEEE 13th International Conference on Rehabilitation Robotics (ICORR)*, pages 1–6, 2013. ISBN 1945-7901 VO -. doi: 10.1109/ICORR.2013.6650376.

[77] K. Huysamen, T. Bosch, M. de Looze, K. S. Stadler, E. Graf, and L. W. O'Sullivan. Evaluation of a passive exoskeleton for static upper limb activities. *Applied ergonomics*, 70:148–155, 2018.

[78] R. L. Smith, J. Lobo-Prat, H. van der Kooij, and A. H. A. Stienen. Design of a perfect balance system for active upper-extremity exoskeletons. In *2013 IEEE 13th International Conference on Rehabilitation Robotics (ICORR)*, pages 1–6, 2013. doi: 10.1109/ICORR.2013.6650376.

[79] R. Altenburger, D. Scherly, and K. S. Stadler. Design of a passive, iso-elastic upper limb exoskeleton for gravity compensation. *Robomech Journal*, 3(1):1–7, 2016.

[80] At-home 3d printing is gaining popularity, Oct 2018. URL https://www.reichelt.com/magazin/en/research-home-3d-printing/.

[81] B. Kianian. Wohlers report 2018: 3d printing and additive manufacturing state of the industry, annual worldwide progress report: Chapter title: Other countries. In *Wohlers Report 2018*. Wohlers Associates, Inc., 2018.

[82] D. Bourell and T. Wohlers. Introduction to additive manufacturing. *Additive Manufacturing*, 24, 2020.

[83] T. Alsop. Most used 3d printing technologies worldwide 2018, Mar 2020. URL https://www.statista.com/statistics/756690/worldwide-most-used-3d-printing-technologies/.

[84] Industrial fdm vs. desktop fdm, . URL https://www.hubs.com/knowledge-base/industrial-fdm-vs-desktop-fdm/.

[85] H. Gonabadi, A. Yadav, and S. Bull. The effect of processing parameters on the mechanical characteristics of pla produced by a 3d fff printer. *The International Journal of Advanced Manufacturing Technology*, 111(3):695–709, 2020.

[86] J. Allison, C. Sharpe, and C. C. Seepersad. Powder bed fusion metrology for additive manufacturing design guidance. *Additive Manufacturing*, 25:239–251, 2019.

[87] Design rules best practices for fff 3d printing. URL https://www.hydraresearch3d.com/design-rules.

[88] Z. Liu, Q. Lei, and S. Xing. Mechanical characteristics of wood, ceramic, metal and carbon fiber-based pla composites fabricated by fdm. *Journal of Materials Research and Technology*, 8(5): 3741–3751, 2019.

[89] Fdm 3d printing materials compared, . URL https://www.hubs.com/knowledge-base/fdm-3d-printing-materials-compared/.

[90] B. Zhang, B. Seong, V. Nguyen, and D. Byun. 3d printing of high-resolution pla-based structures by hybrid electrohydrodynamic and fused deposition modeling techniques. *Journal of Micromechanics and Microengineering*, 26(2):025015, 2016.

[91] S. Singh, G. Singh, C. Prakash, and S. Ramakrishna. Current status and future directions of fused filament fabrication. *Journal of Manufacturing Processes*, 55:288–306, 2020.

[92] MakerBot. Pla and abs strength data. URL 228834597.pdf.

[93] 3d cad design software. URL https://www.solidworks.com/.

[94] J. Van der Vorm, L. OSullivan, R. Nugent, and M. de Looze. Considerations for developing safety standards for industrial exoskeletons. *Robo-Mate*, pages 1–13, 2015.

[95] B. D. Lowe, W. G. Billotte, and D. R. Peterson. Astm f48 formation and standards for industrial exoskeletons and exosuits. *IISE transactions on occupational ergonomics and human factors*, 7 (3-4):230–236, 2019.

[96] T. Yaqoob, H. Abbas, and N. Shafqat. Integrated security, safety, and privacy risk assessment framework for medical devices. *IEEE Journal of Biomedical and Health Informatics*, 24(6):1752–1761, 2020. doi: 10.1109/JBHI.2019.2952906.

[97] A. Baird. Free cad designs, files 3d models: The grabcad community library, Sep 2012. URL https://grabcad.com/library/requested-wilmington-robotic-exoskeleton-wrex.

[98] News amp; views blog. URL https://www.testrite.com/about/blog/5/225/the-world-s-first-infinitely-adjustable-square-telescopic-tube-lock/.

[99] Cr 10 3d printer(czech in stock). URL https://www.creality3dofficial.com/products/creality-cr-10-3d-printer.

[100] Improve your print quality with, Jul 2020. URL https://www.simplify3d.com/.

[101] C. Abeykoon, P. Sri-Amphorn, and A. Fernando. Optimization of fused deposition modeling parameters for improved pla and abs 3d printed structures. *International Journal of Lightweight Materials and Manufacture*, 3(3):284–297, 2020.

[102] R. B. Kristiawan, F. Imaduddin, D. Ariawan, Z. Arifin, et al. A review on the fused deposition modeling (fdm) 3d printing: Filament processing, materials, and printing parameters. *Open Engineering*, 11(1):639–649, 2021.

[103] Tpu 3d printing: A guide to 3d printing flexible parts, Apr 2021. URL https://amfg.ai/2018/07/23/tpu-3d-printing-guide/.

[104] R. Singh and H. K. Garg. Fused deposition modeling–a state of art review and future applications. *Ref. Modul. Mater. Sci. Mater. Eng*, pages 1–20, 2016.

[105] R. Aziz, M. I. Ul Haq, and A. Raina. Effect of surface texturing on friction behaviour of 3D printed polylactic acid (PLA). *Polymer Testing*, 85:106434, may 2020. ISSN 0142-9418. doi: 10.1016/J.POLYMERTESTING.2020.106434.

[106] R. Roy and A. Mukhopadhyay. Tribological studies of 3d printed abs and pla plastic parts. *Materials Today: Proceedings*, 41:856–862, 2021.

[107] M. M. Hanon and L. Zsidai. Comprehending the role of process parameters and filament color on the structure and tribological performance of 3d printed pla. *Journal of Materials Research and Technology*, 15:647–660, 2021.

[108] M. W. Spong, S. Hutchinson, and M. Vidyasagar. Forward kinematics: the denavit-hartenberg convention. *Robot Dynamics and Control, 2nd ed.; John Wiley & Sons: New York, NY, USA*, pages 57–82, 2004.

[109] A. Mauri, J. Lettori, G. Fusi, D. Fausti, M. Mor, F. Braghin, G. Legnani, and L. Roveda. Mechanical and control design of an industrial exoskeleton for advanced human empowering in heavy parts manipulation tasks. *Robotics*, 8(3):65, 2019.

[110] R. G. Budynas, J. K. Nisbett, et al. *Shigley's mechanical engineering design*, volume 9. McGraw-Hill New York, 2011.

[111] W. D. Pilkey, D. F. Pilkey, and Z. Bi. *Peterson's stress concentration factors*. John Wiley & Sons, 2020.

[112] G. Ćwikła, C. Grabowik, K. Kalinowski, I. Paprocka, and P. Ociepka. The influence of printing parameters on selected mechanical properties of fdm/fff 3d-printed parts. In *IOP conference series: materials science and engineering*, volume 227, page 012033. IOP Publishing, 2017.

[113] O. H. Ezeh and L. Susmel. On the fatigue strength of 3D-printed polylactide (PLA). *Procedia Structural Integrity*, 9:29–36, 2018. ISSN 24523216. doi: 10.1016/j.prostr.2018.06.007. URL https://doi.org/10.1016/j.prostr.2018.06.007.

[114] O. H. Ezeh and L. Susmel. Reference strength values to design against static and fatigue loading polylactide additively manufactured with in-fill level equal to 100%. *Material Design and Processing Communications*, 1(4), 2019. ISSN 25776576. doi: 10.1002/mdp2.45.

[115] MIT. URL https://abaqus-docs.mit.edu/2017/English/SIMACAEEXCRefMap/simaexc-c-docproc.htm.

[116] Abaqus unified fea. URL https://www.3ds.com/products-services/simulia/products/abaqus/.

[117] S. Bhandari and R. Lopez-Anido. Finite element modeling of 3D-printed part with cellular internal structure using homogenized properties. *Progress in Additive Manufacturing*, 4, 2019. doi: 10.1007/s40964-018-0070-2.

[118] H. Izadi Gonabadi, Y. Chen, A. Yadav, and S. Bull. Investigation of the effect of raster angle, build orientation, and infill density on the elastic response of 3D printed parts using finite element microstructural modeling and homogenization techniques. *The International Journal of Advanced Manufacturing Technology*, 2021. doi: 10.1007/s00170-021-07940-4.

[119] R. W. Ogden. *Non-linear elastic deformations*. Courier Corporation, 1997.

[120] Hyperelastic test data. URL https://abaqus-docs.mit.edu/2017/English/SIMAINPRefResources/rubberfit_ogden_n2.inp.

[121] C. Schmidleithner and D. M. Kalaskar. Stereolithography. IntechOpen, 2018.

[122] Q. Mu, L. Wang, C. K. Dunn, X. Kuang, F. Duan, Z. Zhang, H. J. Qi, and T. Wang. Digital light processing 3d printing of conductive complex structures. *Additive Manufacturing*, 18:74–83, 2017.

[123] Introduction to sls 3d printing, . URL https://www.hubs.com/knowledge-base/introduction-sls-3d-printing/.

[124] Introduction to metal 3d printing, . URL https://www.hubs.com/knowledge-base/introduction-metal-3d-printing/.

[125] Introduction to material jetting 3d printing, . URL https://www.hubs.com/knowledge-base/introduction-material-jetting-3d-printing/.

[126] Introduction to binder jetting 3d printing, . URL https://www.hubs.com/knowledge-base/introduction-binder-jetting-3d-printing/.

[127] C. Dudescu and L. Racz. Effects of raster orientation, infill rate and infill pattern on the mechanical properties of 3d printed materials. *ACTA Universitatis Cibiniensis*, 69(1):23–30, 2017.

[128] V. Cabreira and R. M. C. Santana. Effect of infill pattern in fused filament fabrication (fff) 3d printing on materials performance. *Matéria (Rio de Janeiro)*, 25, 2020.

[129] M. Leite, J. Fernandes, A. M. Deus, L. Reis, and M. F. Vaz. Study of the influence of 3d printing parameters on the mechanical properties of pla. In *3rd international conference on progress in additive manufacturing (Pro-AM 2018)*, 2018.

[130] F. Othman, T. Alani, and H. Ali. Influence of Layer Thickness on Impact Property of 3D-Printed PLA. 2018.

[131] A. Nugroho, R. Ardiansyah, L. Rusita, and I. L. Larasati. Effect of layer thickness on flexural properties of pla (polylactid acid) by 3d printing. In *Journal of Physics: Conference Series*, volume 1130, page 012017. IOP Publishing, 2018.

[132] J. Khatwani and V. Srivastava. Effect of process parameters on mechanical properties of solidified pla parts fabricated by 3d printing process. In *3D printing and additive manufacturing technologies*, pages 95–104. Springer, 2019.

[133] M. Shahinpoor. *A Robot Engineering Textbook*. Harper & Row, 1987. ISBN 9780060459314. URL https://books.google.pt/books?id=0iJ8AAAAIAAJ.

Appendix A

3D Printing

A.1 3D Printing Processes

Vat photopolymerization

Vat photopolymerization concerns various processes, notably stereolithography (SLA) and Direct Light Processing (DLP), where a photopolymer resin is exposed to certain wavelengths of light to solidify. These processes create parts with a good surface finish and can produce complex and detailed parts. Consequently, these methods are usually employed to manufacture jewelry and for medical applications.

Stereolitography (SLA) consists of depositing a liquid thermoset resin to form a structure that then supports the part in itself. The layers created are exposed to an ultraviolet laser that solidifies the part and, if necessary, the object can then be cured in an UV chamber to complete the solidification of the part and obtain optimal mechanical properties. This process allows for the manufacturing of complex parts and offers great accuracy and excellent surface finish, but involves high costs and is a slow process. Furthermore, the part needs to be stored under certain conditions to remain stable over time and it is only possible to print one resin at a time, which restricts the range of applications of this process [121].

Digital Light Processing (DLP), emerged in 1996 and uses a projector light with a liquid crystal display panel or a deformable mirror to solidify the photopolymer, which allows for a faster process as the entire layer is solidified at once. As SLA, DLP produces parts with high accuracy and resolution but still requires the same post-processing steps. However, only a shallow vat of resin is required to facilitate the process and, consequently, there is less material waste and lower costs [122].

Powder Bed Fusion (PBF)

Powder Bed Fusion (PBF) encompasses the processes that use a heat source to fuse the particles of a polymer or metal powder one layer at a time. The main technologies that use PBF are Selective Laser Sintering (SLS), used for polymers, and Selective Laser Melting (SLM) and Direct Metal Laser Sintering (DMLS), employed to 3D print metals.

In Selective Laser Sintering (SLS) a laser is used to fuse the particles of a polymer powder creating layers that form a part. The parts require post-processing as, after printing, they are encapsulated in

loose powder and the powder bin has to reach room temperature before the parts can be unpacked, which can take up to 12 hours. For this reason, it is important that the build volume of the machine is taken advantage of, as the printing time is independent of the number of parts [123]. The parts must then be cleaned and the remaining powder can be reused. This process produces highly accurate parts with good and uniform mechanical properties and complex parts with hollow sections can be printed. However, SLS parts are brittle and porous.

Selective Laser Melting (SLM) and Direct Metal Laser Sintering (DMLS) are similar 3D printing processes that use a laser scan to sinter metal powder creating layers that form a part. The main difference between these two processes is that while SLM produces parts from a single metal powder, DMLS uses powdered metal alloys and elevated temperatures to fuse the particles with different melting points on a molecular level. The components manufactured through these processes typically do not require further post-processing and have good and practically isotropic mechanical properties, although, because of their rough surface finish, they are more prone to fatigue [124], These processes are usually employed for small-batch production of complex high-quality parts where the use of traditional manufacturing methods is not possible.

Digital Inkjet

Inkjet processes eject through a nozzle liquid phase materials, called inks, in a chamber and are mainly used for electronic applications. This process is similar to the one used by traditional desktop printers, that most people have at home, that use ink droplets to convert a digital file into paper. This ejection happens as the chamber filled with liquid reduces its volume through the application of an external voltage, which causes a shockwave responsible for the deposition of the ink. Inkjet 3D printing can be divided into two processes, according to the material being deposited: binder jetting and material jetting.

In binder jetting, as the name suggests, the material being jetted is a binder, which acts similarly to glue. As the parts manufactured are brittle and have high porosity, post-processing is necessary. This process can be applied to ceramic materials and metals, usually to produce sand casting cores and molds as the parts obtained have a good surface finish of around Ra 6 µm after post-processing, and there are almost no geometric restrictions.

In material jetting, the materials of the part, usually liquid photopolymers, are jetted through multiple nozzles to create a part. These process creates highly accurate parts, with most systems providing a dimensional accuracy of ± 0.1%, generally with a lower limit of ± 0.1 mm, with a good surface finish. In this process, multi-material parts that would normally take several processes and a final assembly, are manufactured in a single step [125]. As this process is also high cost it is usually employed to create visually appealing prototypes of almost any size with great dimensional accuracy.

Table A.1: Comparison of important characteristics of different 3D printing processes, with the data obtained from [126]

Process	Materials	Dimensional accuracy	Maximum build size	Support	Advantages	Disadvantages
Fused Deposition Modeling (FDM)	Thermoplastics (PLA, ABS, PETG, PC, PEI, etc.)	**Desktop**: ± 0.5% (lower limit ± 0.5 mm); **Industrial**: ± 0.15% (lower limit ± 0.2 mm)	**Desktop**: 200 x 200 x 200 mm; **Industrial**: 1000 x 1000 x 1000 mm	Not always required	Fast; Low cost; No post processing usually required	Rough surface finish; Anisotropic parts; Low accuracy
Vat photopolymerization	Photopolymer resins (thermosets)	**Desktop**: ± 0.5% (lower limit: ± 0.10 mm); **Industrial**: ± 0.15% (lower limit ± 0.01 mm)	**Desktop**: 145 x 145 x 175 mm; **Industrial**: 1500 x 750 x 500 mm	Always required	Good surface finish; Suitable for complex detailed parts	Brittle parts; Extensive post processing required
Binder Jetting	Metal and ceramic powders	**Metal**: ± 2%; **Full-color**: ± 0.3 mm; **Sand**: ± 0.3 mm	**Metal**: 800 x 500 x 400 mm; **Full-color**: 500 x 380 x 230 mm; **Sand**: 2200 x 1200 x 600 mm	Not required	Full-color options; No defects related to temperature changes	Low part strength; Extensive post processing necessary
Material Jetting	Acrylic photopolymers (thermoset)	± 0.1% (lower limit of ± 0.05 mm)	1000 x 800 x 500 mm	Always required	High accuracy; Good surface finish	Brittle part; High cost
Metal 3D printing (SLM and DMLS)	Metals and metal alloys	± 0.1 mm	500 x 280 x 360 mm	Always required	Suitable for complex parts; Excellent mechanical properties	High cost of metal powder and manufacturing process
Selective Laser Sintering (SLS)	Thermoplastics	± 0.3% (lower limit of ± 0.3 mm)	750 x 550 x 550 mm	Not required	Good mechanical properties; Suitable for complex parts	Only industrially available; Rough surface finish; Porous parts;

A.2 FDM Printing Parameters

Table A.2: FDM printing parameters and their influence on the manufactured part, for PLA filament

Property	Description	Influence on part
Infill style	Pattern of the material that fills the interior of the part	The infill pattern typically only has a notable influence on the failure strain of the part [85, 127]. However, it can be noted that the wiggle pattern increases both the ultimate tensile stress and the tensile modulus [128].
Wall thickness	Thickness of the exterior shell of the part	The thickness of the shell is proportional to the compressive and tensile strength of the specimen. In fact, it is one of the most influential parameters in part strength [112].
Layer thickness	Height of the layers, in the z-direction	The larger the layer thickness, the lower the build time but the strength of the part is compromised, as the adhesion between layers is minimized [129, 130]. However, in an upright orientation, tensile and flexible strengths increase as the layer thickness increases [131].
Bed temperature	Temperature of the build platform	The usual range of bed temperature is between 55 °C and 70 degree C. If the part is not adhering to the bed, the bed temperature should be increased. However, when the bed temperature increases the first layers might melt, causing the part to collapse on itself. Furthermore, it has been shown that tensile flexural strength increases as bed temperature increases [132].
Printing temperature	Temperature of the filament ejected	PLA filament is printed between 190 °C - 220 °C. The optimal temperature varies depending on the printer and the filament. In general, with the increase of temperature, the adhesion between layers increases but the part becomes more brittle [129].

A.3 3D Printing Parameters

Table A.3: Creality CR-10 3D printer properties, according to [99]

Forming technology	FDM
Print size	300 x 300 x 400 mm
Machine net weight	8.7 kg
Packing weight	13.5 kg
Nozzle diameter	0.4 mm
Software	Cura; Simplify3D; Repetier-host
File format	STL; OBJ; G-Code
Print speed	Standard: 60 mm/s Maximum: 100 mm/s
Filament diameter	1.75 mm
Support filament	PLA; ABS; TPU; wood; carbon fiber; copper
Power requirement	Input: 110 V - 220 V Output: 12 V Power: 270 W

Table A.4: 3D printing parameters used for both the PLA and the TPU filament

Layer	Nozzle Diameter	0.40 mm	
	Extrusion Multiplier	0.95 mm	
	Retraction Distance	**PLA**	**TPU**
		5.50 mm	Not Applicable
	Retraction Vertical Lift	**PLA**	**TPU**
		0.10 mm	Not Applicable
	Retraction Speed	**PLA**	**TPU**
		3000 mm/min	Not Applicable
	Primary Layer Height	0.20 mm	
	Top Solid Layers	3	
	Bottom Solid Layers	3	
	Outline/Perimeter Shells	2	
	First Layer Height	100 %	
	First Layer Width	110 %	
	First Layer Speed	**PLA**	**TPU**
		50 %	100 %
Temperature	Internal Fill Pattern	Rectilinear	
	Interior Fill Percentage	8 %	
	Outline Overlap	25%	
	Infill Extrusion Width	100%	
	Minimum Infill Length	5 mm	
	Internal Infill Angle Offsets	45 °; -45 °	
	Primary Extruder Temperature	**PLA**	**TPU**
		Layer 1: 190 ℃	Layer 1: 220℃
		Layer 2: 195℃	Layer 2: 225℃
		Layer 3: 200℃	Layer 3: 230℃
	Heated Bed Temperature	Layer 1: 45 ℃	
Cooling	Fan Speed	Layer 1: 0 % Layer 2: 50 % Layer 5: 100%	
Speeds	Default Printing Speed	**PLA**	**TPU**
		3600 mm/min	1200 mm/min
	Outline Underspeed	**PLA**	**TPU**
		50 %	100%
	Solid Infill Underspeed	**PLA**	**TPU**
		80 %	100%
	Support Structure Underspeed	**PLA**	**TPU**
		80 %	100%
	X/Y Axis Movement Speed	4800 mm/min	
	Z Axis Movement Speed	1002 mm/min	

A.4 Results Dimensional Accuracy Test

Table A.5: Results of the theoretical and measured diameter of the plates

Holes			**Cylinders**		
Theoretical Diameter (mm)	True Diameter (mm)	Observational Error (mm)	Theoretical Diameter (mm)	True Diameter (mm)	Observational Error (mm)
3	2,78	0,22	3	3,12	-0,12
4	3,77	0,23	4	3,94	0,06
5	4,86	0,14	5	4,91	0,09
6	5,85	0,15	6	5,9	0,1
7	6,69	0,31	7	6,97	0,03
8	7,77	0,23	8	7,96	0,04
9	8,78	0,22	9	8,95	0,05
10	9,78	0,22	10	9,97	0,03
11	10,8	0,2	11	10,98	0,02
12	11,84	0,16	12	11,94	0,06
13	12,81	0,19	13	12,95	0,05
14	13,76	0,24	14	13,96	0,04
15	14,79	0,21	15	14,99	0,01
16	15,72	0,28	16	15,92	0,08
17	16,74	0,26	17	16,83	0,17
18	17,69	0,31	18	17,85	0,15
19	18,73	0,27	19	18,88	0,12
20	19,71	0,29	20	19,86	0,14
21	20,66	0,34	21	20,95	0,05
22	21,72	0,28	22	21,87	0,13
23	22,67	0,33	23	22,86	0,14
24	23,64	0,36	24	23,82	0,18
25	24,71	0,29	25	24,81	0,19
26	25,7	0,3	26	25,85	0,15
27	26,67	0,33	27	26,82	0,18
28	27,65	0,35	28	27,87	0,13
29	28,64	0,36	29	28,93	0,07
30	29,58	0,42	30	29,89	0,11
31	30,61	0,39	31	30,86	0,14
32	31,6	0,4	32	31,91	0,09

A.5 First Prototype

Table A.6: Build statistics of the 3D printing of the first prototype

Part Name	Filament Material	Number of Parts	Filament Length	Material Cost	Printing Time
Strap	TPU	1	5121.6 mm	0.78 €	178 minutes
Elastic Support Element	PLA	3	329.0 mm	0.02 €	16 minutes
Shoulder Link	PLA	1	2026.7 mm	0.12 €	25 minutes
Forearm Link	PLA	1	4100.6 mm	0.25 €	61 minutes
Outer Telescopic Arm Link	PLA	2	5623.0 mm	0.34 €	64 minutes
Inner Telescopic Arm Link	PLA	2	1332.0 mm	0.08 €	18 minutes
Outer Telescopic Back Link	PLA	1	15821.2 mm	0.95 €	210 minutes
Inner Telescopic Back Link	PLA	1	11427.6 mm	0.69 €	138 minutes
Pin	PLA	3	2147.0 mm	0.13 €	32 minutes
Elbow Joint	PLA	1	19237.9 mm	1.16 €	251 minutes
Shoulder Joint	PLA	1	7268.3 mm	0.44 €	100 minutes
			Total	5.67 €	21 hours and 27 minutes

(a) Reach to opposite side of neck

(b) Reach to back of the head

(c) Hand to mouth

(d) Reach to opposite axilla

(e) Eat with a spoon

(f) Drink from a mug

(g) Answering the phone

(h) Brushing hair

(i) Raise a block to shoulder height

(j) Raise a block to head height

Figure A.1: First prototype of the exoskeleton performing various ADLs

Appendix B

Analytical Calculations

B.1 Denavit–Hartenberg Convention

The Denavit-Hartenberg (D-H) notation was proposed in 1955 by Jacques Denavit and Richard S. Hartenberg to describe and select frames of reference of serial-link mechanisms, used mostly in the field of robotics. In this convection, the mechanism is considered to contain two types of parts: rigid links and revolute or sliding joints. The origin of the coordinate frames is placed in the distal end of every link such that the z-axis is associated with the joint and the x-axis is associated with the link. The homogeneous transformation matrix A_j that allows the transformation from coordinate frame j to frame j-1 is a product of elementary rotations and translations, and function of the Denavit-Hartenberg parameters. The matrix A_j is represented in equation B.1.

$$A_j = R_{z,\theta_j} Trans_{z,d_j} Trans_{x,a_j} R_{x,\alpha_j} = \begin{bmatrix} cos\theta_j & -sin\theta_j cos\alpha_j & sin\theta_j sin\alpha_j & a_j cos\theta_j \\ sin\theta_j & cos\theta_j cos\alpha_j & -cos\theta_j sin\alpha_j & a_j sin\theta_j \\ 0 & sin\alpha_j & cos\alpha_j & d_j \\ 0 & 0 & 0 & 1 \end{bmatrix} \tag{B.1}$$

Firstly, it is necessary to construct the Denavit-Hartenberg parameter table to assemble the homogeneous transformation matrices represented in equation B.1 as $R_{z,\theta_j}, Trans_{z,d_j}, Trans_{x,a_j}$, and R_{x,α_j}. The D-H parameter table consists of four variables:

- **Joint Angle** (θ): Angle in degrees (°) from x_{j-1} to x_j around z_{j-1}
- **Link Twist** (α): Angle in degrees (°) from z_{j-1} to z_j around x_j
- **Link Length** (d): Distance in centimeters (cm) between the origin of frame j-1 and the origin of frame j along the z_{j-1} axis
- **Link Offset** (a): Distance in centimeters (cm) between the origin of frame j-1 and the origin of frame j along the x_j axis

As it is not possible to represent an arbitrary homogeneous transformation using four parameters, it is necessary to introduce the following constraints, considering frames j and j-1:

1. The axis x_j is perpendicular to the axis z_{j-1}
2. The axis x_j intersects the axis z_{j-1}

A schematic of the parameters and of the constraints 1 and 2 referred previously, in frames j-1 and j, is represented in figure B.1.

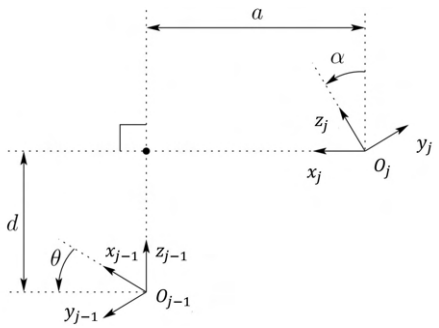

Figure B.1: Representation of the coordinate frames satisfying assumptions 1 and 2 and of the parameters necessary to construct the homogeneous transformation matrices, adapted from [133]

B.2 Arm Link Calculations

The critical part of the arm link is simplified to a cantilever beam with a width of $w = 0.02\,m$ and a height of $h = 0.02\,m$. The calculations of the stresses applied and the safety factor is presented in figure B.2. The critical section of the arm link is in the vicinity of the hole were the pin is introduced and, therefore, the stress concentration factor obtained through the chart in figure B.3 is taken into consideration. According to the calculations performed, the part satisfies the safety criteria.

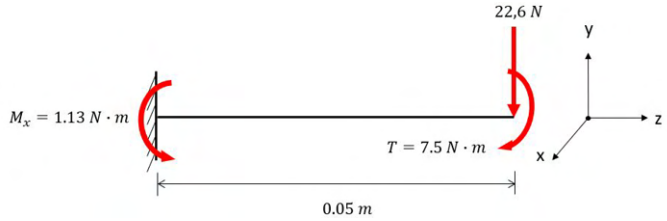

$I_x = 10.48 \times 10^{-9}\,m^4$, $Q_x = 9.17 \times 10^{-7}\,m^4$

$\sigma_{Mx} = 1.8 \frac{1.13 \times \frac{0.02}{2}}{10.48 \times 10^{-9}} = 1.94\,\text{MPa}$

$\tau_{Vy} = \frac{22.6 \times 9.17 \times 10^{-7}}{2 \times 0.0032 \times 10.48 \times 10^{-9}} = 0.31\,\text{MPa}$

$\tau_T = \frac{7.5}{2 \times 0.0032 \times (0.02 - 0.0032)(0.02 - 0.0032)} = 4.15\,\text{MPa}$

$\tau_{zy} = 4.15 + 0.31 = 4.46\,\text{MPa}$, $\sigma_z = \pm 1.94\,\text{MPa}$

$\sigma_A = 3.59\,\text{MPa}, \sigma_B = -5.53\,\text{MPa}$

$\frac{3.59}{29} - \frac{-5.53}{17.9} = \frac{1}{n} \longrightarrow$ **n = 2.31**

Figure B.2: Calculations of the stresses applied in the arm link

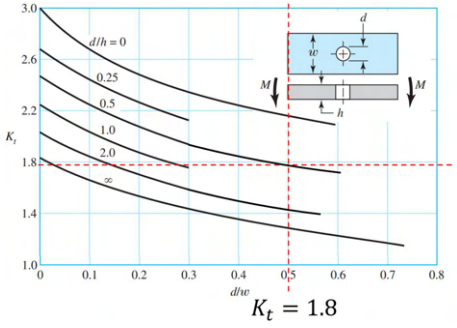

Figure B.3: Chart of the theoretical stress concentration factor for a rectangular bar with a transverse hole in bending [110]